1-3-2018

Power Management Systems for Biomass-Based Energy Harvesting

Ridvan Umaz

Power Management Systems for Biomass-Based Energy Harvesting

Ridvan Umaz, PhD

University of Connecticut, 2018

Energy harvesting aims to convert ambient available energy from the surrounding environment into usable electrical energy. There have existed many energy sources can be found to harness environmental energy, but the focus of this thesis is to harvest energy from aquatic environment to power up underwater devices. Microbial fuel cells (MFCs) are important energy-harvesting devices for underwater sensors and electronic devices. MFCs are a promising technology that converts bio-energy in the biomass substrate through electrochemical reactions into electricity. Due to the low voltage and power at MFC outputs, a power management system (e.g., power converter) is needed to boost the low voltage to a usable level by these devices. This thesis thus, presents power management circuits for biomass energy harvesting sources. New architectures and design techniques are discussed to achieve high system efficiency and effective design for MFCs.

The first part of this thesis focuses on the development of the maximum power extraction from energy sources by deploying an inductorless power converter (i.e. capacitive power converter). The maximum power extraction is not targeted for a specific energy sources, but rather is designed for both low-power energy source and high-power energy source without increasing complexity of system and the need of power hungry peripheral circuits. Proposed power converter is divided into two stages; a number of first-stage in parallel and shared-stage.

The first-stage maximizes power extraction from the energy source while the shared-stage operates as a conventional charge pump. The peak end-to-end efficiency is enhanced by 98\% as compared to the conventional converter. The proposed inductorles power converter has been implemented on a 0.13μm CMOS process.

The second part of the thesis discusses energy combiner architecture for multiple microbial energy harvesting sources. Combining four identical MFCs (i.e. the same material, size and structure) through their power converter is achieved by deploying digital circuit to allow them to connect in-order to either a load or a battery. Proposed design let's all sources contribute to the output and minimize the overall efficiency. The proposed efficient energy combiner architecture is implemented on a 0.13μm CMOS process.

The remainder of the thesis deals with power management circuits that have ability to recover bioturbation issue in MFCs. A unique issue in marine sediment MFCs is related to underwater bio-stress, referred to as bioturbation is discussed. Solution to bioturbation issue brings new requirements on the design of power management systems (PMSs). The third part of the thesis presents an off-the-shelf power management system for multi anode MFCs. The PMS has been tested through a prototype BFMC. Experimental results demonstrate the effectiveness of this design for multi anode MFCs.

The last part of the thesis discusses an integrated circuit for multi anode MFC to detect automatically impaired anodes. The evaluation is made in using a 90nm CMOS technology. The proposed design provides 42% more efficiency than conventional design under the worst-case scenario.

Power Management Systems for Biomased-Based Energy Harvesting

Ridvan Umaz

B.S., Inonu University, 2009

M.S., University of Connecticut, 2013

A Dissertation

Submitted in Partial Fulfillment of the

Requirements for the Degree of

Doctor of Philosophy

at the

University of Connecticut

2018

APPROVAL PAGE

Doctor of Philosophy Dissertation

Power Management System for Biomass-Based Energy Harvesting

Presented by

Ridvan Umaz, B.S., M.S.

Major Advisor _____

Lei Wang

Associate Advisor _____

John Chandy

Associate Advisor _____

Faquir Jain

University of Connecticut

2018

To my family, my parents and my wife

Abstract

Energy harvesting aims to convert ambient available energy from the surrounding environment into usable electrical energy. There have existed many energy sources can be found to harness environmental energy, but the focus of this thesis is to harvest energy from aquatic environment to power up underwater devices. Microbial fuel cells (MFCs) are important energy-harvesting devices for underwater sensors and electronic devices. MFCs are a promising technology that converts bio-energy in the biomass substrate through electrochemical reactions into electricity. Due to the low voltage and power at MFC outputs, a power management system (e.g., power converter) is needed to boost the low voltage to a usable level by these devices. This thesis thus, presents power management circuits for biomass energy harvesting sources. New architectures and design techniques are discussed to achieve high system efficiency and effective design for MFCs.

The first part of this thesis focuses on the development of the maximum power extraction from energy sources by deploying an inductorless power converter (i.e. capacitive power converter). The maximum power extraction is not targeted for a specific energy sources, but rather is designed for both low-power energy source and high-power energy source without increasing complexity of system and the need of power hungry peripheral circuits. Proposed power converter is divided into two stages; a number of first-stage in parallel and shared-stage. The first-stage maximizes power extraction from the energy source while the shared-stage operates as a conventional charge pump. The peak end-to-end efficiency is enhanced by 98% as compared to the conventional converter. The proposed inductorles power converter has been implemented on a 0.13 μm CMOS process.

The second part of the thesis discusses an energy combiner architecture for multiple microbial energy harvesting sources. Combining four identical MFCs (i.e. the same material, size and structure) through their power converter is achieved by deploying digital circuit to allow them to connect in-order to either a load or a battery. Proposed design lets all sources

contribute to the output and minimize the overall efficiency. The proposed efficient energy combiner architecture is implemented on a 0.13 μm CMOS process.

The remainder of the thesis deals with power management circuits that have ability to recover bioturbation issue in MFCs. A unique issue in marine sediment MFCs is related to underwater bio-stress, referred to as bioturbation is discussed. Solution to bioturbation issue brings new requirements on the design of power management systems (PMSs). The third part of the thesis presents an off-the-shelf power management system for multi anode MFCs. The PMS has been tested through a prototype BFMC. Experimental results demonstrate the effectiveness of this design for multi anode MFCs.

The last part of the thesis discusses an integrated circuit for multi anode MFC to detect automatically impaired anodes. The evaluation is made in using 90nm CMOS technology. The proposed design provides 42% more efficiency than conventional design under the worst case scenario.

Contents

List of Tables

List of Figures

Chapter 1

Introduction

1.1 Energy Harvesting

In the last two decades, the focus on batteryless applications has been grown in areas of wireless sensor nodes (WSN) and Internet of Things (IoT). The surrounding envrionment can be actively exploited to derive energy to provide usable power (i.e. the batteryless power supply) to a wide set of applications. The batteryless power supply is so-called energy harvesting. Energy harvesting is an active process that converts ambient available energy into electrical energy. Multiple types of energy sources including microbial fuel cells [2], piezoelectronics [4], photovoltaic cells [5], RF [6], thermal energy [7] and others are available to harnes environmental energy to utilize at various loads.

However, there are three main challenges in energy harvesting (i.e. specially low ambient power level) to power up the loads. First, the available energy harvested from the environment is extremely constrained by either ambient conditions or some design parameters. Energy sources typically generate low voltage and power at their outputs. For example, for photovoltaic cells, light intensity varies widely depending on locations and illuminance can range from 10s of lux at twilight or dim indoor conditions to 100Ks lux under direct sunlight. They can produce power from 5μW to 10mW [8]. Another example, microbial fuel

cells (MFCs) exploit bioelectrochemical reactions to generate power in the range of 10μW to 2mW, which highly depends on electrode size, installation distance [9],[10], [1] and thermodynamic limitations [11]. In order to improve the output voltage and power of MFCs, some existing techniques rely upon shortening the distance of electrodes [12], applying different cathode arrangements [13], and using multiple independent MFCs [14]. Most of these works rely upon large or parallel electrodes for higher power output. This is because connecting multiple BMFCs in series in open water does not help; i.e., this arrangement is equivalent to a single BMFC setup [15], [16].

Second, since energy harvesting starts with low ambient voltage and power levels, the generated voltages from energy sources are usually low, ranging from 10s of milivolts to 100s of milivolts. However, these voltages are not sufficient for electronic devices (e.g. sensors) to operate. In addition, energy sources are not suitable to directly power electronic devices, because the voltages at the outputs of energy sources can vary considerably during operation. Therefore, designing a low input voltage (e.g. less than 1V) power converter is crucial to up-convert the low voltage to a level usable by the load.

Finally, the harvesters need to be constructed efficiently to approach maximum power extraction. The maximum power available from the energy sources can be obtained by adjusting system parameters (e.g., number of stages, switching frequency). However, adjusting these system parameters need to either get help of DSP or CPU, or implement some power-consuming control logic circuits. One example, two different microbial fuel cells used as energy sources [17] generate the maximum power of 1.6mW and 11.2μW, and a maximum power extraction circuit is implemented to achieve this. However, the peak power dissipation of the circuit is 36.4μW which is much higher than the low MFC power out. Therefore, this maximum power extraction circuit is not well-suited for all energy sources. For low energy sources, maximum power extraction circuits should be ultra low-power. Also, these circuits should be designed for a variety of power ranges in energy sources.

1.2 Biomass-Based Energy Harvesting

A growing interest in aquatic exploration such as marine ecosystem observation, pollution detection, temperature monitoring, ocean disaster deterrence and surveillance for undersea infrastructure has been shown recently [9, 18]. The most appropriate technology for these applications is to employ underwater remote sensor networks [19, 20]. At the present time, the most omnipresent method to power up these sensors is to deploy batteries. However, the long-term use of these sensors is generally constrained by the finite charge stored in batteries which are used as the primary power source in remote sensor networks. In order to keep the operations of these sensors, batteries needs to be replaced if needs. The cost of the replacement is appeared as an expensive and a dangerous processes due to having a diving team to handle it in a hard reached locations under aquatic environment. In addition, if considered environmental impact, the toxicity of some types of batteries is harmful to living orgainsms in aquatic environment.

Energy supply for these applications should be located around the sensors and should be sustainable. Therefore, a promising alternative renewable energy source should be employed. The ability to harvest energy from an aquatic envrionment is microbial fuel cells (MFCs). MFCs are a promising techology that converts bio-energy in the biomass substrate through electrochemical reaction into electricity to power up underwater devices.

1.2.1 History and Background

In 1911, M. Potter was the first to suggest the idea of deriving electrical energy from bacteria [21]. This would lead to deploying groups of bacteria into cells as to harness better power generation capacity. This accrelerated the breakthrough of Microbial Fuel Cells (MFCs). In 1931, Barnet Cohen continued the study of microbial fuel cell by connecting some semi MFCs in series and generated the output voltage of 35V with a current of 2mA [22]. However, there

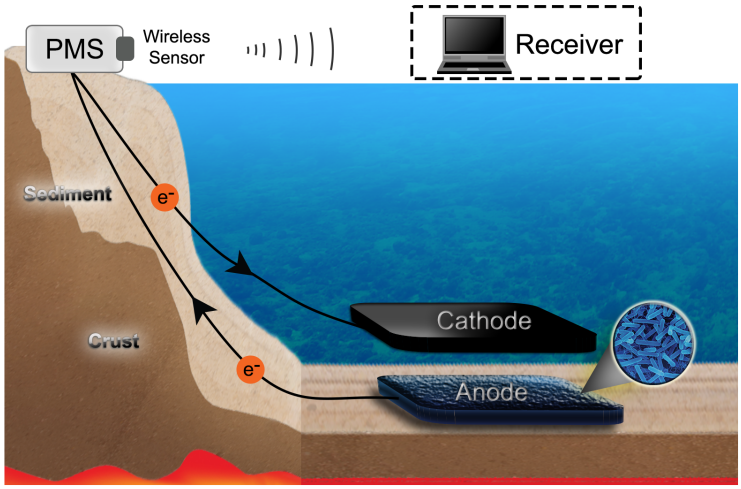

Figure 1.1: The application scenario of microbial fuel cells in the underwater environment.

were no any indications of studies of the MFCs from 1931 to 1960s. Del Duca et al. used hydrogen which was yielded from glucose fermentation using Clostridium butyricum as the reactive material in fuel cell anode [23], but this attempt was not reliable enough. In 1970s, to solve this unreliable issue the concept of the using microorganism as catalysts in fuel cells was proposed by Suzuki et al. [24]. Energy harvesting with microbial fuel cells, which implement in deep oceans, lakes and other aquatic environments, is becoming a promising technologh due to the impractical use of other energy harvesters such as solar cell, vibration and wind in the aquatic environment [25], [3], [15]. A basic implementation of MFCs in aquatic environment is shown in Fig. 1.1.

1.2.2 Energy Source

Basically, microbial fuel cells convert chemical energy into electrical energy by generating electricity directly from biodegradable substrates. In other words, MFCs take advantage of the metabolism of aquatic microorganisms [26] to drive electrochemical reactions and generate electrical energy from organic matters. The basic structure of MFCs is shown in Fig 1.2. In order to generate electricity from MFCs, an anode must be buried under sediment

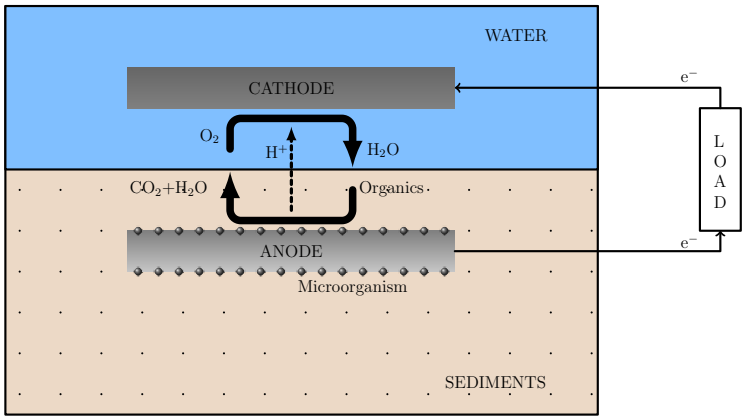

Figure 1.2: The basic principle of MFCs.

while a cathode floats in the water. Microorganisms growing on the anode surface degrade organic matter and release electrons [27]. These freed electrons pass through an external load (e.g. sensors and resistors) to reach the cathode where it is exposed to dissolved oxygen, and then these electrons combine with protons and oxygen to yield water; thus, a full circuit is completed and electricity is generated.

Each energy source has different electrical models to represent their internal equivalent circuits. MFCs can be modeled as a voltage source in series with a resistor. A simplified electrical equivalent model for MFCs with connected components (e.g. boost converters, resistive loads, charge pumps) is constructed in Fig. 1.3.

Maximum power extraction from MFCs as the energy source is obtained once the input impedance (R_{eq}) of the connected components interfacing with the source is viewed to be equal to the source internal impedance (i.e. R_{MFC}=R_{eq}). This is referred as the impedance matching theory. The maximum power can be represented as

$$P_{max} = \frac{V_{MFC}^2}{4R_{MFC}}. \tag{1.1}$$

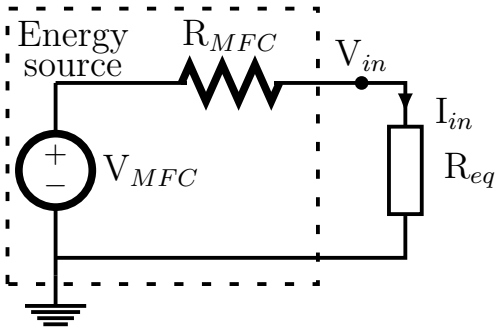

Figure 1.3: An electrical equivalent circuit for MFCs with the connected component.

Table 1.1: Summary of power converters.

	Circuit	Pros	Cons
Power Converters	Charge pump	Low Vin Integrated Self-start-up abilitiy	Low Vout Low efficiency
	Boost converter	High Vout High efficiency	High Vin Off-chip inductor

1.3 Energy Harvesting Interfaces

One limiting issue in MFCs energy harvesting is to provide low output voltage and power at their outputs [11, 15, 16, 28–34]. Many studies have focused on improving output voltage and power of MFCs and some techniques depend upon development of new materials, improvement of the design [10], deploying large electrodes [16], connecting multiple MFCs in parallel and in series [35], shortening the distance of electrodes [12], applying different cathode arrangements [13], and using multiple independent MFCs [14]. In spite of these efforts, the output voltages of MFCs (the theoretical value is about 1.1V [25, 27]) are not at a usable level because the typical operating voltage for the sensors are far from these voltages. To tackle this problem, an interface circuit (i.e. power converter) is required between MFCs and a load to meet a specific load demanding voltage (e.g. 1.8V) [11, 15, 16, 26, 28, 30, 33, 34].

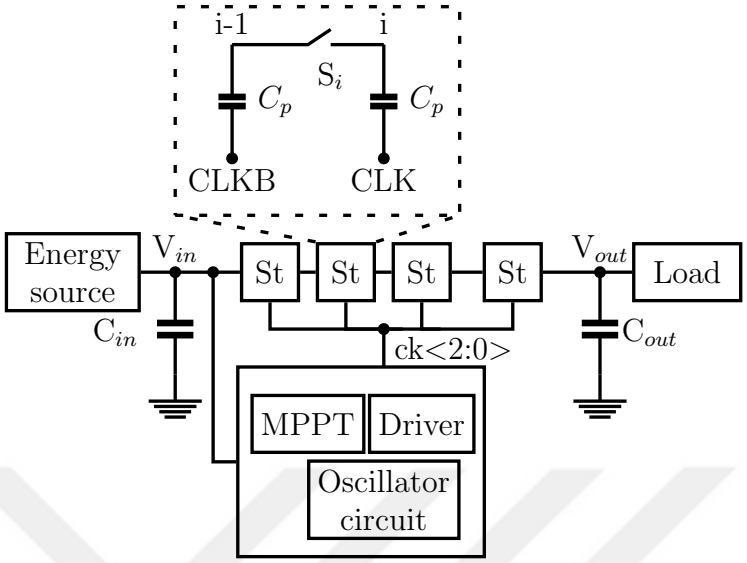

Figure 1.4: A top level block diagram of capacitive converter.

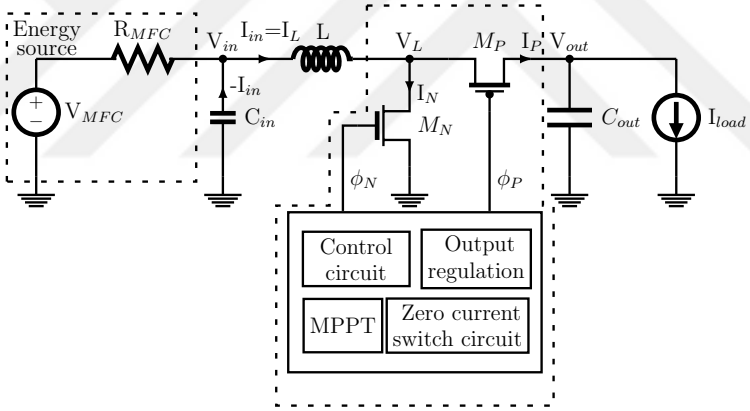

Figure 1.5: A top level block diagram of inductive converter.

Mainly two types of power converters are available; charge pump (capacitive) (shown in Fig. 1.4) and boost converter (inductive) (shown in Fig. 1.5). In energy harvesting systems, capacitive power converters can be principally used as either a step-up power converter [17] or an auxiliary circuit (e.g. start-up) [36, 37]. Compared to an inductive boost converter, which is most of the time an essential part in energy harvesting system, capacitive one comes fully integrated on a chip with better self-start-up ability, and operates at a low voltage level and is thus more applicable for low-power energy harvesting systems. However, the capacitive

one is well-known to achieve low conversion efficiency and output voltage. Moreover, it does not provide a sufficient voltage level to some load applications (e.g. 3.3V) and even if it does, it provides low power efficiency (i.e. less than 5%) which does not power up the load.

The efficiencies comparison is expressed as

$$\eta_{cp} < \eta_{dc} \tag{1.2}$$

where, η_{cp} is the efficiency of charge pumps and η_{dc} is the efficiency of boost converters.

Comparison of power converters for some parameters are summarized in Table 1.1.

Due to the inherent low output power of MFCs, a temporary energy storage element (e.g. super capacitor or rechargeable battery) in the interface circuit is needed to accumulate the harvested energy so as to intermittently transfer to the load. The load, therefore, will be operated in the burst mode.

1.4 Thesis Contribution and Organization

The possibility of self-powered operation for underwater devices is achieved by using microorganism to harvest energy in aquatic environment like lakes, rivers and oceans to provide usable electrical power. This thesis explorers four power management systems for marine MFC systems with a particular emphasis on circuital solutions addressed to the extraction of the maximum power, the combining of the multiple energy sources and the bioturbation issue.

Chapter 2 presents an inductorless power converter (i.e. charge pump) with maximizing power extraction for energy harvesting systems. The state-of-the-art of charge pumps in energy harvesting require complex and power hungry peripheral circuits to extract the maximum power from energy sources. However, for low-power energy sources, extracting the maximum power is of concern to implement high budget power need for circuits. A

new technique is then presented that allows either low-power energy source and high-power energy source to extract the maximum power out. The inductorless power converter divided two parts demonstrated with the circuit implemented on a 0.13-μm CMOS process enhances the extracted power from energy source by range of 117%-161%. As compared to the conventional converter, this study improves the peak end-to-end efficiency by 98%. This work demonstrates how it is possible to extract the maximu power out of energy sources without increasing complexity and the need of large power.

Chapter 3 focuses on an energy harvesting system that combines energy from multiple and homogeneous microbial fuel cells to expand overall system reliability and increase system efficiency. Conventional energy combiner circuits either exclude some sources to contribute or need of a precharge voltage to start up are discussed and identified the problems with them. A new energy combiner circuit is proposed and impemented on a 0.13-μm CMOS process. The combiner is based on output time-multiplexing scheme that connects outputs of converters in-order and equal time. Digital control circuit that configures the connection orders and the routing ways (i.e. either the load or the battery.) is presented. The stored energy at the converter outputs is fully transferred without loss of energy by routing the outputs to the load or an energy storage (e.g., a rechargeable battery or a super capacitor). This architecture allows all energy sources to simultaneously operate and include all sources to increase overall system reliability. In this work, it is demonstrated that how proposed energy combiner circuit can be effective with multiple and homogenous MFCs.

Chapter 4 and chapter 5 discuss power management systems featuring the decoupling of the impaired anodes from the rest of the system to enhance overall system reliability. Chapter 4 presents an off-the-shelf power management system for achieving bioturbation resilince in multi anode MFCs. The PMS includes a multi anode decoupling circuit, a switching circuit and a boost converter. The PMS is self-starting and can automatically detect the impaired anodes due to bioturbation. Design optimization of the PMS includes the consideration of both the power transfer efficiency and the impact of possible bioturbation problems. The

detailed design of the PMS is discussed and performance is tested with a prototype multi-anode BMFC. This work achieves higher efficiency with consideration of bioturbation as compared to previously published works.

Chapter 5 introduces a fully integrated power management circuit for multi anode MFCs.The integrated PMS consists of a shared-stage charge pump, an energy accumulation and transfer control circuit and a boost converter. The circuit is implemented on a 90nm CMOS process. The impaired anode decoupling is achieved in the Frontier stage of the shared-stage charge pump. The PMS starts an input voltage as low as 0.35V and regulates the output to 3.3V. Proposed PMS achieves a maximum efficiency of 62%. As compared to conventional design, Integrated power converter provides 42% improvement in overall efficiency. Chapter 6 draws conclusions for all works done as part of this thesis.

Chapter 2

Design of An Inductorless Power Converter with Maximizing Power Extraction for Energy Harvesting

2.1 Introduction

Energy harvesting utilizes the surrounding environmental energies to provide power to a wide set of applications, such as wireless sensor networks and remote devices [3], [10]. Energy sources including microbial fuel cells [2], piezoelectronics [4], photovoltaic cells [5], RF [6] and thermal energy [7] are serviceable for harvesters to utilize at various loads.

However, there are three main challenges in energy harvesting (i.e. specially low ambient power level) to power up the loads. First, the available energy harvested from the environment is extremely constrained by either ambient conditions or some design parameters. Energy sources typically generate low voltage and power at their outputs. For example, for photovoltaic cells, light intensity varies widely depending on locations and illuminance can range from 10s of lux at twilight or dim indoor conditions to 100Ks lux under direct sunlight. They can produce power from 5μW to 10mW [8]. Another example, microbial fuel

cells exploit bioelectrochemical reactions to generate power in the range of10μW to 2mW, which highly depends on electrode size, installation distance [9],[10], [1] and thermodynamic limitations [11].

Second, since energy harvesting starts with low ambient voltage and power levels, the generated voltages from energy sources are usually low, ranging from 10s of milivolts to 100s of milivolts. However, these voltages are not sufficient for electronic devices (e.g. sensors) to operate. In addition, energy sources are not suitable to directly power electronic devices, because the voltages at the outputs of energy sources can vary considerably during operation. Therefore, designing a low input voltage (e.g. less than 1V) power converter is crucial to up-convert the low voltage to a level usable by the load. There are two types of up-converters: an inductive type and a capacitive (i.e. inductorless) type. The inductive type converters are not fully-integrated due to external bulky components, and thus they are not preferable in many applications with size constraints. The capacitive converters can be an alternative solution. Some previous works have studied the inductorless power converter [17], [38], [39], [40], [41] but they use general-purpose charge pumps implemented by either varying the number of stages on different load conditions or modulating switching frequency. These works usually require complex and power-hungry peripheral control circuits, thereby compromsing low-power operation.

Finally, the harvesters need to be constructed efficiently to approach maximum power extraction. The maximum power available from the energy sources can be obtained by adjusting system parameters (e.g., number of stages, switching frequency). However, adjusting these system parameters need to either get help of DSP or CPU, or implement some power-consuming control logic circuits. One example, two different microbial fuel cells used as energy sources [17] generate the maximum power of 1.6mW and 11.2μW, and a maximum power extraction circuit is implemented to achieve this. However, the peak power dissipation of the circuit is 36.4μW which is much higher than the low MFC power out. Therefore, this maximum power extraction circuit is not well-suited for all energy sources. For low energy

sources, maximum power extraction circuits should be ultra low-power. Also, these circuits should be designed for a variety of power ranges in energy sources.

To overcome the above-mentioned challenges, this part of thesis develops an efficient inductorless power converter for renewable energy sources to maximize the power extraction without introducing additional power overhead and circuit complexity. The proposed power converter employs a hybrid charge pump circuit that is divided into two stages. The first stage utilizes a number of pump units connected in parallel to maximize the power extraction from energy sources. The second stage is a shared-stage that acts as a conventional charge pump to step up the output voltage at the required level by the load. The proposed converter is achieved simply maximum power out from low-power energy sources owing to multiple first-stage instead of need of external sources i.e. battery and complex circuits. In comparison with conventional converter i.e. one first-stage, the proposed converter with three first-stage demonstrates some distinct advantages: (1) the maximize power extraction from energy sources is improved by range from 117% to 161% over the conventional one; (2) 183% more output current at the converter is obtained.

The rest of this chapter is organized as follows. Section 2.2 describes the system architecture including the conventional power converter and the proposed one. Section 2.3 discusses how to achieve maximum power extraction. In section 2.4, the design method and optimization of the proposed power converter are developed. Section 2.5 presents the detailed design of the proposed inductorless power converter circuit. Section 2.6 evaluates the simulation results, and conclusions are drawn in Section 2.7.

2.2 System architecture

2.2.1 Existing architectures

Conventional energy harvesting circuits consist of an inductorless DC-DC converter which is based on capacitor switching including a charge pump and its driver circuit [17], [38], [39], as shown in Fig. 5.5. The power converter is composed of a number of sequential charge stages connected in series. Two complementary non-overlapped signals (CLK and CLKB) are generated by the driver circuit to drive the charge pump, charge the capacitor and switch on/off transistors in order to transfer the stored charges in the present stage to the following stage at the pump. Efforts to maximize power extraction from energy sources (e.g., microbial fuel cells, photovoltaic and thermoelectric harvesters) with capacitive-based converters depend upon matching the internal impedance of the energy source with the converter, i.e., so-called impedance matching method.

The output impedance of a capacitive based converter is given by [42]

$$R_{eq} = \frac{N}{f \times C} \tag{2.1}$$

where N is the number of stages, f is the switching frequency, and C is the pumping capacitor. It is obviously that the impedance can be adjusted by setting either the number of stages [38] or the switching frequency [17],[43],[44]. However, adjusting these parameters requires complex circuit implementations with power-hungry control logic. In addition, low-power output from the energy source does not provide sufficient power to adjust its impedance without using some external power supplies, and this affects the normal converter operation. Another technique is to apply forward/reverse body biasing to extract maximum power out from energy sources [45], [46]. However, they require well-designed clock signals and power-hungry peripheral circuits to drive charge pumps. There should be a more convenient way

to maximize the power extraction from energy sources instead of using more complex circuit implementations.

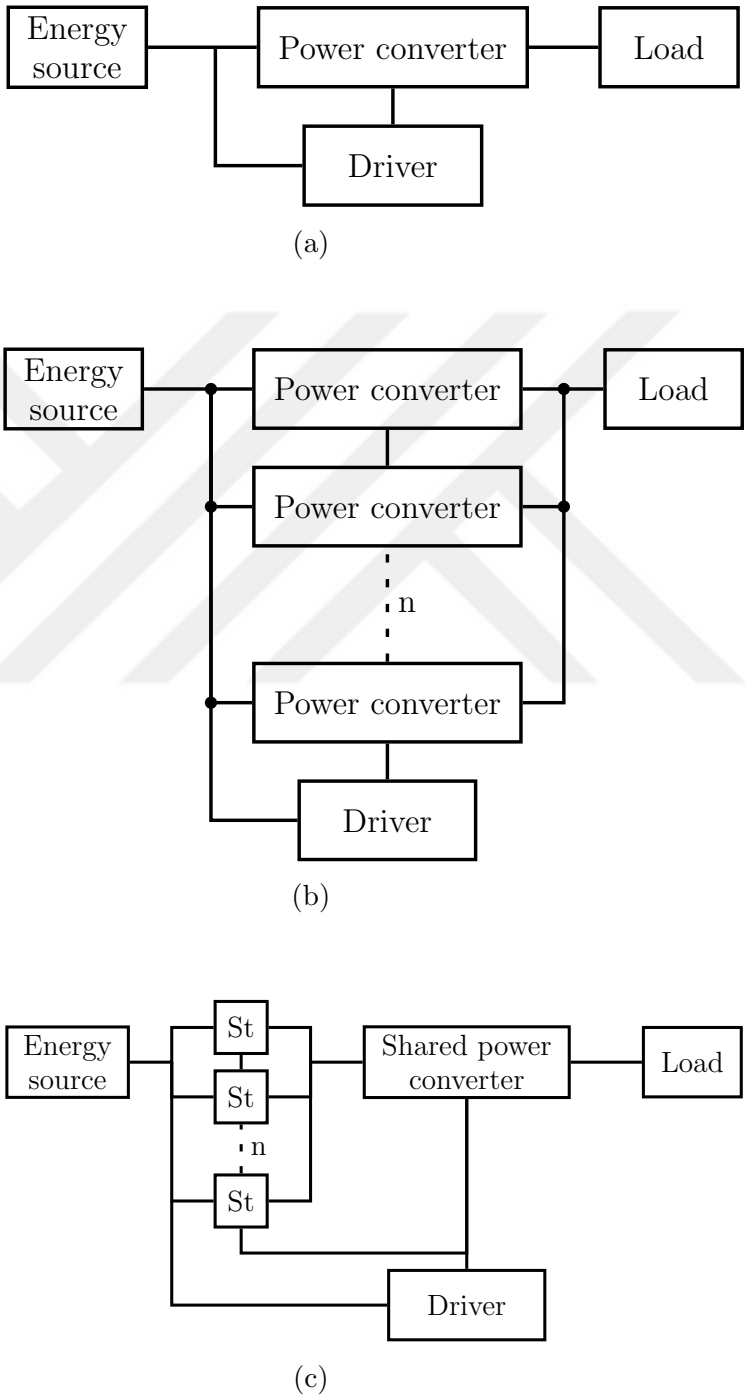

Figure 2.1: (a) Conventional architecture with an inductorless power converter. (b) Proposed inductorless power converter. (c) Optimized proposed inductorless power converter.

2.2.2 Proposed energy harvesting circuit

A more effective energy harvesting circuit over conventional one is given here, as shown in Fig. 2.1b. Although the same converter in conventional design is deployed, a number of power converters connected in parallel are used. Instead of employing a number of driver circuits, one common driver circuit is assigned to drive the converters. Due to connected a number of converters in parallel, proposed converter output impedance is clearly smaller than conventional one (see eq. 2.3).

Although proposed power converter is simply well-suited for adjusting the converter impedance to enlarge power extraction from energy source, it has large area overhead and power losses. To overcome these problems associated with proposed power converter, a more compact and efficient power converter is proposed in this work, as shown in Fig. 2.1c. The optimized proposed power converter consists of a core power converter and a driver circuit. The core is divided into two stages. The first stage includes a number of pumping stages connected in parallel. These pumping stages have the same stage circuit (St) whose output are combined at the same node. The merged node at the outputs of the pumping stages provide the input voltage for following stage (i.e., shared-stage).

The second stage is the shared-stage, which includes a number of sequential pumping stages connected in series that operate like a conventional charge pump. The driver circuit gets its supply voltage from the energy source. Although the driver circuit is similar to the conventional converter one, it has the capability to drive both the first-stage and the shared-stage, instead of employing separately drivers for each.

The output voltage of the proposed charge pump with N stages is expressed as

$$V_{out} = V_c + (N-1) \times \Delta V = V_c + \sum_{i=1}^{N-1} (V_L - \frac{I_{out,i}}{C_i \times f}) \tag{2.2}$$

where ΔV is the voltage fluctuation at each pumping node., V_L is the clock supply voltage

(input voltage of the energy source), V_c is the output voltage of the first-stage, C_i is the pumping capacitance at the i^{th} stage, f is the clock frequency and I_{out} is the output current.

Note that the impedance matching method is applied to the proposed power converter as well. However, the impedance of the conventional converter expressed in (2.1) is not applicable to the proposed converter. New variables should be incorporated into 2.1 and the proposed power converter output impedance is given by

$$R_{eq_{pro}} = (\frac{N}{f \times C}) \times \frac{1}{k} \tag{2.3}$$

where k is a factor that is associated with the number of the pumping stages at the first-stage connected in parallel. The factor k should be less than the number of the pumping stages at the first-stage ($k < n$). This is mainly due to the fact that the number of switching transistors and the pumping capacitors at the shared-stage is smaller than n conventional power converters connected in parallel including n driver circuits.

As the number of pumping stages at the first-stage increases, the current drawn from the energy source also increases while the voltage at the output of the energy source decreases. Thus, the power extracted from the source will approach the maximum power point. Thus, the proposed converter improves the power extraction from the energy source as compare to the single first-stage implementation (i.e., conventional one), thereby transferring more extracted power to the shared-stage.

2.3 Maximum power extraction

Each energy source has different electrical models to represent their internal equivalent circuits. While solar cells can be modeled as a current source in parallel with a diode, MFCs and TEGs can be modeled as a voltage source in series with a resistor. However, all energy sources can be generally modeled as a Thevenin voltage in series with a Thevenin equiva-

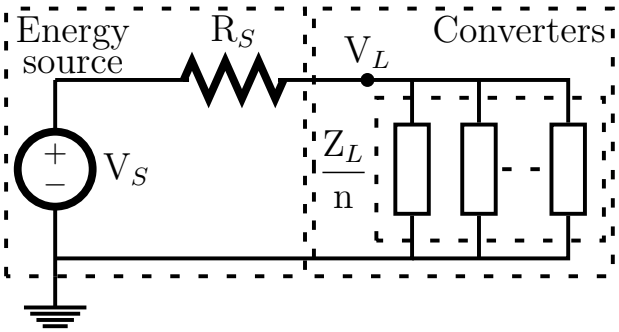

Figure 2.2: Thevenin electrical equivalent circuit for energy sources (e.g. solar, MFCs, TEGs).

lent impedance, which could include resistance, capacitance and inductance. The Thevenin equivalent circuit for energy sources (e.g. solar, MFCs and TEGs) with n power converters connected in parallel and sharing a common driver circuits is shown in Fig. 2.2. Note that the proposed converter including N pumping stages connected in parallel at the first-stage acts as n power power converter connected in parallel. Maximum power extraction from an energy source is obtained once the input impedance of the connected components (e.g. boost converters, resistive loads, charge pumps) interfacing with the source is viewed to be equal to the source internal impedance (R_S=R_{eq}). This is referred to the impedance matching theory.

The maximum power can be obtained as

$$P_{max} = \frac{V_S^2}{4R_S}. \tag{2.4}$$

In Fig. 2.2, the power delivered to the n power converters connected in parallel can be described as

$$P_L = (\frac{V_S}{R_S + \frac{Z_L}{n}})^2 \times \frac{Z_L}{n} \tag{2.5}$$

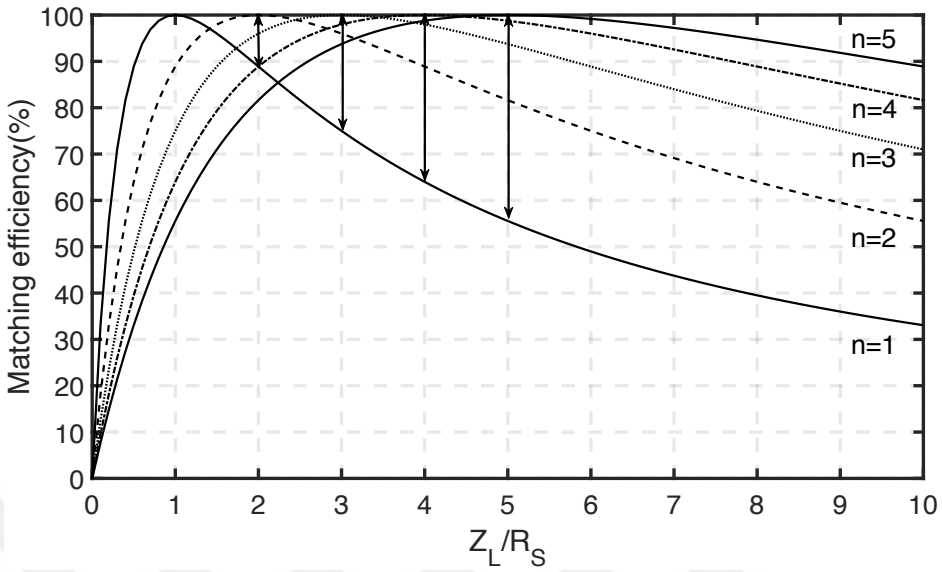

Figure 2.3: Matching efficiency η_Z as a function of $\mathrm{Z}_L/\mathrm{R}_S$.

The matching efficiency η_Z can be viewed as the ratio of P_L to P_{max}, given by

$$\eta_Z = \frac{P_L}{P_{max}} = \frac{4}{\frac{Z_L}{n\times\ R_S} + \frac{n\times\ R_S}{Z_L} + 2} \tag{2.6}$$

Fig. 2.3 shows the matching efficiency as a function of Z_L/R_S under various values of n. More than 90% of the available power can be extracted from the energy sources once the endurable impedance mismatch ranges from -48% to +93% for the conventional converter. The impedance mismatch range increases proportionally with the number of the converters connected in parallel. For instance, once two converters are connected in parallel, the impedance mismatch ranges from -2×48 (-96%) to +2×93 (+186%) for more than 90% of the matching efficiency. This shows the number n of converters have a significant error tolerance over the conventional design. Therefore, the output power remains very close to the maximum power point (MPP) even when a large impedance mismatch occurs in the proposed converter design. This is a simple and self-starting (i.e., no need for extra power supplies) method to maximize the power extraction, instead of employing more complex power-hungry peripheral circuits as in conventional converter designs.

2.4 Design optimization

Maximizing power extraction from energy sources and achieving a high power conversion efficiency at the end of power converters are crucial, in particular when low power sources are used as the energy source. To maximize power out and acquire high efficiency, some design parameters (e.g. current consumption, capacitor values, transistor sizes, etc.) need to be optimized and selected appropriately. Some previous works [47], [48] discussed a general strategy for charge pump design optimization. However, this method is insufficient to the proposed converter. A new design and optimization method is required in order to achieve the best efficiency.

In Section 2.2.2, the output voltage is given as a function of the first-stage output voltage V_c as (2.2). For simplicity, the first-stage pump capacitance is not considered. However, design optimization throughout the proposed converter should include the first-stage pump parameters with shared-stage ones.

The output voltage of the proposed converter with N stages can be expressed as

$$V_{out} = (N+1) \times V_L - \left[\frac{I_{out}}{f \times C_f \times n} + \frac{I_{out}}{f \times C_s} \times (N-1) \right] \tag{2.7}$$

where I_{out} is output current, f is the switching frequency, n is the number of the pumping stages at the first-stage, C_f and C_s are pump capacitances of the first-stage and shared-stage, respectively.

Note that there are two terms in (2.7). The first one refers to the pump output voltage ((N+1)×V_L) in the case of a pure capacitive load, and the second one presents voltage loss in the case of a current load. The second term also has two components: the first one reflects the effect of the first stage on the output of the power converter, and the second one shows the effect of the shared stage which is voltage drop on the charge pump output once the load is connected.

The number of the pumping stages at the shared-stage is determined by (2.2) and can be given by

$$M = \frac{V_{out}}{V_c} - 1 \tag{2.8}$$

The first-stage pumps are counted as one pumping stage without considering the number of pumping stages in parallel, due to the same voltage V_c at the output of the first stage. The total number of pumping stages at the proposed converter is thus given by

$$N = 1 + M \tag{2.9}$$

The number of the pumping stage at the first stage depends on the particular energy source being used.

In order to fully transfer the stored charge from a capacitor (e.g. C_f) at the first stage to a capacitor (e.g. C_s) at the shared stage, the capacitance of the first stage should be much smaller than the shared-stage one. Otherwise, the remaining charges at the first stage will reduce the pumping capability. This can be set as

$$C_f \times n \leq C_s \tag{2.10}$$

where n is the number of the pumping stages at the first stage.

Substituting (2.10) into (2.7), we can derive the capacitance of a stage in (2.7) as

$$C_f = \frac{I_{out}(N-1)}{f \times n[(N+1) \times V_{DD} - V_{out}]} \tag{2.11}$$

The transistors also need to be sized accordingly in order to support the efficient charge transfer from the first stage to the shared stage.

The input and output capacitors should also be considered. The input capacitor C_{in} is critical since energy sources are low power. The capacitor accumulates the harvested

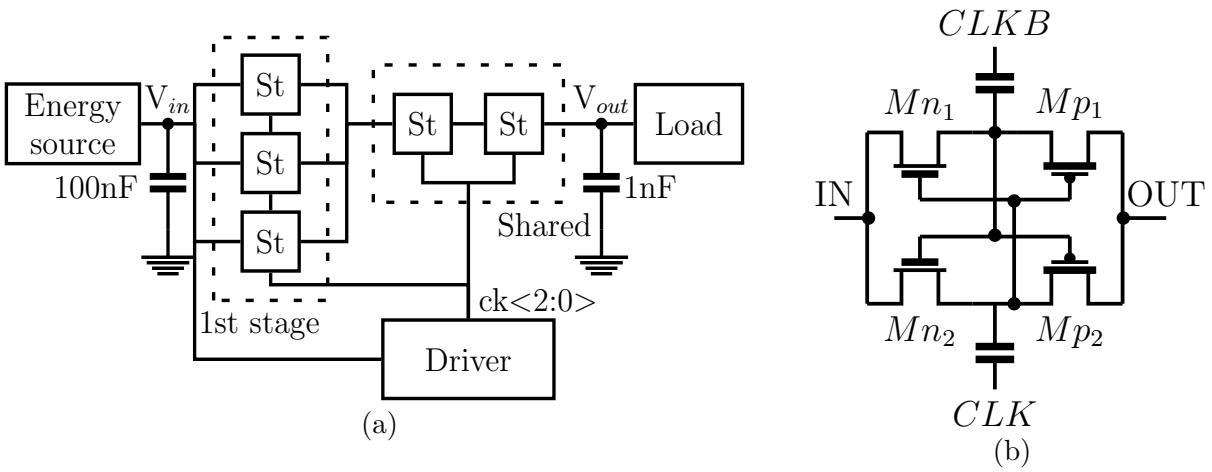

Figure 2.4: (a) Block diagram of the proposed power converter. (b) Circuit implementation of the charge pump stage (St).

energy so as to provide supply voltage for the driver circuit as well the input voltage for the converter.

2.5 Circuit implementation

The block diagram of the proposed power converter is shown in Fig. 2.4a. The converter consists of three first-stage and two shared-stage pumps, and two non-overlappled clock signals. Due to the inherent low power at the output of the energy source, a temporary energy buffer (e.g. C_{in}) is used to accumulate the harvested energy so as to provide supply voltage to the converter. Input capacitor C_{in} of 100nF and output capacitor C_{out} of 1nF were used.

A detailed schematic of the stage (St) is shown in Fig. 2.4b. The St consists of a voltage doubler, a dual-series PMOS switch (M_{p1} and M_{p2}), and two non-overlapped complementary signals (CLK and CLKB). The voltage doubler includes a cross-coupled NMOS pair (M_{n1} and M_{n2}), and two pumping capacitors. The voltage doubler allows the capacitors' nodes to swing between input voltage (IN) and output voltage (OUT), which is equal to 2×IN. The same stage circuit (St) is used for both first stage and shared stage, except that some

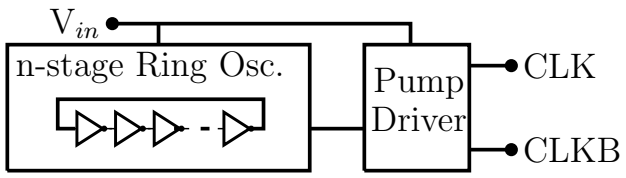

Figure 2.5: Block diagram of the driver circuit.

parameters (e.g. pumping capacitor, transistor size) are different. For evaluation purpose, the pumping capacitor of $20pF$ for the first stage and of $60pF$ for the shared stage were used. The transistors are sized accordingly to meet the requirement on output voltage.

The block diagram of the driver circuit is shown in Fig. 2.5. The driver consists of a n-stage ring oscillator and a non-overlapping clock generator. The n-stage ring oscillator, whose supply voltage is obtained from the energy source, generates a clock for the non-overlapping clock generator to generate two non-overlapped complementary clocks (CLK and CLKB). The clock generator includes two NAND gates, a transmission gate, and a couple of inverters. The switches at the St circuit are not turned on simultaneously, which are controlled by the non-overlapping clocks. As a result, power efficiency degradation is kept low.

2.6 Results and Discussion

The proposed power converter was evaluated in a $0.13\mu m$ CMOS process. For simulations throughout this work, a 800 mV input voltage source in series with a $1k\Omega$ internal resistor was used to emulate the energy source.

In order to evaluate power extraction from the energy source, we vary the number of first stage in the proposed power converter. The voltages and currents at the input of the converter under different numbers of first stage units are monitored once a load resistor of $10k\Omega$ is connected, as shown in Fig. 2.6. The input voltage at the converter decreases with the increase in the number of the first-stage, while the input current increases when adding

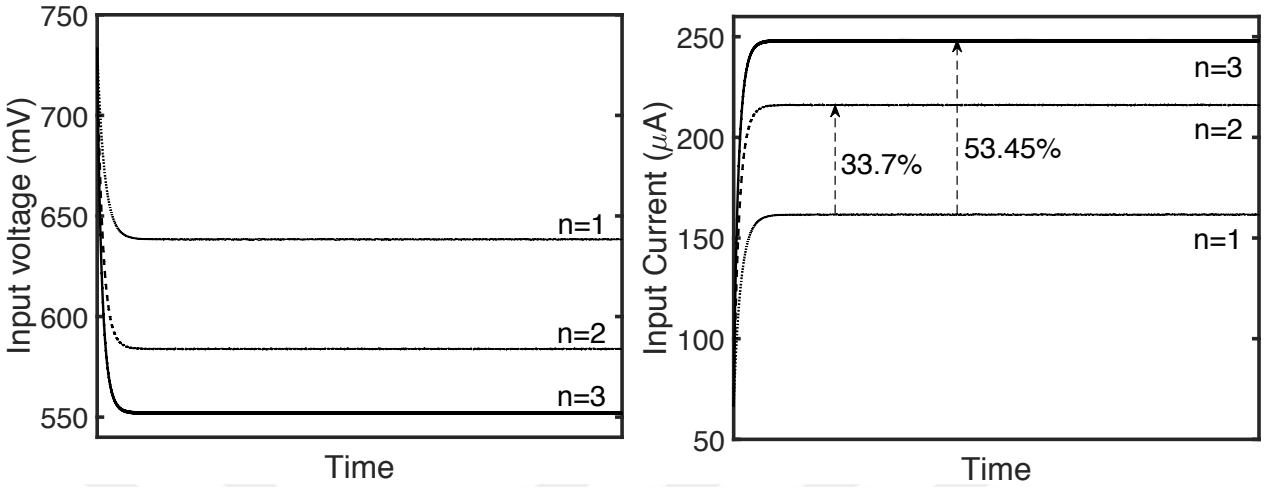

Figure 2.6: (a) Input voltage of the proposed converter under varied number of first-stage. (b) Input current of the proposed converter under varied number of first-stage.

more first stage units. The converter with three first stage units draw 53.45% more current from the energy source than the conventional converter with one first stage. Once one first stage unit is employed, the power of 103μW is extracted from the energy source. When three first stage units are used, the extracted power is 137μW, which is 33% more. Under varied loads, the improvement of extracted power with proposed converter (e.g. $n = 3$) over the conventional converter (e.g. $n = 1$) ranges from 17% to 61%. As a result, the proposed converter with three first stage units approaches very close to the MPP than the conventional converter.

Fig. 2.7 shows the proposed converter output voltage as a function of its output current under different numbers of first stage units. In the light load mode, although conventional converter (e.g. $n = 1$) has larger output voltage than the proposed one, their output currents are nearly close to each other. The reason varied output voltage in the light load mode is that the proposed converter extracts more power than the conventional one. Drawing more current from energy source is obtained as number of the first-stage is increased. Therefore, the input voltage of the conventional converter is higher than the proposed ones. However, in the heavy load mode, the proposed converter has better output voltage and current than

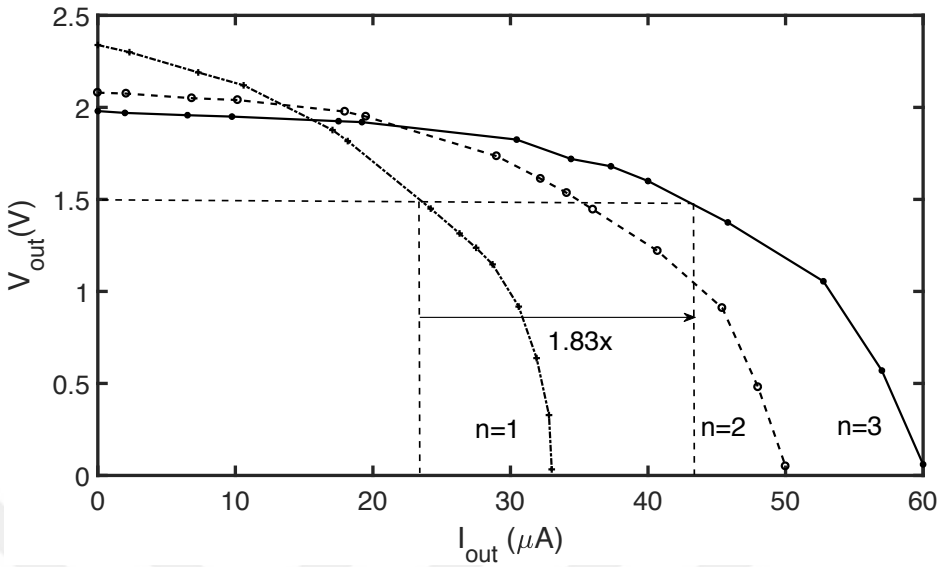

Figure 2.7: The proposed converter output voltage as a function of its output current under varied number of first-stage.

the conventional one. The proposed converter improves the maximum output current by 183% as compared to the conventional converter. As mentioned, the proposed converter extracts more power from the energy source. As a result, the proposed converter shows better power output closer to the MPP than the conventional converter. Fig. 2.8 shows the power efficiency as a function of output current under different numbers of first stage units. Although the conventional converter exhibits better efficiency than the proposed one at the light load mode, the conventional converter has worse efficiency than the proposed converter at the heavy load mode. Heavy load requires more power than low one. The proposed converter extracts more energy than the conventional one from energy source. In the heavy load mode, the conventional converter transfers less power to the output, so power degradation is increased. The maximum efficiencies obtained from the proposed and conventional converter are 53.3% and 38.5%, respectively.

However, the peak end-to-end efficiency (see (2.12)), which is the ratio between the power obtained at the load and the maximum power available from the energy source, varies for the proposed and the conventional converter, whose efficiencies are 39.6% and 20%, respectively.

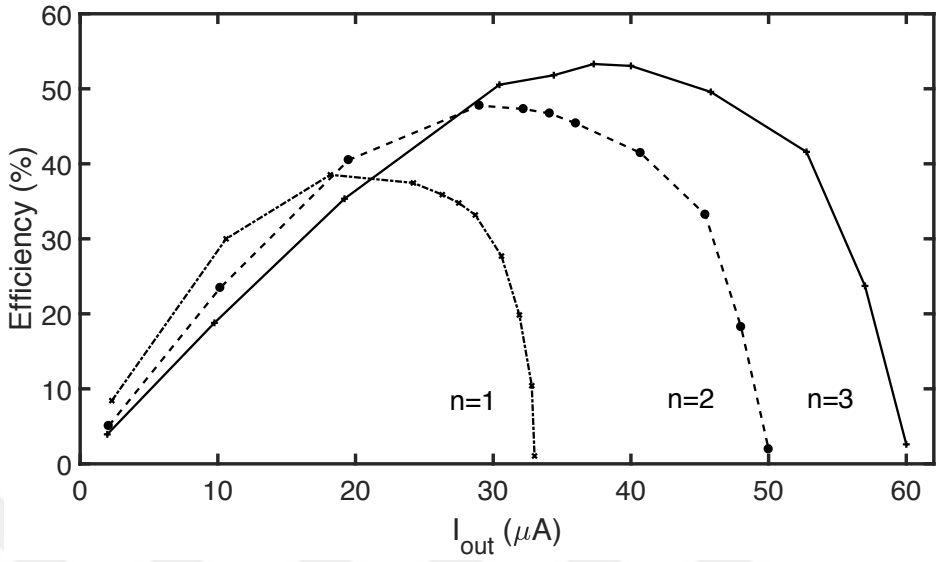

Figure 2.8: The efficiency of the proposed converter under varied number of first-stage.

This indicates that the proposed converter improves the end-to-end efficiency by 98% as compared to the conventional converter. Transfferring more energy to the load is achieved at the proposed converter because more energy is extracted from energy source.

$$\eta_{end} = \frac{P_{in}}{P_{max}} \times \frac{P_{out}}{P_{in}} = \frac{P_{out}}{P_{max}} \tag{2.12}$$

2.7 Conclusions

This chapter presents an inductorless power converter for energy harvesting. As compared to conventinal capacitive based power converter, the proposed power converter is divided into two parts; first-stage and shared-stage. First-stage is the maximum power extraction stage by connecting a number of first-stage in parallel. First-stage achieves maximizing power extraction without increasing power dissipation and circuit complexity except increasing area. Shared-stage operates as conventional charge pump to step-up the merged output voltage of a number of first-stage to a usable level by the application. Maximum power extraction is analyzed. Design methodology and optimization are discussed and incorporated

into circuit implementation. The extracted power from energy sources enhances by range from 117% to 161% over the conventional design. The proposed inductorless power converter improves the end-to-end efficiency by 98% as compared to the conventional converter. The proposed inductorless power converter achieved maximizing power extraction is specifically targeted from not only low power energy source but also high power energy source as well.

Chapter 3

Energy Combiner Architecture for Multiple Microbial Energy Harvesting Sources

The main purpose of deploying MFCs as a power supply is to accomplish long-term autonomous operation in underwater devices. However, due to their low output voltages, MFCs might not be able to directly power up loads. Single MFC in general does not have sufficient output voltage to operate a connected load, even though an up-converted power converter is employed among them. Thus, multiple MFCs connected to the load through multiple power converters can achieve better reliability and functionality for energy harvesting [49], [2].

As the power output of MFCs strongly depends on the environment, even identically designed MFCs (i.e. same size and physical structure) will generate different output voltages [9], [1]. The discrepancy at MFC outputs can be explained by the nonlinear effects of microorganisms during inoculation [50], [1], [10]. Some previous studies have discussed the combination of multiple MFCs for enhanced power output [49], [2], [11] [40], but they did not considered the variations in output voltages and how this will affect the power transfer cycle, i.e., synchronizing the output power cycles of different MFCs simultaneously. As a result, the overall efficiencies of these works are limited by the highest generated voltage, whereas the lower generated voltages are not exploited at their best efficiencies. To overcome

these problems, this study develops a more efficient method for combining multiple microbial energy harvesting systems, as shown in Fig. 3.1b.

3.1 System design considerations

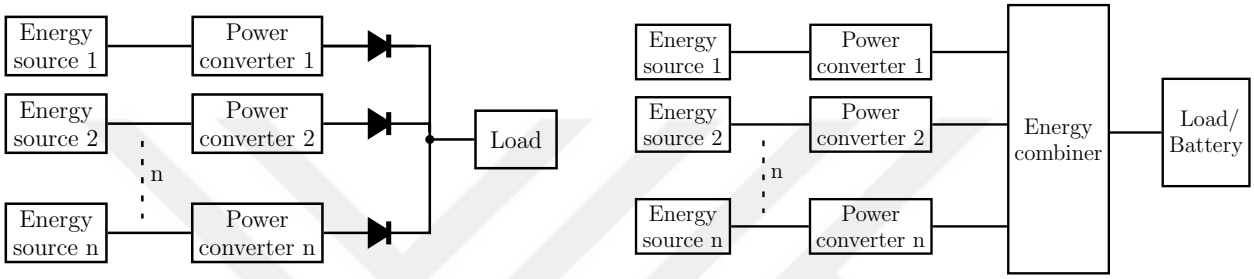

Figure 3.1: (a) The block diagram of a conventional energy combiner circuit. (b) The block diagram of the proposed energy combiner circuit.

Driving an external load through a power converter by single energy source, e.g., MFC, might not be an effective solution to exploit energy harvesting due to the irregularity in energy flow. Efforts to utilizing multiple energy sources can assist to either power up the load or minimize the limitation on load operation. By combining multiple energy sources of the same or different types, it is possible to increase the overall output power and enhance the system reliability [51], [52], [53], [54], [55], [56], [57], [58], [59], [60], [61], [62].

Traditional energy combiner designs for multiple energy sources are achieved by simply combining their outputs to a common output node directly or through a unidirectional switch (e.g., a diode) [53], [54], [55], so called power ORing, as shown in Fig. 3.1a. Instead of selecting the source with either the maximum instantaneous power [63] or in-order [56], [57], proposed energy combining method offers simultaneously energy harvesting from multiple energy sources. Furthermore, this method is truly self-starting, which is different to many previous works [56], [57] that need external power sources to launch their operation until enough voltage is obtained.

Although the conventional energy combiner design provides some advantages, there are some issues inherent to such circuit, such as (1) powering the load with multiple energy sources without sharing between them but simply providing the load with the highest supply voltage, thereby limiting the overall efficiency as it excludes the contributions from other supply voltages (i.e., just one energy source supplies the load), and (2) the power loss associated with the diode voltage drop affects the overall efficiency.

In this study, a more efficient method is developed. The key idea is to place an energy combiner circuit before the load (e.g. a sensor) to overcome these issues, as shown in Fig. 3.1b. The energy combiner circuit operates in a time-multiplexed manner to manage the energy transfer to the load. For multiple (e.g., n) energy sources, the power converter outputs PC_1 to PC_n connect sequentially to the load, thereby resulting in an n time-multiplexed operation. This allows all energy sources to contribute to the power-up of the load. Also, it precludes converters with different output voltages to concurrently connect to the load in order to eliminate charge leakage from the load to some converters.

3.2 The proposed energy combiner for multiple microbial fuel cells

3.2.1 Power converter

Energy sources are usually not connected to the energy combiner circuit directly due to the inherent low voltage at their outputs. Thus, an interface circuit (e.g., power converter) is required to up-convert the low output voltage to a usable level for the load. The circuit block diagram of the power converter in this work is shown in Fig. 3.2 while Fig. 3.3 illustrates the waveforms of the control signals of the switches and the current flowing in the inductor as well as the switches. A switching inductor converter is employed as the power converter, which includes a start-up circuit, a output regulation circuit, a signal generator, power transistors

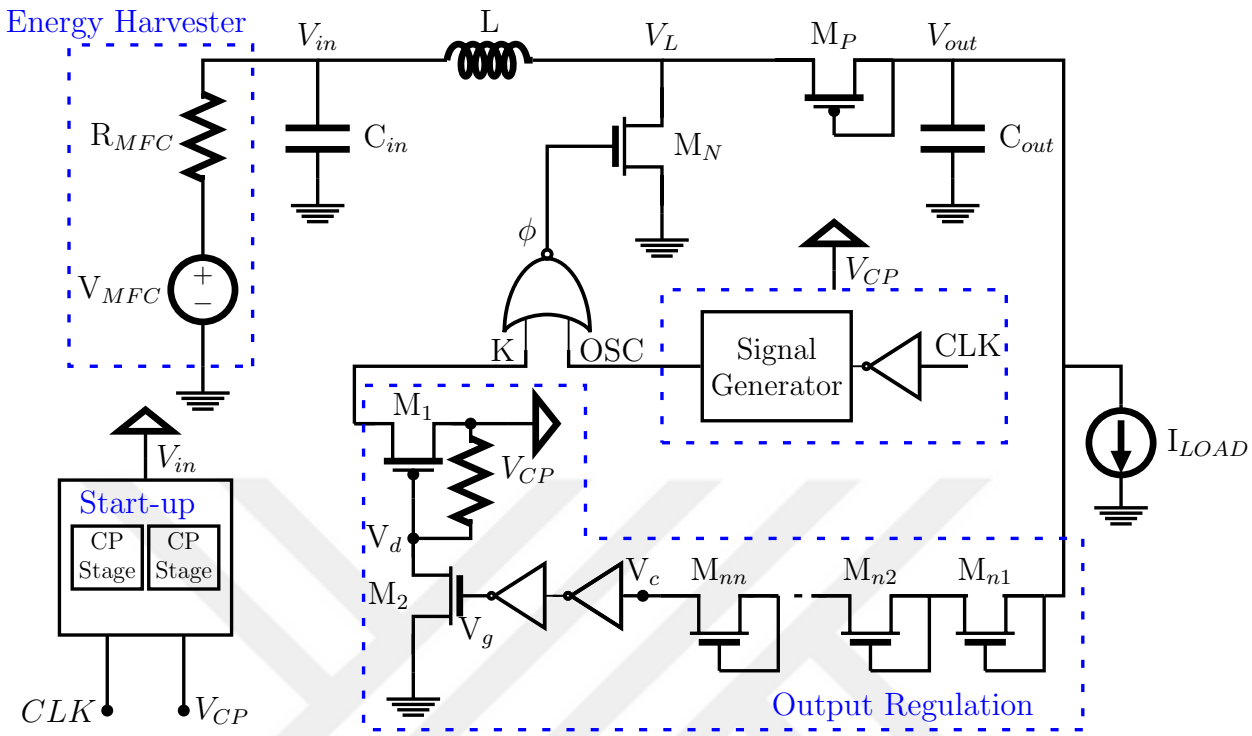

Figure 3.2: Implementation of the power converter circuit.

and other components.

The voltage at the output of the energy source is insufficient to support the operation of the power converter, as the threshold voltage of CMOS transistors is typically higher than the source output voltage. Therefore, a start-up circuit is needed to boost the low voltage to a sufficient level to enable CMOS transistors. The start-up circuit is designed using a two-stage charge pump to start the operation from the output (V_{in}) of the low-voltage energy source. The charge pump (CP) stage of the start-up circuit is shown in Fig. 3.4. This circuit steps up the output (V_{cp}) to power the control circuit e.g. NOR gate and regulate the output of the main converter for a desired load voltage. The charge pump is driven by a ring oscillator that generates clock signals CLK and CLKB once input voltage V_{in} has sufficient voltage. Note that once there is no sufficient voltage at the input of the converter, the converter does not start-up.

The CLK signal obtained from the start-up circuit is used by the signal generator to

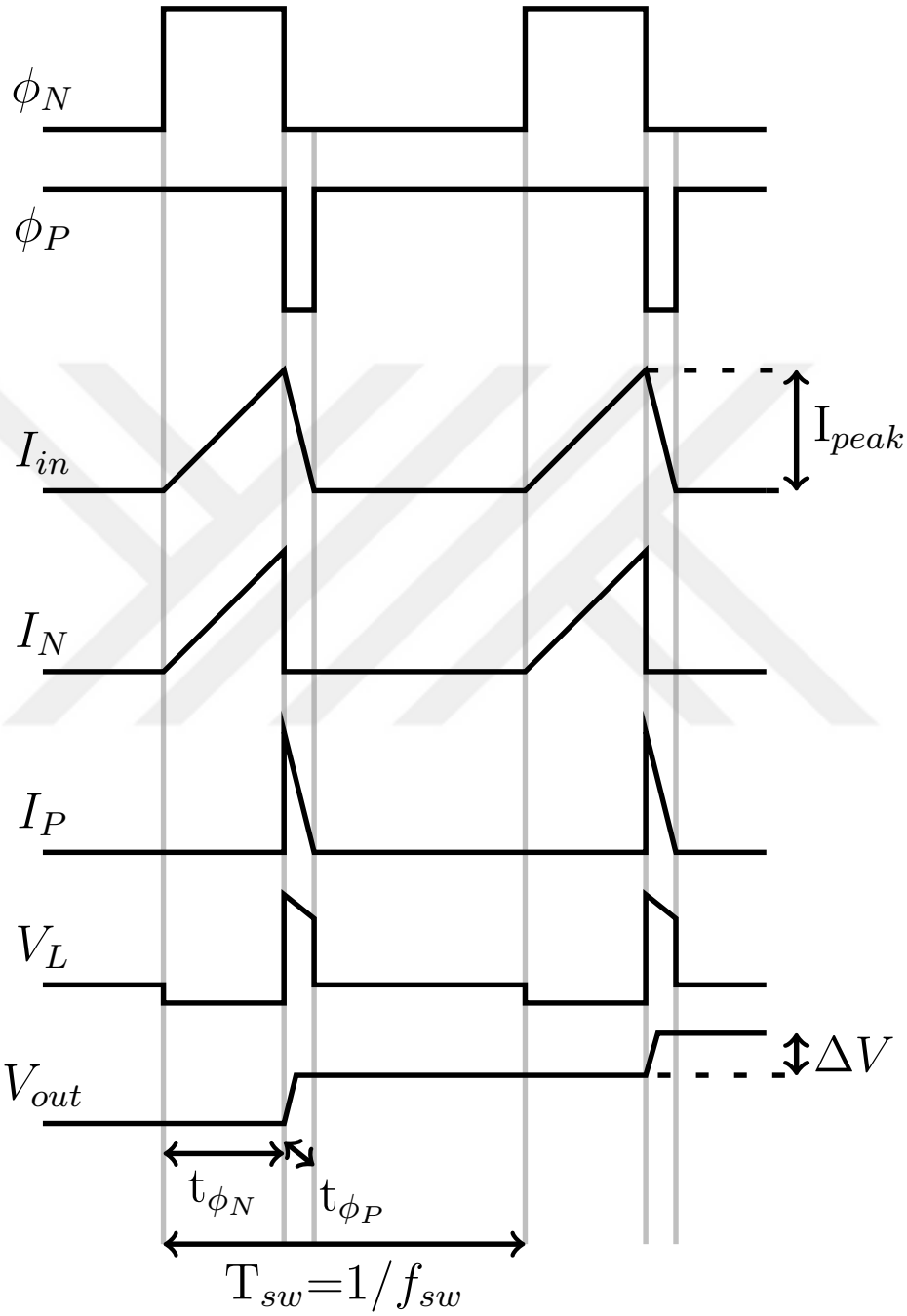

Figure 3.3: Conceptual illustration of waveforms for control signals currents and voltages at swithches and output. The boost converter operates in discontinuous conduction mode (DCM).

generate the OSC signal that feeds the NOR gate input. This controls the on/off behavior of the power transistor M_N. The signal generator creates a 50% duty cycle square wave powered by the output of the start-up circuit V_{cp}. Once M_N is turned on, energy harvester starts charging the inductor L to a maximum current I_{max}. The inductor's peak current is given by

$$I_{max} = \frac{V_{in} \times t_1}{L} = \frac{V_{in}}{2 \times L \times f_s}, \tag{3.1}$$

where $t_1 = 1/2f_s$ and f_s is the switching frequency of the converter.

When M_N is turned off, the stored current in L goes through M_P to charge the output of the converter. The voltage V_L goes high and this voltage is transferred through the PMOS transistor M_P to the output. The voltage at V_L during the duration of t_2 is given by

$$V_L = \frac{V_{in} \times (t_1 + t_2)}{t_2}. \tag{3.2}$$

Note that the voltage V_L depends on the input voltage and the values of t_1 and t_2. These processes repeat periodically over time.

Before V_{outc} reaches the desired level, the output regulation circuit sends 0 to the NOR gate. As a result, the NOR gate output ϕ is the inverse of the signal generator output. Once V_{outc} exceeds the desired level, the output regulation circuit feeds the NOR gate input with V_{cp}. This keeps M_N in the off stage until V_{out} discharges enough to start up again, which changes M_N to the on stage. This process repeats over the time.

The power converter forms an energy transfer bridge from the low-voltage (as low as 0.3V) output of the energy source to the high voltage (around 1.5V) at its output. The output regulation circuit regulates at an output voltage level of 1.5V. The regulation circuit as shown in Fig. 3.2 is based on the gate-drain connected transistor scheme to maintain the output voltage at the desired point. Once the voltage is reached at the output of the boost converter, this voltage through the gate-drain connected transistors will drop across

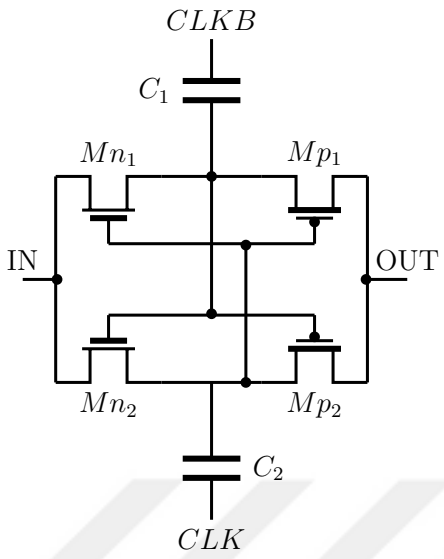

Figure 3.4: The CP stage in the start-up circuit.

the transistors. The voltage at the source of the M_{nn} transistor, V_c, is given by

$$V_c = V_{outc} - n \times V_{gs} \tag{3.3}$$

Note that M_{n1}–M_{nn} transistors have the same size. The voltage at V_d is equal to V_{cp} since the resistor acts as a short circuit. This keeps the PMOS transistor $M1$ in the off state.

Once V_c exceeds the inverter pull-down transistor threshold voltage V_{thpd} (i.e., $V_{g1} \geq V_{thpd}$), the voltage at V_g goes high and $M2$ becomes conducting. Note that inverters are used to enable quick switching while not causing delay or inappropriate transitions at V_g. The gate voltage of the PMOS transistor $M1$ drops to zero, and hence the drain of $M2$ is connected to ground. The resistor whose value is 10Meg acts as a linear element to supply current to the gate of the $M1$ transistor. The pull-up resistor also helps in discharging the gate capacitance of M1. The $M1$ transistor conducts and sends the signal to the control circuit. Substituting $V_c = V_{thpd}$ into (3.3), the output voltage at the boost converter is given by

$$V_{outc} = (n) \times V_{gs} + V_{thpd}. \tag{3.4}$$

This is a very simple way to regulate output voltage instead of using more complex circuits. The proposed regulation circuit eliminates the need for a reference voltage generator circuit and a comparator with the voltage divider scheme. In addition, the proposed circuit consumes very small power (less than $305nW$ as discussed in Section 3.3).

3.2.2 Energy combiner

Some previous studies have discussed how to combine multiple MFCs for enhanced power output [49], [2], [11], [40]; however, these works did not considered the variations in different output voltages and how these variations will affect the power transfer cycle, i.e., synchronizing output power cycles of different MFCs simultaneously. Variations in the output voltage of each identically designed MFCs cause different on/off frequencies in the converter to control the switch M_N. This results in different discharge times to transfer the current stored in the inductor L to the output PC_i ($i = 1$ to n), which reduces the overall efficiency. In this study, this problem is addressed by using the proposed energy combiner circuit, as shown in Fig. 3.1b. The energy combiner allows all energy sources to simultaneously operate and connect to the power converters. The converters will not connect concurrently to the load or battery. Instead, the energy combiner circuit operates in a time-multiplexed manner to manage the energy delivery to either load or battery.

An energy transfer cycle T_{ci} defines the time in which the stored energy at the output of each power converter is transferred in the order of connection (e.g., PC_1 first, then PC_2 and so on). They can be expressed as

$$T_{c1} = T_{c2} = ... = T_{cn} = T_c, \tag{3.5}$$

$$T_{off} = (n-1) \times T_{ci}, \tag{3.6}$$

where T_{off} is the time duration that no energy is transferred and n is the number of energy

sources (and converters). This gives

$$.T = T_{ci} + T_{off} \tag{3.7}$$

Substituting (3.5) and (3.6) into (3.7), we obtain

$$T = T_{ci} + (n-1) \times T_{ci} = n \times T_c. \tag{3.8}$$

Due to the variations in output voltages, different amount of charges are fed into the output capacitor C_{out_i} by each converter, resulting in charge leakage from the highest voltage (i.e., load) to the lowest voltage power converter output once time-multiplexing allows the output converter connection. Thus, it is needed to reduce the leakage and direct the stored energy to somewhere in order to keep overall efficiency nearly constant. To achieve this, energy can be directed either to a load or to a battery. If the connected converter output voltage is higher than the load, energy is directed toward to the load, otherwise toward to the battery. The energy storage element battery is used to store the extra energy if the available input power is larger than that required by the load. The detailed explanation of this process will be given in Section 3.2.4.

3.2.3 Circuit implementation

Fig. 3.5 shows the circuit implementation of the proposed energy combiner with $n = 4$ for illustration. The outputs of the converters PC_1 to PC_4 are connected to the transistors M_{c1} to M_{c4}, which are controlled by a switch matrix generated by a digital control unit (DCU). Fig. 3.5a shows the block diagram of the DCU. $CLK2$ signal is generated from the CLK signal, which is the output of the start-up circuit (see Fig. 3.2) of one energy source. $CLK2$ is used as a clock source in a 4-bit counter. The output of the counter feeds into a 4-bit serial-in parallel-out shift register and some primitive logic gates to generate transistor

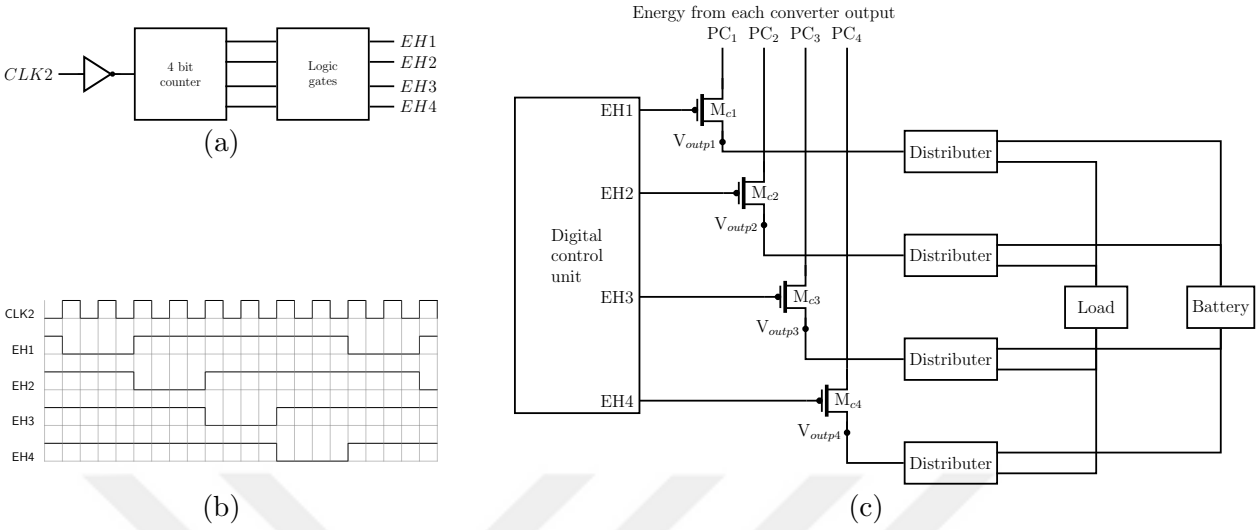

Figure 3.5: (a) The block diagram of digital control unit (DCU). (b) Timing diagram of DCU. (c) Implementation of the energy combiner circuit with four energy sources.

control signals $EH1$ to $EH4$. The expected DCU output is shown in Fig. 3.5b.

Once the output converter PC_i is connected, the power of the corresponding switch EH_i goes low, but other switches keep high, pulling the switch M_{ci} to the ON status while leaving others in the OFF status. Thus, the output connected to the energy direction distributer decides the next connection, either the load or the battery. The same steps are repeated for other converter outputs. Note that while four energy sources are used in this paper, it is straightforward to extend to more energy sources.

3.2.4 Energy direction distributer with control circuit

The energy combiner circuit performs in the order of connection and directs the corresponding converter output to either the load or the battery, as described in Fig. 3.6. Once the i^{th} transfer cycle is activated, the output is ready to transfer the stored energy at PC_i to the energy distributer circuit (see Fig. 3.5c). The corresponding input of the distributer V_{outpi} is compared with the output of the distributer control circuit V_{reg} (see Fig. 3.7b). If V_{reg} is larger than V_{outpi}, then the result of $V_{reg} - V_{outpi}$ is smaller than the threshold of transistors

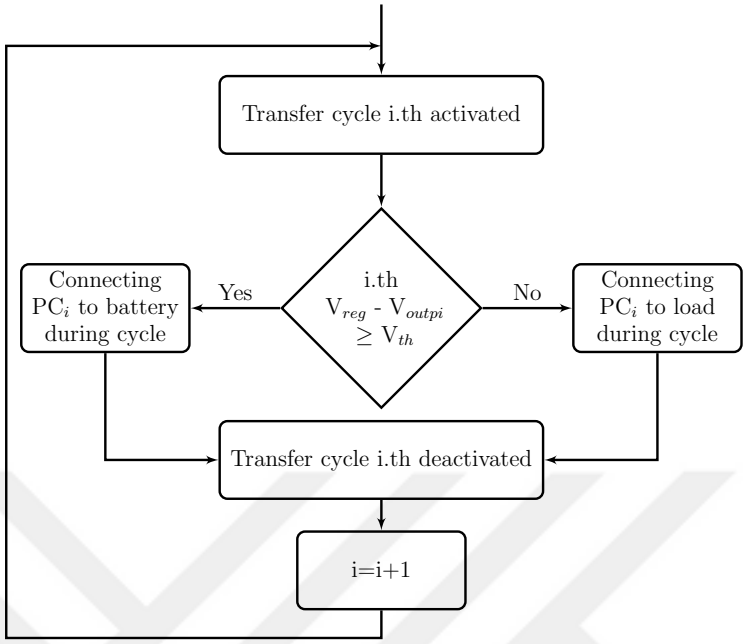

Figure 3.6: Control flow of the proposed energy direction distributer.

in the distributer circuit. The corresponding output of the converter is connected to the load in the time of T_{ci}; otherwise it is connected to the battery. At the end of the energy transfer cycle T_{ci}, the stored energy at the converter output stops to transfer; i.e., transfer cycle i^{th} is deactivated. Next, the following transfer cycle $(i+1)^{th}$ is activated and the above process is repeated. This is precisely what the distributer circuit operates.

The energy distributer is designed with single input (V_{outpi}) and dual outputs, which are the battery and the load, as shown in Fig. 3.7a. The circuit is based on two transistors controlled by the output of the regulation circuit, as shown in Fig. 3.7b. The control circuit is used to sequentially route n energy distributer circuits towards the load or the battery.

As the load output capacitor initially charges up, the PMOS transistor M_k is cut off. The charge at the outputs of the converters are sequentially transferred by the energy combiner circuit to the load. The voltage of the output passes through n gate-drain connected MOSFETs that act as diodes to drop voltage across them. The source voltage of the M_n

transistor is obtained by

$$V_s = V_{out} - k \times V_{gs}. \tag{3.9}$$

When V_s is sufficiently high (e.g., equal to V_k, which is the first inverter pull-down transistor threshold voltage) to connect the output of the first inverter to ground, the drain of the M_m transistor connects to ground and then M_k PMOS transistor turns on. The energy at the input of the corresponding distributer circuit is delivered to the energy storage (e.g. battery). Substituting $V_s = V_k$ into (3.9), the output voltage of the load can be expressed as

$$V_{out} = k \times V_{gs} + V_k \tag{3.10}$$

Once the voltage at the load drops below to the desired level, M_k transistor turns off and the energy is delivered to the load again.

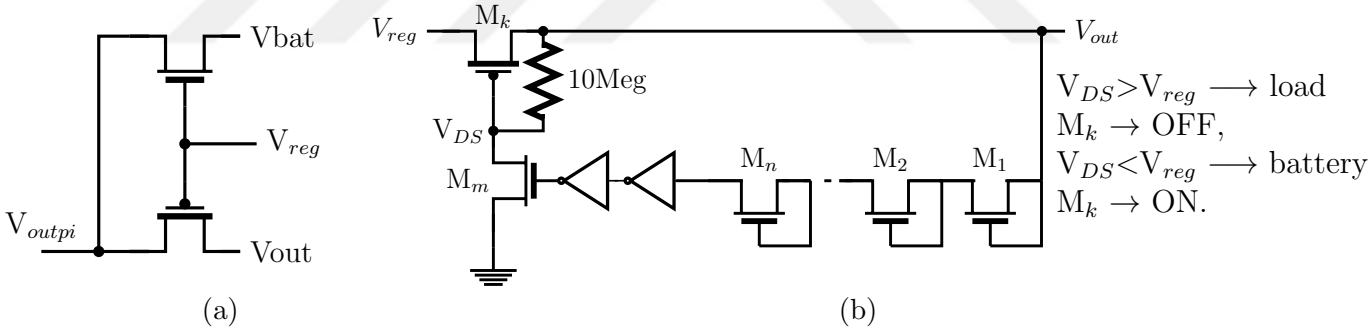

Figure 3.7: (a) Energy distributer circuit. (b) Energy distributer control circuit.

3.3 Results and discussion

To evaluate the proposed technique, an energy combining circuit for multiple microbial fuel cells was designed and simulated using a 0.13μm CMOS process. Four identical sediment MFCs [49] were deployed as the energy sources. The variations on the output voltages

were simulated by an analytical model of the MFCs [1], which also emulated the output power/voltage of the MFCs. The power converter uses a 20μH inductor L, a 4.7μF output capacitor C_{out}, and a 470μF input capacitor C_{in}. These components are the same for other three converters used in the circuit. For demonstration purpose, a resistance of 1kΩ is used as the load.

The first set of simulations was carried out for one power converter to show its operation and performance. Figure 3.8 shows the voltage waveforms of the output regulation and control circuits. Initially, the output voltage of the converter V_{out} is zero. Once the MFC is connected to the converter, V_{out} is gradually charging up to the desired voltage. Meanwhile, V_c (in Fig. 3.2) is slowly increasing to reach the inverter pull down transistor threshold voltage. As V_c slightly exceeds the threshold voltage, V_{cp} is allowed to feed the NOR gate input K until V_{out} is discharged to below the desired voltage. The output of the converter starts to charge back to slightly over the desired voltage by the MFC through the converter. The same process is repeatedly over the time (see Fig. 3.8). Before V_{out} reaches the required level for the load (a model of hydrophone is used here), the converter switches the inductor by the frequency of f_s. Once V_{out} reaches the required voltage, the converter switch the inductor less due to output regulation.

Figure 3.9 shows the voltage V_L in Fig. 3.2 and the current through the inductor. It takes 2.5μs to charge the inductor to the maximum current which is 50.1mA according to (3.1). On the other hand, it takes 700ns for the inductor to discharge through the M_P PMOS transistor to the output of the converter, which reduces the inductor current to zero. The inductor current is not allowed to flow negatively due to the implementation of the DCM converter in this study. The voltage at V_L is at 1.96V which is the expected value from (3.2).

Fig. 3.10 shows the voltage waveforms for input (V_{in}) and output (V_{outc}) of the converter and the start-up output (V_{cp}). The output voltage of the MFC is around 0.41V, whereas the the output voltage of the converter was regulated at 1.55V. The output voltage introduces less than 1% supply voltage variation to the load.

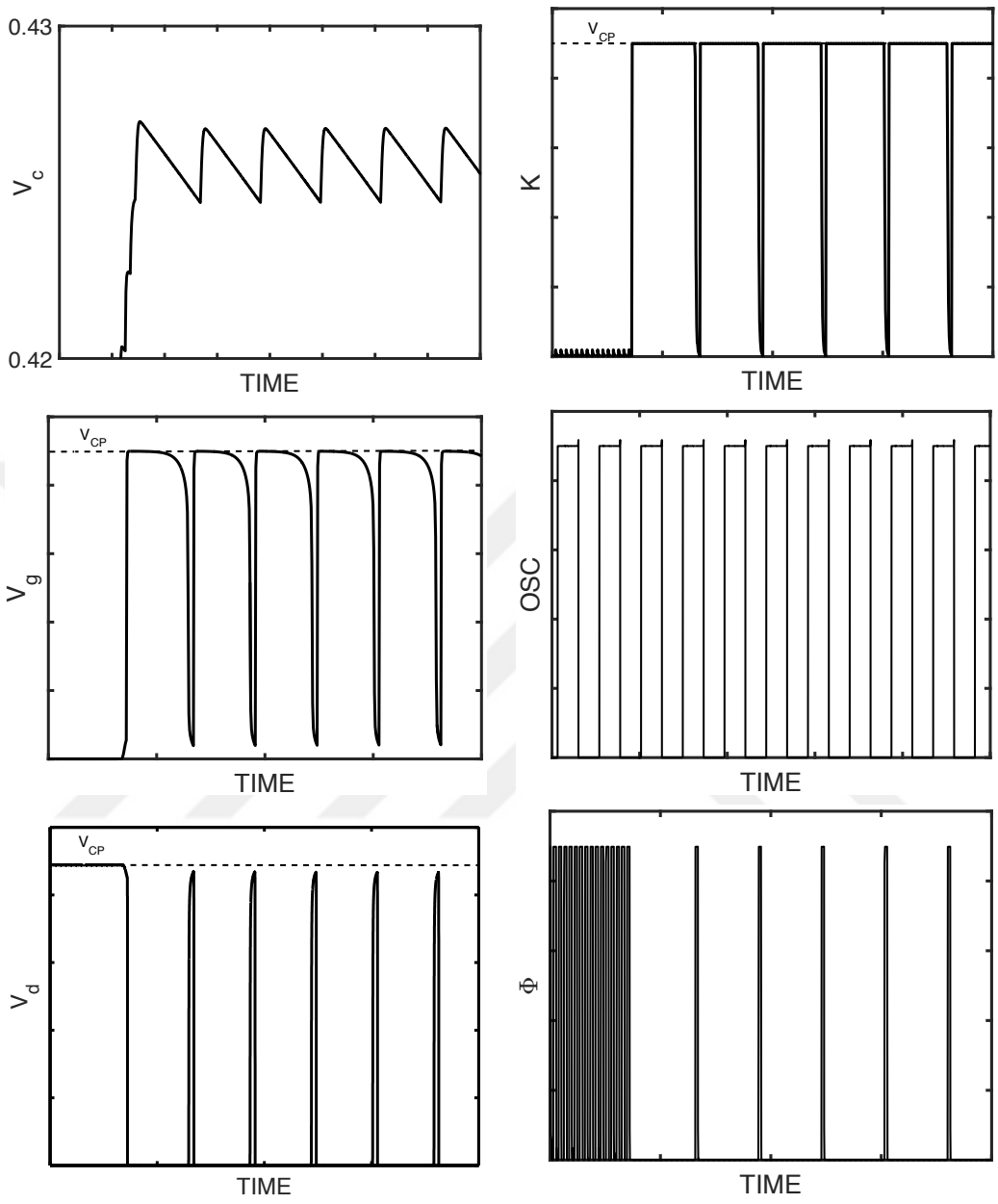

Figure 3.8: Waveforms at different circuit nodes of the output regulation and control circuits (see Fig. 3.2).

In addition, the efficiency and switching frequency of the power converter are investigated by varying input voltage as shown in Fig. 3.11. It is clearly to see that small variations in the input voltage result in different efficiencies and generate different frequencies. The variations in the frequencies cause different voltages V_{outci} at the output of the power converter. The

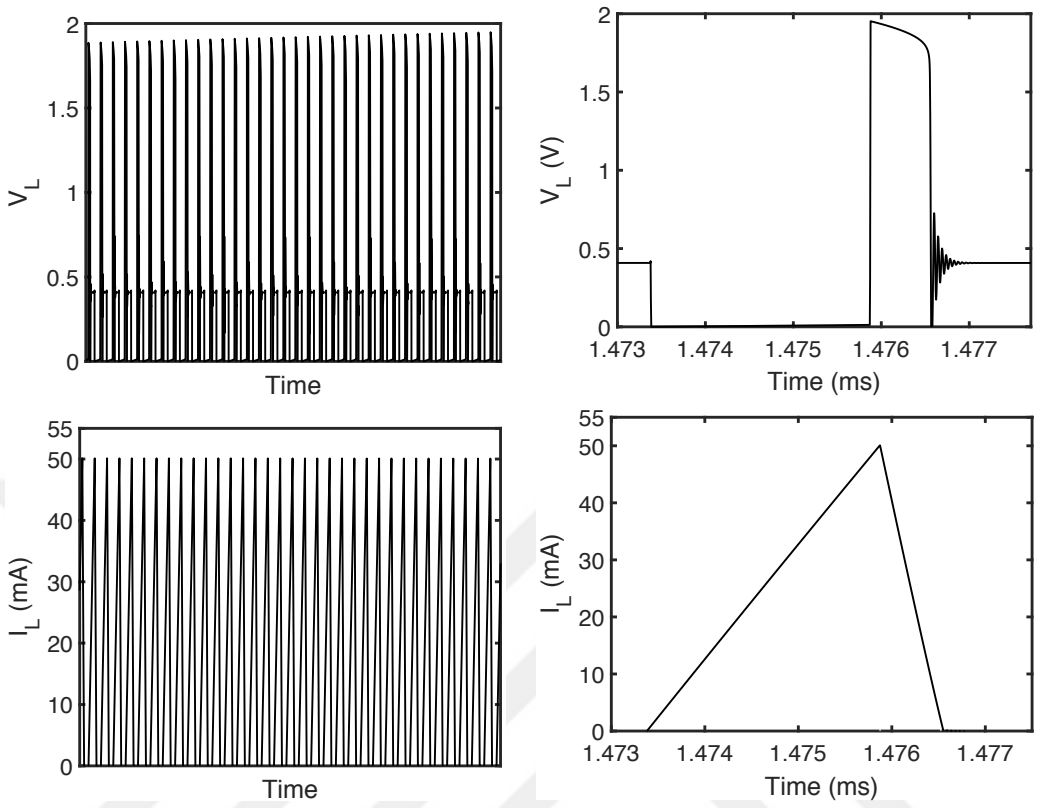

(a) Waveforms (b) Zoomed waveforms

Figure 3.9: Voltage waveform at V_L and current at the inductor I_L.

different voltages at the output of the converters are also due to difference in threshold voltages of the transistors in regulation block among different converters.

The second set of simulations was carried out for the conventional energy combiner to show all system operation. Four identical power converters using the same design parameters up-converting their outputs through the energy sources (e.g., MFCs) are connected to the load without diodes implementations taken placed in Fig. 3.1a. One additional component in the power converters is an output capacitor of 18.8μF in parallel with the load of 1kΩ. The output voltage at the connected load is shown in Fig. 3.12a. As it is impossible to see the contributions of all output voltages at the converters to the load, the input currents of the converters (i.e., MFCs output currents) should be monitored. The currents are shown in Fig. 3.12b. Before the output voltage reaches to the regulated voltage level, all energy

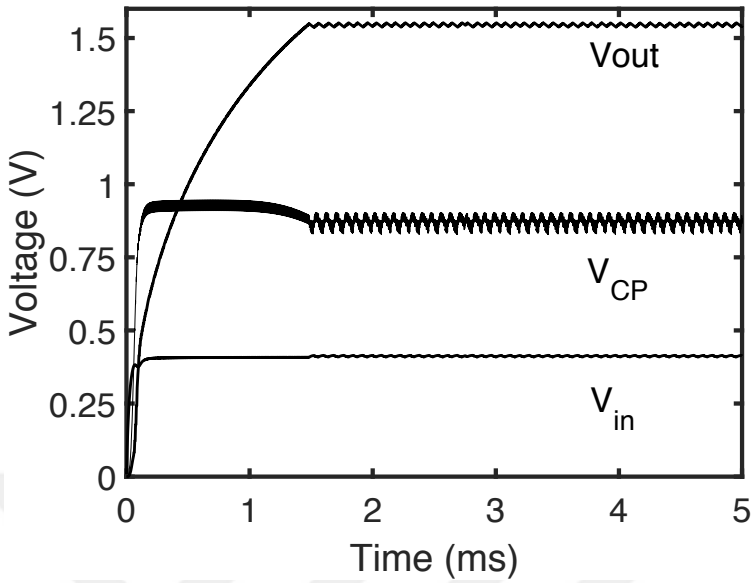

Figure 3.10: Voltage waveforms of input voltage, start-up circuit output voltage and output voltage.

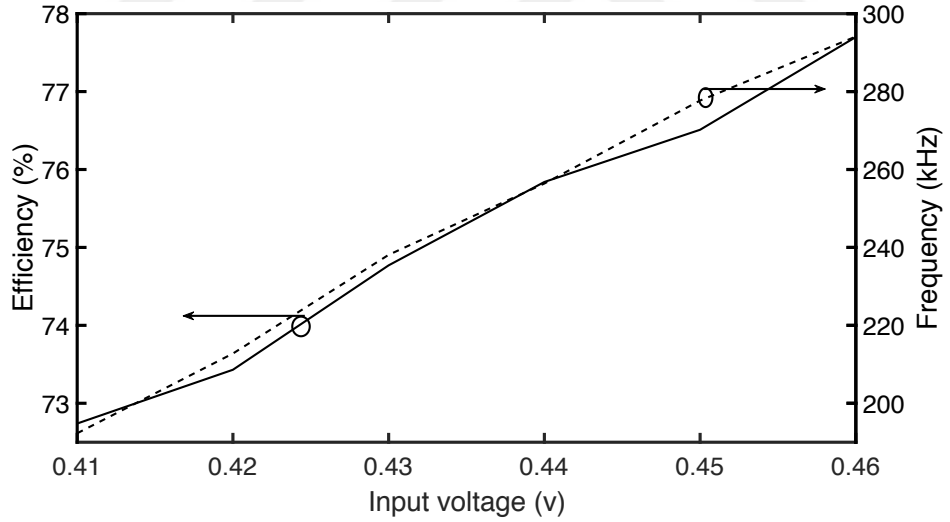

Figure 3.11: The efficiency of the power converter by varying input voltage V_{in} and V_{in}-frequency relationship.

sources contribute to the energy transfer to the load. All converters draw currents from their connected energy sources; thus, all converters operate in the active mode and harvest energy from all energy sources at the same time. However, once the output voltage reaches to the regulated level, three energy sources stop transferring their harvested energy to their

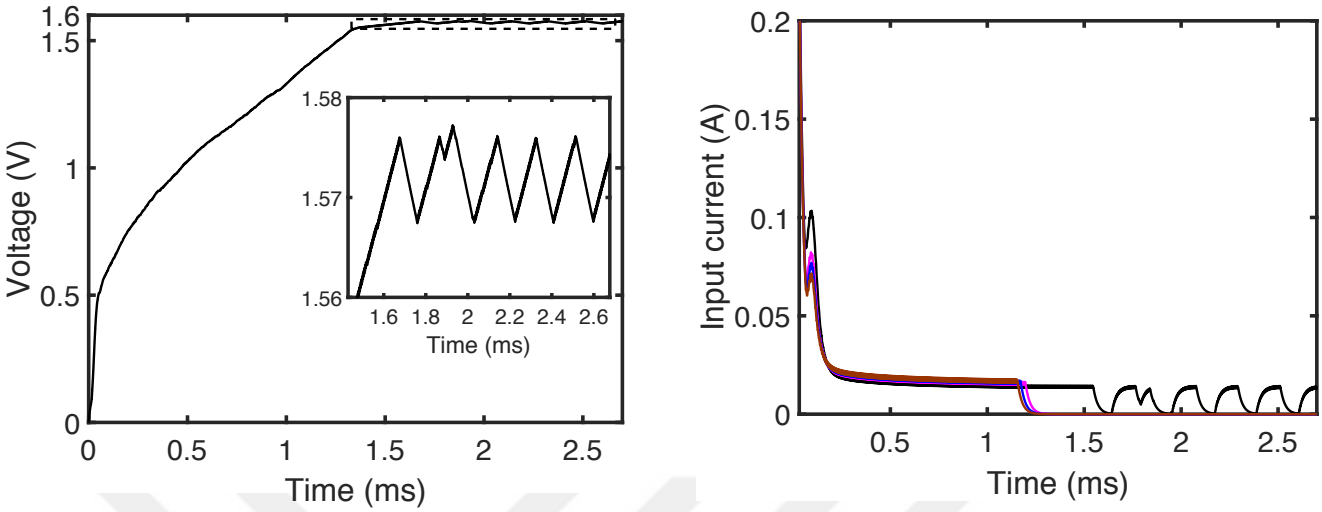

Figure 3.12: (a) Output voltage. Inserted waveform shows the ripple of the output voltage. (b) Input currents of power converters (currents at the outputs of the four identical MFCs.)

converters. The converters input currents drop to zero. This puts the converters in the passive mode. The energy source with the highest voltage consistently transfers the energy to the load. Its converter operates in the active mode and draws current from it. Also, the output voltage is obtained merely from this converter. As a result, conventional combination of all converter outputs (see Fig. 3.1a) leads to energy losses and affects these converters contributing to the output voltage. In other words, the overall system efficiency is degraded as three energy sources are excluded.

The last set of simulations was conducted to show the proposed energy combiner design. Some additional components are a load of 1kΩ in parallel with an output capacitor of 18.8μF, and a capacitor of 20μF is employed as the energy storage which could also be a rechargeable battery. To verify the function of the energy distributer control circuit, its output V_{reg} and control signal V_{DS} in Fig. 3.7b are monitored and their waveforms are shown in Fig. 3.13. It can be seen that V_{DS} is gradually increased by the load output V_{out}. Once M_m transistor in Fig. 3.7b has a sufficient voltage to turn on, V_{DS} quickly drops to zero. Thus, M_k switches ON, i.e., V_{reg} is equal to the load voltage, and then the energy is directed to the battery. Once V_{out} drops to below the desired level, i.e., M_m transistor does not have enough voltage

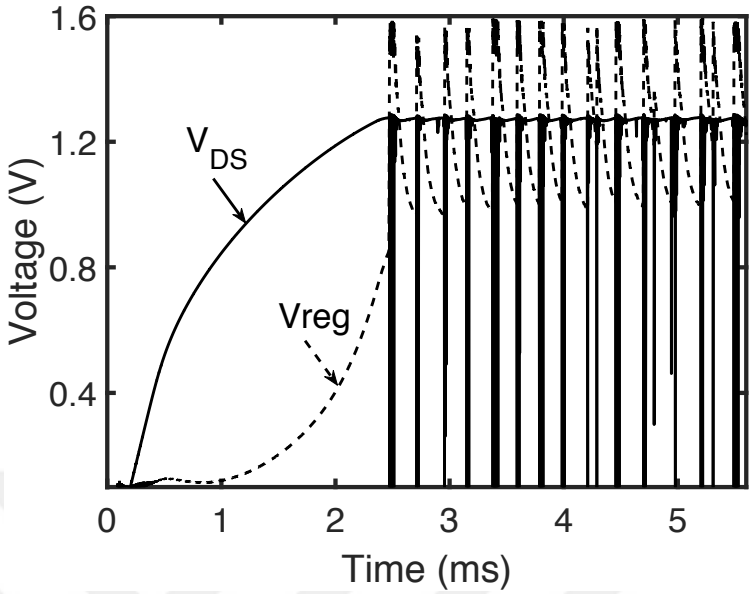

Figure 3.13: Energy distributer control circuit operation and voltage waveforms of V_{DS} and V_{reg}.

to switch on, M_k transistor is OFF and the energy is directed to the load to exceed the level. The same process repeats over the time.

Results of all energy source input voltages V_{in1} to V_{in4}, start-up circuit output voltages V_{cp1} to V_{cp4}, power converter output voltages V_{outc1} to V_{outc4}, load output voltage V_{out}, and energy storage voltage V_{bat} are shown in Fig. 3.14a. It can be seen that the output voltage V_{out} initially starts from zero till power converters start to transfer energy to the output. This is mainly due to the fact that all power converter output voltages are insufficient to change the switch matrix M_{c1} to M_{c4} in Fig. 3.5c. Once sufficient voltages charge the converters outputs, the switch matrix starts to operation as described in Section 3.2.3 and shown in Fig. 3.5b. Their energy is sequentially transferred to the load until the converter output voltages V_{outc1} to V_{outc4} and the load output voltage V_{out} are clamped to more than 1.5V. Before that level, the battery voltage V_{bat} is zero, which means the energy is transferred to the load. After that, the energy distributer control circuit starts to operate and determines where energy will be directed to. It is obviously to see from Fig. 3.14a that the energy storage voltage starts to charge and the control circuit keeps the load output voltage at

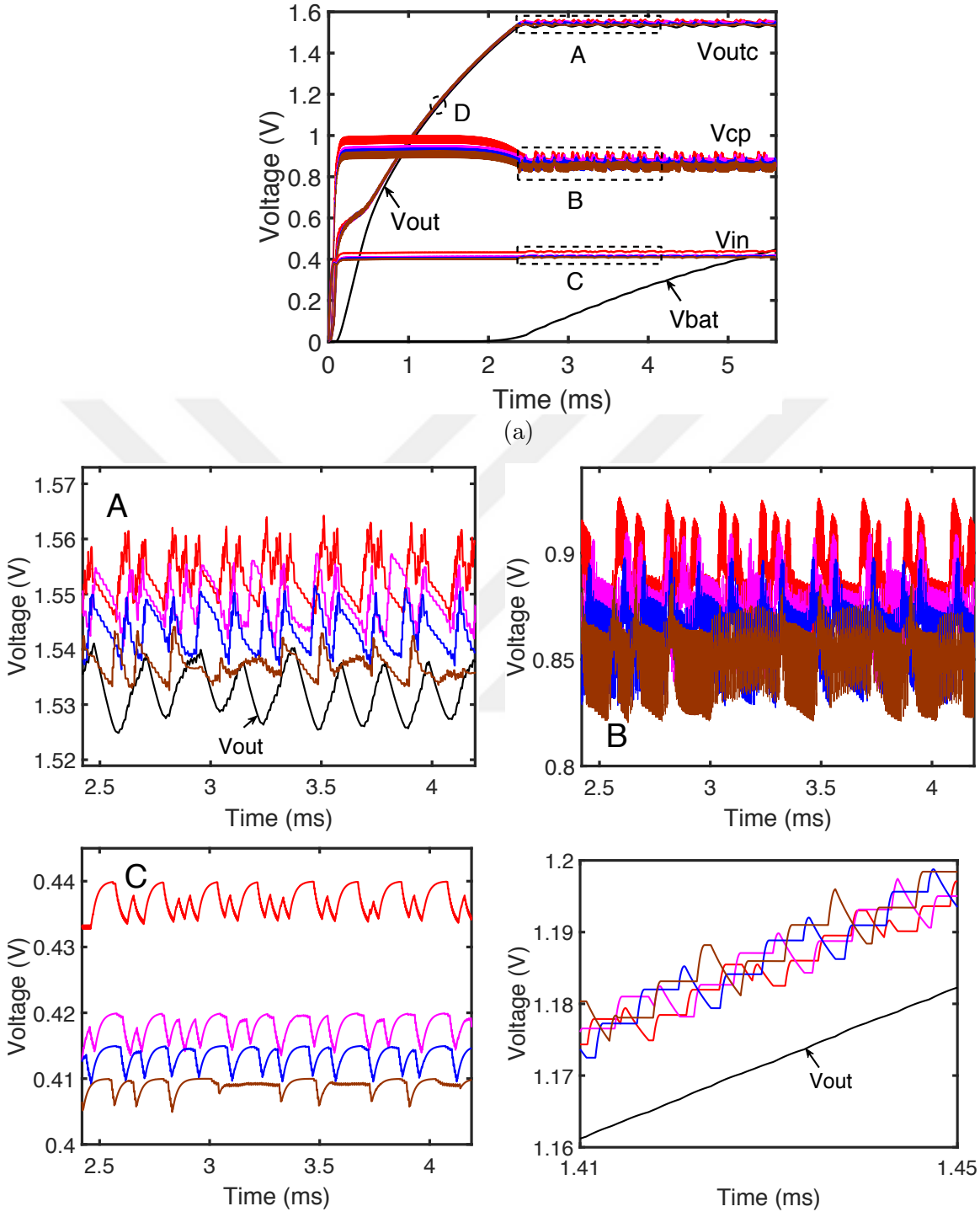

(a)

(b)

Figure 3.14: (a) Voltage waveforms of four energy source (e.g. MFC) input voltages V_{in1} to V_{in4}, start-up circuit output voltages V_{cp1} to V_{cp4}, power converter output voltages V_{outc1} to V_{outc4}, load output voltage V_{out} and energy storage voltage V_{bat}. (b) Zoomed voltage waveforms in areas A, B, C, and D shown in (a).

the desired level. Switching frequencies of the power converters $PC1$–$PC4$ are observed as 245.7kHz, 204.5kHz, 194.17kHz, and 184.84kHz, respectively, due to the variations in their input voltages.

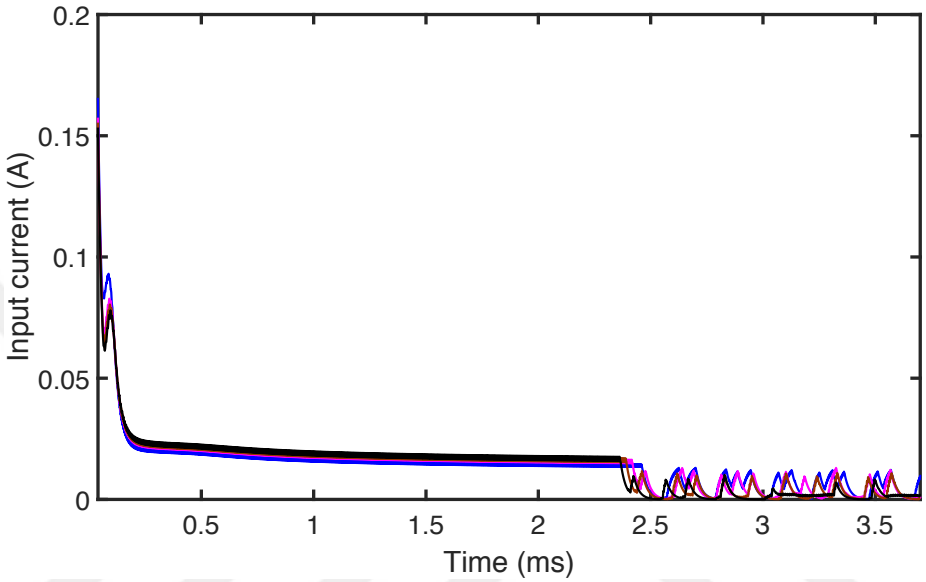

Figure 3.15: Input currents of power converters (currents at the outputs of the four identical MFCs.) in the proposed energy combiner.

The figure at the top left of Fig. 3.14b zooms in the rectangular A of Fig. 3.14a to show converter output voltages and load voltage V_{out} after M_k transistor is first ON in the energy distributer control circuit, i.e., energy is directed either ways. The load output voltage is smaller than all converter outputs. Thus, all energy sources are included in the energy harvesting process. Once the load output voltage is increased from the low value (e.g., 1.525V) to the high value (e.g., 1.54V), all energy sources at that moment are directed to the load; otherwise all energy sources are directed to the battery. The figure at the top right of Fig. 3.14b zooms in the rectangular B of Fig. 3.14a to show all start-up circuit output voltages. The figure at the bottom left of Fig. 3.14b zooms in the rectangular C of Fig. 3.14a to monitor input voltages of the converters, i.e., MFCs output voltages. The figure at the bottom right of Fig. 3.14b zooms in the circle D of Fig. 3.14a to present all

converter output voltages and the load output voltage before reaching the regulated level (i.e., more than 1.5V). The circle D is chosen for demonstration purpose and all scenarios before the regulated level are identical. The currents at the inputs of converters are shown in Fig. 3.15. All converters actively draw currents from their connected energy sources; therefore, all energy sources contribute to the load or the battery. As shown, the proposed energy combiner is designed for a better efficiency that includes all energy sources in the energy harvesting process.

3.4 Conclusion

Microbial fuel cells (MFCs) designed with the same material and physical size generate different voltages at their outputs. The discrepancy at MFC outputs can be explained by the nonlinear effects of microorganisms. An integrated power converter that includes a start-up circuit, a signal generator, and an output regulation circuit for low-voltage microbial energy harvesting was designed to up-convert the voltage to the desired level (e.g. 1.5V). Conventional energy combiner circuits lead to the efficiency degradation and exclude some energy source contributions. To overcome these issues, this work presents an efficient energy combiner circuit for multiple microbial energy harvesting sources. The combiner circuit is based on an in-order connection and has equal time of the connection. The stored energy at the converter outputs is fully transferred without loss of energy by routing the outputs to the load or an energy storage (e.g., a rechargeable battery or a super capacitor). Results demonstrate the effectiveness of the proposed energy combiner circuit.

Chapter 4

Multianode SMFC Energy Harvesting Interface Circuit

Numerous factors affecting the proper function and stable power generation in MFCs have been identified, and one with great significance is underwater bio-stress, referred to as bioturbation [1]. The anodes in marine sediment MFCs are buried in the sediment and operated under an anaerobic condition isolated from oxygen. However, anaerobic media can be easily damaged by either marine organisms burrowing through the sediment [2] or incomplete anode burial and insertion [18, 64], causing dissolved oxygen in water to penetrate into the anaerobic medium and reach anode surface, as shown in Fig. 4.1. Subsequently, the generated electrons at the anode surface by microorganisms are depleted by oxygen, which eliminates the net electric potential difference across MFC electrodes. These so-called reverse reactions, i.e. electrochemical redox reactions at the anode, cause an equivalent short-circuit effect, and thus the affected MFC cannot produce any useful voltage or power output.

To ensure the stability of MFCs, the bio-stress related issues must be resolved. Several solutions have been presented in the literature. One technique employs small anodes [18, 64], which can be easily buried and deployed in the underwater environment, to lower the failure rate against bioturbation. However, stable power generation is still at risk when a single

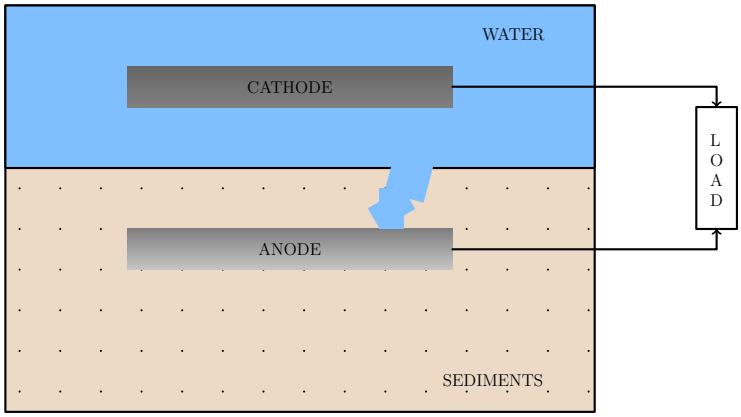

Figure 4.1: The structure for bioturbation in BMFC.

MFC system is deployed in the harsh marine environment. Our group also proposed a multi-anode technique [1] that spatially distributes multiple anodes associated with a shared cathode, as shown in Fig. 4.2. When one or several anodes are impaired by the burrowing organisms, the induced problem will only localize to those anodes without affecting other anodes. The functional anodes still maintain sufficient electric potential difference with the shared cathode, allowing MFCs to generate a stable power output. Therefore, MFCs are robust in the presence of diverse bioturbation problems.

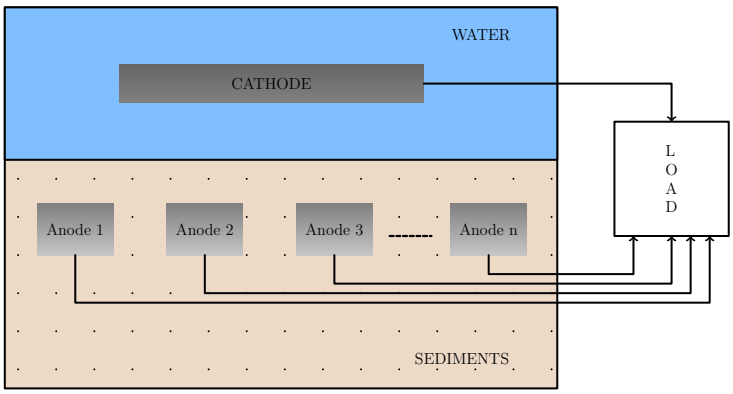

Figure 4.2: The structure of the developed multi-anode BMFC in [1].

Employing multiple anodes for bioturbation resilience imposes new requirements on the design of power management systems (PMS). Specifically, the PMS must be able to detect the

impaired anodes automatically and disconnect them from the rest of the BMFC; otherwise the reverse reactions at the impaired anodes will cause an equivalent short-circuit effect to other anode/cathode pairs as well. In addition, the PMS should boost the output voltage to a level required by the load. The load will be operated in the burst mode; it requires a certain charging time to accumulate energy into an energy storage element so that the load can work for a short period, and this scenario will be repeated over the time. These new requirements are truly challenging due to the fact that BMFCs typically generate very small output power (e.g., less than $1w/m^2$ of electrode area in filed tests), which also requires the overhead of the PMS to be as small as possible. Previous works [15], [28], [16], [30], [31], [11],[33], [13], [37] have studied several PMS for single-anode BMFCs. In [64], a PMS was developed for multiple independently operated SMFCs (mio-SMFC) to improve the robustness against failures in individual SMFC (e.g., when the anode of an SMFC is not totally covered by the sediment). These PMS are in general not suitable for multi-anode BMFCs [1].

In this chapter, the design of a power management system (PMS) for multianode SMFCs is presented. The PMS is based on discrete components which provides the best efficiency of 35.02% with three number of anodes.

4.1 Discrete Power Management System

An effective discrete PMS design for achieving bioturbation resilience in multi-anode BMFCs [1], which have a different structure than the multiple independently operated SMFCs [64] are presented in this chapter. The proposed PMS consists of a multi-anode decoupling circuit, a super capacitor, a self-sustained (i.e., not requiring other power sources) switching circuit, and a DC-DC converter (i.e. boost converter). The multi-anode decoupling circuit is a key component in this PMS. It can automatically detect and disconnect the impaired anodes caused by bioturbation, so that the BMFC can reliably harvest energy even if the anaerobic condition at some anodes is broken by aquatic organisms, i.e., seeped oxygen

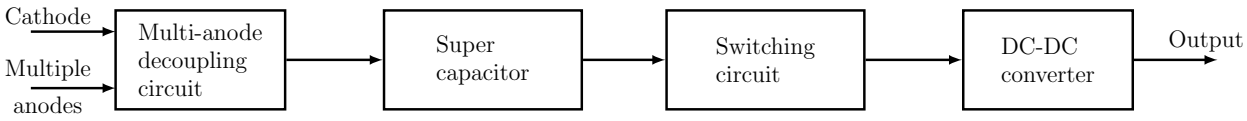

Figure 4.3: The system diagram of the proposed discrete PMS.

resulting in electron depletion at the corresponding anodes. The super capacitor is used to temporarily accumulate the harvested energy and then deliver it to the DC-DC converter, which steps up the output voltage for the load. The self-sustained switching circuit provides an interface between the super capacitor and the DC-DC converter. This circuit controls the energy accumulation and delivery processes. Different from most existing PMS for BMFCs, the proposed PMS is self-starting, i.e., no need of extra power sources other than the BMFC. The preliminary idea of this PMS was discussed in [10], [2].

4.2 Proposed Discrete Power Management System for Multi-anode BMFCs

The system diagram of the proposed discrete PMS is shown in Fig. 4.3. It consists of a multi-anode decoupling circuit, a super capacitor, a switching circuit, and a DC-DC converter. The function of the multi-anode decoupling circuit is to remove the effect of impaired anodes so as to improve the robustness of the BMFC under bioturbation. The switching circuit controls the charging-discharging cycles of the super capacitor, which acts as a temporary storage to accumulate the energy harvested from the BMFC. The DC-DC converter generates the required output voltage to the load. Detailed design and operation of these components will be discussed in the following sections.

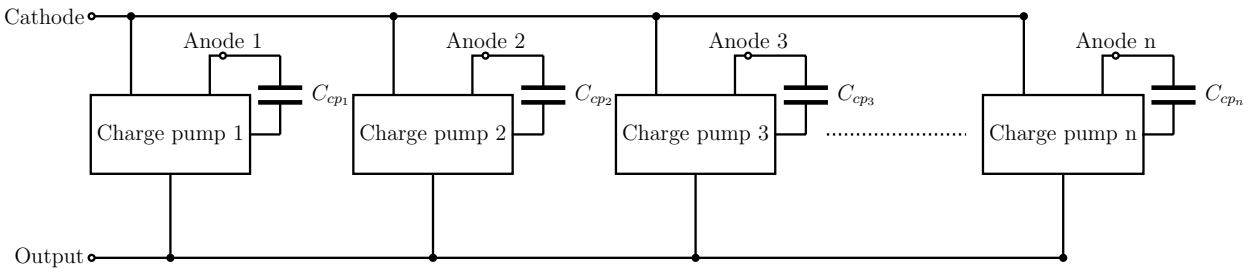

Figure 4.4: Multi-anode decoupling circuit. A shared cathode is used as the positive input for all charge pumps while each charge pump uses one anode as its own ground. Each charge pump has a local capacitor (C_{cpi}).

4.2.1 Multi-anode decoupling circuit

Bioturbation problems cause an equivalent short-circuit effect at the affected anodes. This is because the seeped oxygen causes reverse reactions that consume the harvested electrons at the anode surface, i.e., the electrons will not be transported to the cathode and consumed by the external load. The decoupling circuit is able to detect this problem automatically and disconnect the affected anodes from the rest of the BMFC. As shown in Fig. 4.4, the decoupling circuit consists of a group of charge pumps, the number of which equals that of the anodes in the BMFC. These charge pumps use the shared cathode as their positive inputs. Each charge pump takes one anode as its negative input (i.e., serves as the ground reference). The outputs of the charge pumps are connected to the super capacitor, which is used as the storage element to accumulate the harvested energy from the BMFC.

Assume that one anode is impaired by bioturbation (e.g., seeped oxygen). Due to reverse reactions, the electric potential of this anode will drop and approach the potential of the shared cathode, e.g., this anode is turning into a cathode. Thus, the charge pump taking this anode and the shared cathode as the negative and positive input, respectively, does not have enough input voltage to start up. Other anodes will not be shorted because these anodes are connected to the negative inputs of different charge pumps. The shared cathode will not be affected either because bioturbation only occurs on anodes; nor will the shared output be affected because the impaired anode effectively disables the corresponding charge

pump (as there is not enough input voltage to start up this charge pump), i.e., the output of a disabled charge pump cannot be shorted by its inputs because of the internal isolation circuitry in the charge pump [65]. This is also the case if more than one anodes are impaired, where the corresponding charge pumps are also disabled. Note that other unaffected charge pumps are still functioning because their anodes are decoupled from the impaired anodes.

Note that each charge pump will need a local capacitor to first accumulate the energy harvested from the corresponding anode. Once the local capacitor reaches or exceeds the discharge start voltage, the positive end of the local capacitor will be connected to that of the super capacitor by a switch circuit inside the charge pump. The negative ends of the local capacitor and the super capacitor (using an anode as the ground reference) are not physically connected but have similar electric field potential, i.e., they share the same electrical ground. This is because microbes are able to maintain the redox gradients in the sediment and establish a stable electric field potential at the anodes [1], [66], [67]. Thus, the harvested energy by the other anodes will be transferred from their local capacitors to the super capacitor.

A question arises that, instead of using individual local capacitor for each charge pump, whether it is possible to use only one local capacitor shared by all charge pumps. The answer is no due to two reasons. First, since anodes may be surrounded by different sediment conditions, the charge pumps will have different charging and discharging cycles. It is impossible to synchronize these operations for a single local capacitor. Second, these charge pumps are also used to detect bioturbation problems on the anodes. If one or several anodes are impaired, the corresponding local capacitors will have no or very small voltage. Thus, the total output voltage of the decoupling circuit will be reduced if all local capacitors are replaced by a shared local capacitor.

The value of the local capacitors affects the time of transferring the stored energy to the load, which is critical to the BMFC that may have impaired anodes. In other words, if one or some anodes are impaired, the energy stored in their local capacitors is no longer

retrievable because these capacitors may not reach the discharge start voltage required by the charge pumps. In order to determine the optimal value of the local capacitors, the power transfer efficiency of the charge pumps should be considered. This efficiency is defined as the ratio between the input power P_{in} of a charge pump and the received power P_c at its local capacitor, as

$$\eta = P_c/P_{in}. \tag{4.1}$$

The charge pump input power P_{in} can be calculated as

$$P_{in} = V_{in} \times I_{in}, \tag{4.2}$$

where V_{in} and I_{in} are the average input voltage and current (drawn from the BMFC), respectively, of the charge pump.

On the other hand, the charge pump starts to discharge the local capacitor to the super capacitor once its local capacitor voltage reaches the discharge start voltage V_d, and the discharging process stops when the local capacitor voltage reduces to V_c, at which point the local capacitor starts to charge up again by the BMFC. Thus, the energy delivered to the local capacitor can be expressed as

$$E = 1/2 \times C \times (V_d^2 - V_c^2), \tag{4.3}$$

where C is the value of the local capacitor. The average power P_c delivered to the local capacitor can be obtained as

$$P_c = (1/2t) \times C \times (V_d^2 - V_c^2), \tag{4.4}$$

where t is the time for the local capacitor to charge from V_c to V_d. In this study, V_d and V_c are $2V$ and $1.44V$, respectively, while the charging time t increases nonlinearly with C (the

underlying effect will not be cancelled out by C/t). Thus, if a large local capacitor is used, it will increase the take a long time to charge this capacitor, which will reduce the charge pump output power P_c as well as the power transfer efficiency η.

In this study, different local capacitors are tested and the corresponding power transfer efficiencies are measured to determine the optimal capacitor value that maximizes η, as discussed in section 4.3.2.

4.2.2 Super capacitor and switching circuit

As mentioned, the charge pumps in the decoupling circuit cannot be synchronized on their charging and discharging cycles, which are determined by the sediment conditions around the anodes. When a charge pump's local capacitor reaches the discharge start voltage, the stored energy is released through the output of the charge pump. Because the discharging times of these charge pumps are different, the outputs of the charge pumps cannot drive the DC-DC converter or the load directly. Doing so will significantly reduce the efficiency of the PMS.

The best solution to this problem is to incorporate a super capacitor, which acts as the second stage storage to accumulate the energy when any of the charge pumps start to discharge. Note that the outputs of non-functional charge pumps (e.g., those connected to the impaired anodes) are high-impedance and thus will not affect the operation of the super capacitor. Due to the buffering effect of the super capacitor, a relatively stable energy level is available for the subsequent circuits.

The connection between the super capacitor and the DC-DC converter needs to be controlled by a switching circuit. If no switching circuit exists, the DC-DC converter will constantly draw current from the super capacitor. Due to the low output power of BMFCs, the super capacitor voltage will drop quickly and won't come back again to the required level of the DC-DC converter. Thus, the DC-DC converter is not able to start up and drive

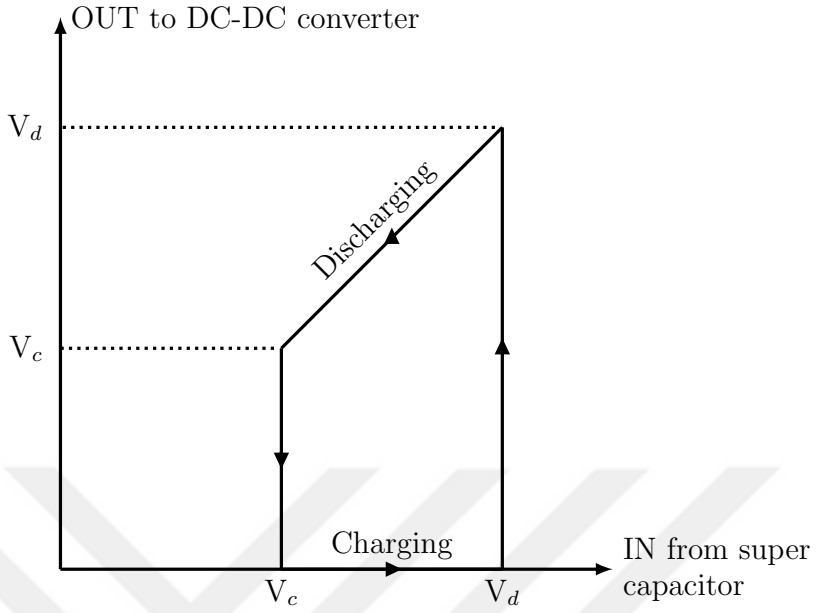

Figure 4.5: The characteristic curve of the switching circuit. During the charging process, the switch is off, while during the discharging process, the switch is on.

the load. As shown in Fig. 4.5, the desired operation of the switching circuit should be as follows.

1. Initially, the super capacitor starts to charge from 0. The switching circuit is off, and the support capacitor and the DC-DC converter are disconnected. The input voltage of the DC-DC converter is zero during this period. No power is delivered to the load.

2. When the super capacitor reaches the discharge start voltage V_d, the switching circuit turns on and connects the super capacitor to the DC-DC converter. The input voltage of the DC-DC converter is equal to the voltage of the super capacitor. The super capacitor starts to transfer the stored energy to the DC-DC converter, which then provides the power to the load with the required voltage level.

3. Due to the low power output of BMFCs, the DC-DC converter draws energy from the super capacitor at a faster rate than the super capacitor draws energy from the charge pumps. Thus, the voltage of the super capacitor starts to reduce immediately after

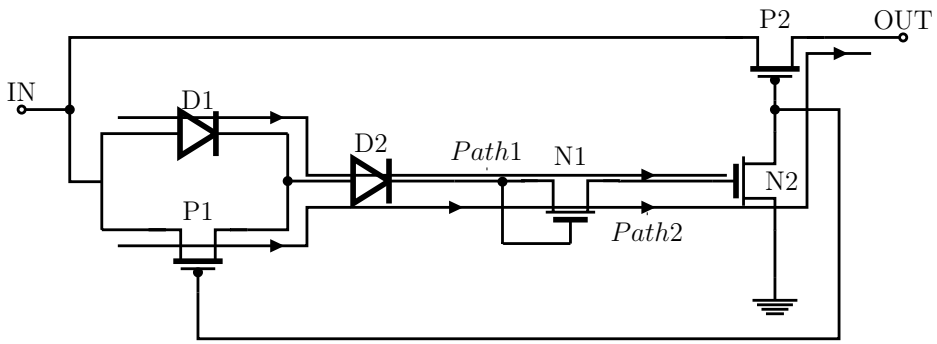

Figure 4.6: Schematic of the switching circuit.

it is connected to the DC-DC converter by the switching circuit. When the voltage drops to the charge start voltage V_c, the switching circuit turns off, disconnecting the super capacitor from the DC-DC converter. The input voltage of the DC-DC converter becomes zero and the load receives no power.

4. The super capacitor starts to charge back from V_c to V_d by the BMFC through the charge pumps, and the operation returns to step 2.

Note that the above operations can be implemented in different ways. For example, a hysteresis controller [11], [33] could be utilized, but an extra power supply is needed to power the comparator and build reference voltages. Using extra power supplies to enable power management functions is undesirable as it compromises the goal for self-sustainability. Ideally, the entire system, including the PMS and the load, should be powered by the BMFC only.

In this study, we develop a new switching circuit that is self-starting; i.e., it does not require any extra power sources other than the energy harvested by the BMFC. Figure 4.6 shows the schematic of the proposed switching circuit. As the super capacitor initially charges up, the pMOS transistor $P1$ is cut off. The voltage of the super capacitor goes through $Path1$ across the diodes $D1$ and $D2$ and nMOS transistor $N1$. The gate voltage

V_{g2} of the nMOS transistor $N2$ can be expressed as

$$V_{g2} = V_{CAP} - 2 \times V_D - V_{tn1}, \tag{4.5}$$

where V_{CAP} is the voltage of the super capacitor that is being charged up, V_D is voltage drop over the diode, and V_{tn1} is the threshold voltage of the nMOS transistor $N1$.

Once V_{g2} increases above the threshold voltage V_{tn2} of $N2$, $N2$ becomes conducting and the gate voltages of the pMOS transistors $P1$ and $P2$ drop to zero. Consequently, $P1$ and $P2$ turn on and the DC-DC converter is connected to the super capacitor through $P2$. The super capacitor starts to discharge and transfer the stored energy to the DC-DC converter. Substituting $V_{g2} = V_{tn2}$ into (4.5), the super capacitor's discharge start voltage V_d can be expressed as

$$V_d = V_{tn1} + V_{tn2} + 2 \times V_D. \tag{4.6}$$

As diode $D1$ is bypassed by $P1$ on $Path2$, and the gate voltage V_{g2} of $N2$ initially undergoes a sudden increase with the amount equal to the voltage drop of $D1$, i.e.,

$$V_{g2} = V_{CAP} - V_D - V_{tn1}. \tag{4.7}$$

This increase will keep $N2$ on untill the voltage of the super capacitor V_{CAP} drops to the charge start voltage V_c. From (4.7), as the voltage of the super capacitor V_{CAP} drops, V_{g2} reduces as well. Once V_{g2} reaches the threshold voltage V_{tn2} of $N2$, $N2$ is cut off, which also turns off $P1$ and $P2$ and thus disconnects the DC-DC converter from the super capacitor. The super capacitor will be charged again. Thus, substituting $V_{g2} = V_{tn2}$ into (4.7), the charge start voltage V_c can be expressed as

$$V_c = V_{tn1} + V_{tn2} + V_D. \tag{4.8}$$

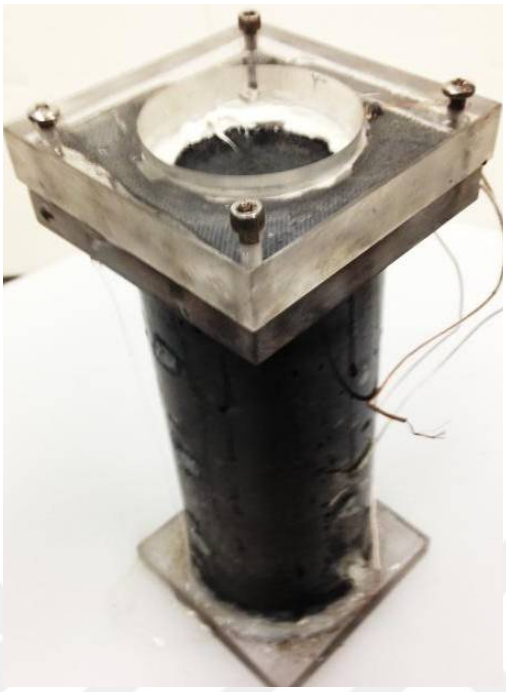

Figure 4.7: The prototype BMFC with four anodes and one shared cathode.

Obviously, the above operations are controlled by the output voltage of the super capacitor only, i.e., the proposed switching circuit is self-starting (no need of extra power sources). In addition, the charge pumps and the DC-DC converter are also self-starting, making the proposed PMS highly efficient and self-sustainable.

4.3 Implementation

The proposed PMS was implemented in a printed circuit board (PCB) and tested through a prototype BMFC. The BMFC has four anodes and one shared cathode to deal with the bioturbation problems.

4.3.1 Multi-anode BMFC

A multi-anode BMFC made from plexiglas cylinders (effective working volume: 500 mL, inner diameter: 7.5 cm, and length: 15 cm) was used to test the performance of the proposed PMS.

The BMFC implementation is shown in Fig. 4.7. Four carbon cloth anodes are placed inside the plexiglas cylinder and buried in the sediment to support the growth of microorganisms and collect the generated electrons. Each of the installed anodes is separated by 2 cm in distance. Three anodes are used for energy harvesting and one anode serves as the ground reference for the super capacitor, switching circuit, DC-DC converter and the load. Activated carbon cathode (ACC) (diameter: 5 cm) and 20% Polytetrafluoroethylene (PTFE) is secured onto the plexiglas cylinder and immersed in water to utilize the dissolved oxygen as the electron acceptor. The cathode is positioned parallel to the benthic surface at a distance of 4 cm. The water depth above the cathode is 12 cm. Organic soil sediments with diverse microbes are utilized as the inocula. Sodium acetate is added as an additional carbon source to enhance the inoculation of anaerobic electrogenic bacteria. All measurements were conducted in duplicates and operated at room temperature of 20°C.

4.3.2 PMS Implementation

The charge pumps for the BMFC need to work with a low input voltage and draw small current from the BMFC. The charge pump S-882 from Seiko Instruments [65] was selected. It requires an input voltage as low as $0.3V$ and can charge to $2V$ and discharge to $1.44V$. The decoupling circuit uses three charge pumps, each connected to one anode.

Each S-882 charge pump requires an external local capacitor C_{cp}, whose value must be large enough to support the charge sharing between the charge pump and the super capacitor/DC-DC converter when the switching circuit is on. In addition to this requirement, the selection of the local capacitor C_{cp} also affects the power transfer efficiency η, as discuss in section 4.2.1. To obtain the optimal power transfer efficiency, different values of C_{cp} were tested, and the input and output power of the charge pump was measured to calculate the efficiency. Table 4.1 shows the results of charging time and power transfer ratio η (measured from one charge pump) under different values of C_{cp}. The charging time refers to the time

Table 4.1: Charging time and power transfer ratio for different charge pump local capacitors.

Capacitor $C_{cp}(\mu\text{F})$	Charging Time (s)	Power Ratio η (%)
470	32	31
800	53	31.04
1270	80	31.08
1740	112	29.81
2210	142	29.09

when the capacitor voltage increases from $1.44V$ to $2V$.

From Table 4.1, it can be seen that using a larger charge pump capacitor results in a longer charging time. Moreover, the power transfer efficiency also changes, initially increasing and then decreasing. This is because power transfer is a complicated process determined by the electric operating mode of the charge pump, which in this case varies with the size of the local capacitor C_{cp}. The largest value of power transfer efficiency is achieved when $C_{cp} = 1270\mu\text{F}$. As the value of C_{cp} increases, the effect of increase in charging time will dominate and reduce the power transfer efficiency. If one or more anodes fail to operate due to bioturbation or other problems, the stored energy in the corresponding C_{cp} will be unaccessible because the capacitor cannot reach the required voltage level to discharge the charge pump. The stored energy will then be trapped in the capacitor. This problem can be mitigated by using a smaller charge pump capacitor to reduce the charging time. As the charging time is reduced, the amount of wasted energy, if any, will be relatively small. In this design, we choose $C_{cp} = 470\mu\text{F}$ because of the short charging time. Also, the degradation in power transfer efficiency is negligible. Using a smaller charge pump capacitor reduces the charging time of the charge pump, which minimizes the impact of bioturbation on anodes.

The selection of the super capacitor needs to consider the requirement of specific applications (e.g., the power requirement of loads). For the purpose of demonstration, we use a 220mF super capacitor with the discharge start voltage $V_d = 1.44V$ and the charge start voltage $V_c = 1.12V$. The reason of choosing $V_d = 1.44V$ is that this value is the maximum

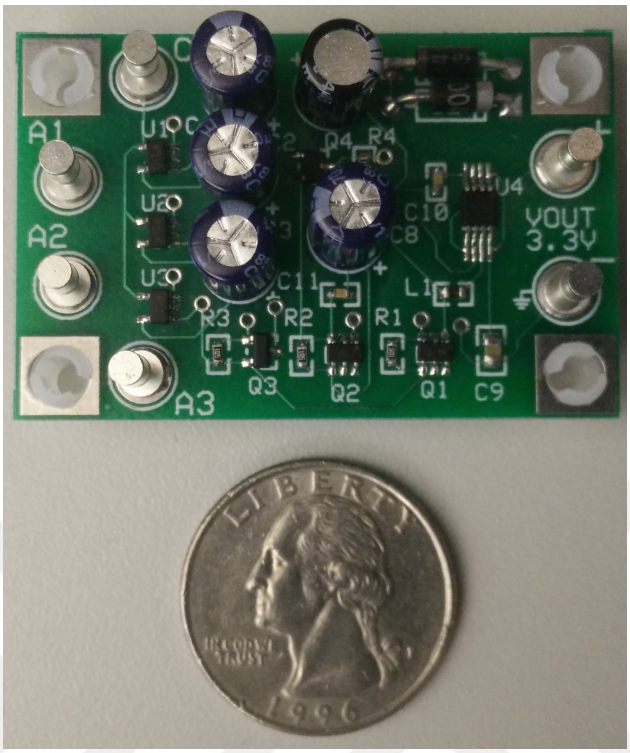

Figure 4.8: The PCB implementation of the PMS.

voltage allowed by the super capacitor. On the other hand, choosing $V_c = 1.12V$ enables the DC-DC converter (here we choose L6920DB from ST microelectronics [68]) to achieve a higher efficiency than the specified minimum input voltage of $0.8V$.

The switching circuit needs to be operated with these voltages; i.e., the switch will be on to discharge the super capacitor when the super capacitor voltage reaches $V_d = 1.44V$, and when the super capacitor voltage drops to $V_c = 1.12V$, the switch will be off so that the super capacitor can be recharged by the BMFC. In Fig. 4.6, the diodes $D1$ and $D2$ are 1N4001 and 1N4004 (Vishay Siliconix, $V_D = 320mV$), respectively, $P1$ is FDN304P (Fairchild semiconductor, $V_{tp1} = -0.4V$), $P2$ is Si3499DV (Vishay Siliconix, $V_{tp2} = -0.75V$), $N1$ is PMV31XN (NXP semiconductors, $V_{tn1} = 0.35V$)), and $N2$ is Si3460BDV (Vishay Siliconix, $V_{tn2} = 0.45V$). Thus, $V_d = 1.44V$ and $V_c = 1.12V$ from (4.6) and (4.8) in section 4.2.2, which meet the design specifications. Note that the charge start voltage V_c and the discharge start voltage V_d can be adjusted by applying different types of diodes or adding more diodes

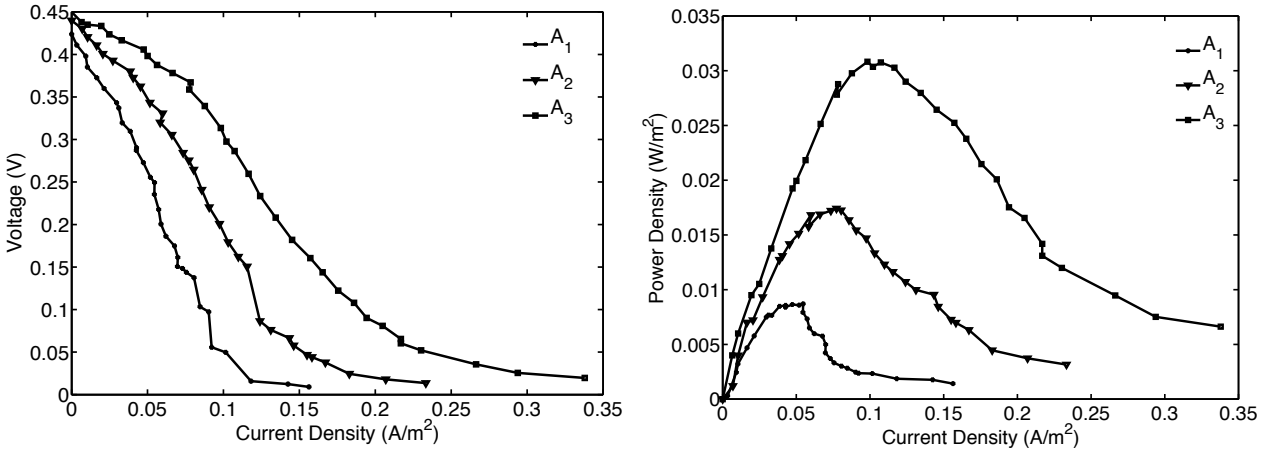

(a) Polarization curve (voltage vs current density) (b) Power density vs current density

Figure 4.9: Voltage-current density and power density-current density characteristics of the prototype BMFC.

to the switching circuit.

The fabricated PCB of the PMS is shown in Fig 4.8.

4.4 Experimental Results and Discussion

This section presents the experimental results from the proposed PMS and the BMFC. The power-current density characteristics of the BMFC were tested as follows. First, the BMFC was connected to a resistive load until it reached the steady state. After that, the load was disconnected to measure the BMFC open circuit voltage (OCV), which was around $0.45V$ in this study. Then, a variable resistive load (R_{ext}) from 15Ω to 2500Ω was connected to the BMFC in order to construct the polarization curves for three different anode configurations: a three-anode case (A_3) where all anodes are functional without any bioturbation, a two-anode case (A_2) where one anode is impaired by exposing to the dissolved oxygen in water, and a one-anode case (A_1) where two anodes are impaired for the same reason. For each R_{ext} value, the BMFC output voltage and current values were recorded. The measurements were made when the voltage and the current become stable. In Fig. 4.9a, the current density

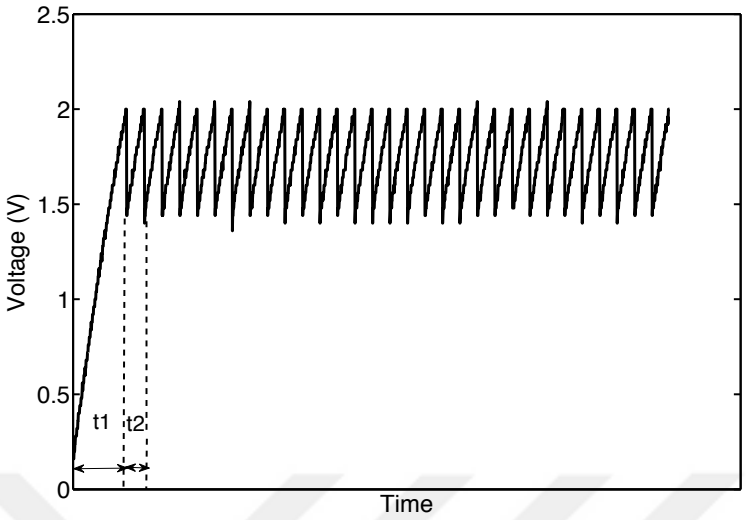

Figure 4.10: Measured waveform of charge pump capacitor voltage. The values of time axis (e.g., t_1 and t_2) are different for different cases, as shown in Table 4.2.

(normalized by the cathode area) and voltage are proportional to the number of functional anodes under the same R_{ext} value. This is because these results are obtained under the different numbers of anodes, i.e., the BMFC has different configurations. The power density was calculated as a product of the measured voltage and current. In Fig. 4.9b, it can be seen that the power and current densities increase with the number of functional anodes in the BMFC. These results verify that the multi-anode BMFC works as expected in the presence of bioturbation.

To test the PMS, the BMFC was connected as the input and a 10kΩ load resistor was connected as the output. Charge pumps were monitored to evaluate the local capacitor charging and discharging cycles for each case, as shown in Fig. 4.10, where t_1 measures the time when the charge pump starts to charge its local capacitor from 0 to $2V$, and t_2 is the time that the charge pump charges its local capacitor from the charge start voltage (V_c) to the discharge start voltage (V_d). The values of V_c and V_d are $1.44V$ and $2V$, respectively. For A_3, A_2 and A_1 cases, the local capacitors have the same V_c and V_d but different t_1 and t_2 values, as the number of functional anodes is different and each anode may see different sediment conditions. These results are summarized in Table 4.2, where for A_3 and A_2 cases,

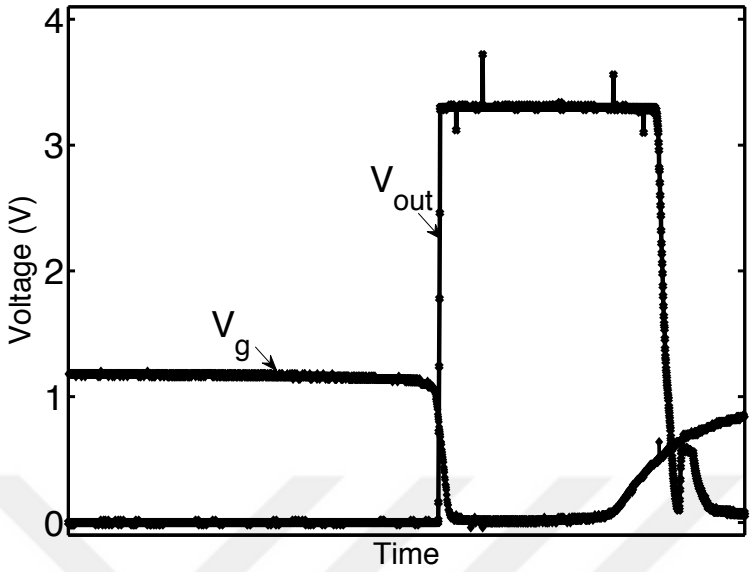

Figure 4.11: Measured waveforms of DC-DC converter output voltage (V_{out}) and the gate voltage (V_g) of PMOS $P2$ in the switching circuit. The value of time axis are different for different cases, as shown in Table 4.2.

the values of t_1 and t_2 are averaged over all the functional anodes.

To verify the function of the switching circuit, Figure 4.11 shows the relationship between the DC-DC converter output voltage and the gate voltage V_g of the PMOS $P2$ in Fig. 4.6, which controls the on/off behavior of the switching circuit. It can be seen that when the super capacitor voltage reaches the discharge start voltage, V_g starts to decrease and quickly drops to zero (as NMOS $N2$ is on). Thus, $P2$ switches on and the super capacitor starts to discharge. The stored energy at the super capacitor is transferred to the DC-DC converter, which generates a stable $3.3V$ output voltage to drive the load. When the super capacitor is discharged to the charge start voltage, $P2$ switches off and V_g starts to increase. The DC-DC converter output voltage drops to zero as the switching circuit is off. The same process repeats over the time. These results indicate that the switching circuit works properly and the expected control on energy transfer is accomplished.

The super capacitor voltage and the output voltage to the load were measured in Fig. 4.12a, and Fig. 4.12b shows the zoomed area between $t3$ and $t5$. For A_3, A_2 and A_1 cases, the charge and discharge start voltages of the super capacitor are $V_c = 1.12V$ and $V_d = 1.44V$, respec-

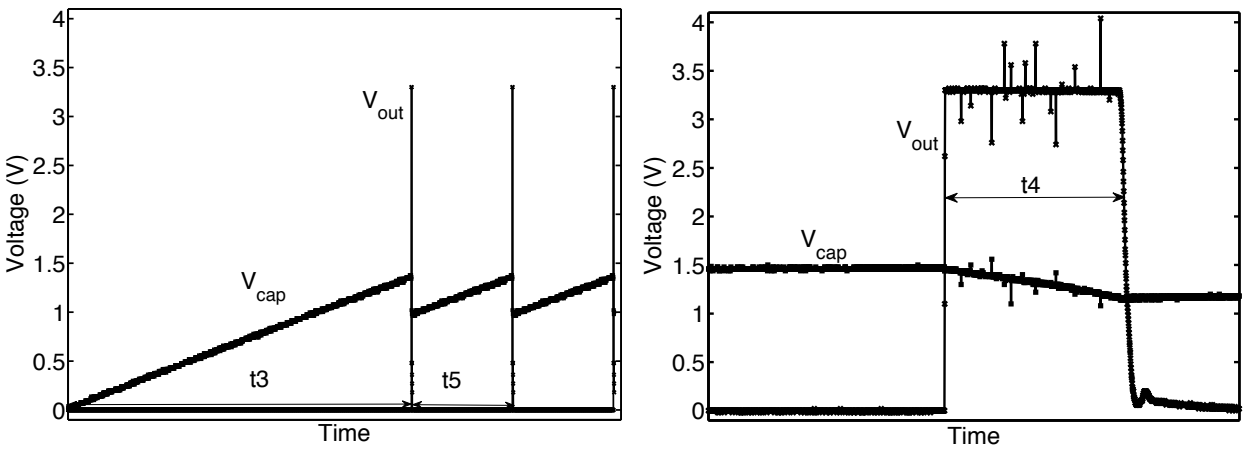

Figure 4.12: (a) Measured waveforms of the super capacitor voltage (V_{cap}) and the output voltage to the load (V_{out}). (b) Zoomed waveforms when the load is active (e.g., between $t3$ and $t5$ in (a)). The values of time axis (e.g., t_3, t_4, t_5) are different for different cases, as shown in Table 4.2.

tively. The output voltage to the load is $V_{out} = 3.3V$. It can be seen that when the super capacitor voltage reaches the discharge start voltage $V_d = 1.44V$, the switching circuit is on and the load receives the power from the DC-DC converter. The super capacitor voltage then reduces and once it reaches $V_c = 1.12V$, the switching circuit is off. No power is delivered to the load and the super capacitor is charged back by the BMFC through the charge pumps. Due to the low power output of the BMFC (see Fig. 4.9b), the load will operate in this burst mode. It requires a sufficiently long charging time t_5 to accumulate the harvested energy into the super capacitor so that the load can consume the energy and work for a short period of t_4. This pattern will be repeated over the time. Note that A_3, A_2 and A_1 cases have different values of t_3 (initial charging time) and t_5, as shown in Table 4.2. Increasing the number of anodes in the BMFC can reduce both t_3 and t_5. This is because multi-anode BMFCs can harvest more energy to the load. On the other hand, the load active time t_4 is the same as the value of the super capacitor is fixed, i.e., the same amount of energy stored in the super capacitor is transferred to the load.

Finally, the power transfer efficiencies of A_3, A_2 and A_1 cases were measured. The overall

Table 4.2: Measured time results for A_3, A_2 and A_1 cases.

Cases	t_1	t_2	t_3	t_4	t_5
A_1	202s	60s	4.1h	25s	0.916h
A_2	189s	53s	2.06h	25s	0.48h
A_3	180s	55s	1.383h	25s	0.3h

efficiency of the system is expressed as

$$\eta_{overall} = \eta_1 * \eta_2, \tag{4.9}$$

where η_2 is the efficiency of the DC-DC converter, and η_1 is the efficiency from the BMFC to the super capacitor, obtained as

$$\eta_1 = P_{cc}/P_{in}, \tag{4.10}$$

where P_{in} is the charge pump input power (i.e., BMFC output power) and P_{cc} is the power transferred to the super capacitor, defined as

$$P_{cc} = (1/2t_5) \times C \times (V_d^2 - V_c^2), \tag{4.11}$$

where C is the value of the super capacitor.

As an off-the-shelf charge pump (Seiko S-882) is used, its input impedance is fixed, which is larger than the BMFC internal impedance. As a result, the input power to the charge pump is smaller than the maximum output power of the BMFC. This affects the charging and discharging cycles of the charge pump, resulting in a long charging time, t_5. As the number of functional anodes increases, the charging time t_5 reduces and P_{cc} increases, which increases the overall efficiency. The overall power transfer efficiencies are 20.23%, 26.18% and 35.02% for A_1, A_2 and A_3, respectively. Note that most losses during power transfer come

from the overheads in the commercial charge pump, DC-DC converter and other components used in PMS, which are beyond our control.

Table 4.3 compares the existing works of power management systems for MFCs. In terms of efficiency, the proposed PMS is comparable to the previous work [64] that does not require the support of external power sources. Note that this work and [64] target different MFC structures and apply different approaches for power management. In summary, the proposed PMS is truly self-sustainable and can effectively address the bioturbation problem.

4.5 Conclusions

Multi-anode BMFCs have distinct advantages over the existing single-anode BMFCs. Using multiple anodes can improve the robustness of BMFCs in the harsh ocean environment. A discrete power management system (PMS) for multi-anode BMFCs was developed in this study. The PMS is self-starting and can automatically detect the impaired anodes due to bioturbation. Design optimization of the PMS includes the consideration of both the power transfer efficiency and the impact of possible bioturbation problems. The detailed design of the PMS was discussed and performance was tested with a prototype multi-anode BMFC. The experimental results match with the design specifications.

Table 4.3: Performance comparison of the existing PMS.

Circuit	[16]	[30]	[11]	[64]	This work
# of anode	single	single	single	multi	multi
# of cathode	single	single	single	multi	single
Required startup voltage	300mV	180mV	N/A	300mV	300mV
External power sources	Not required	Not required	Required for operation	Not required	Not required
Efficiency	22%	N/A	45%	32.8%	35.02
Bioturbation / Robutsness	No	No	No	Yes	Yes

Chapter 5

Energy Harvesting System for Bioturbation Resilince in Multianode SMFC

As discussed in the previous chapter, the energy harvesting circuit with a multi-anode MFC consists of a group of discrete charge pumps, a super capacitor, a switch circuit, and a boost converter [2], as shown in Fig. 5.1. At the first state, discrete charge pumps are connected in parallel and the number of which equals the anodes in the MFC. These charge pumps are used to automatically detect and remove the effect of impaired anodes in the presence of bioturbation so as to enhance the robustness of the MFC in the harsh marine environment.

However, there are some issues with the existing setup. Due to bioturbation at the anode, the corresponding charge pump does not operate while others are functional. Charges stored at the following super capacitor will leak through that charge pump into its output capacitor, thereby reducing the overall efficiency. In addition, each charge pump has its own output capacitor, introducing a large overhead. Moreover, discrete charge pumps are not well-suited for energy harvesting with MFCs. Due to their relatively large internal energy losses, the energy conversion efficiency is very low for MFCs. These issues introduce new requirements to the design of energy harvesting circuits for MFCs. Specifically, the following aspects should be considered:

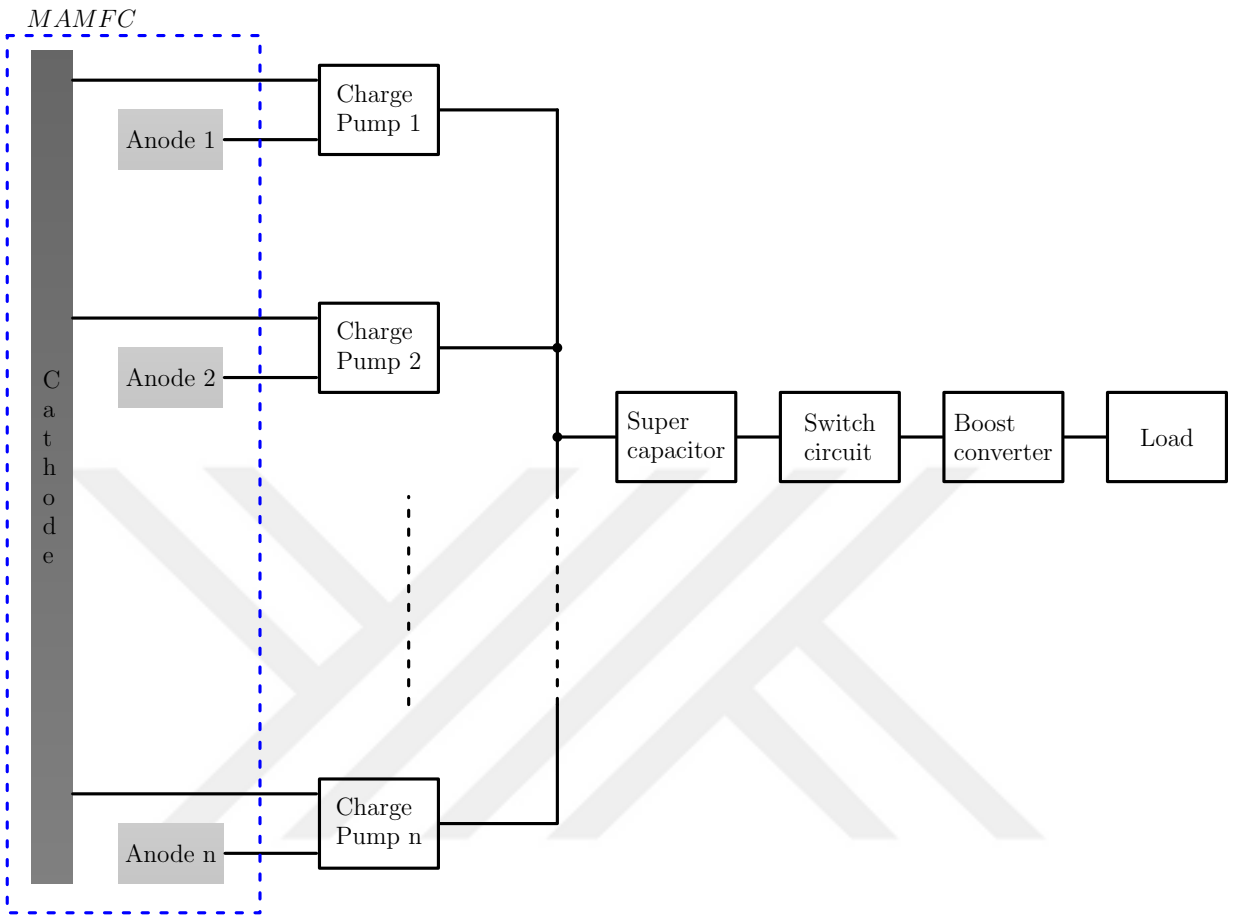

Figure 5.1: Energy harvesting with multi-anode MFC architecture [2]. For each anode, one separate charge pump is used. These charge pumps connected in parallel are referred to multi conventional charge pumps in this study.

1. The energy harvesting circuit should minimize the reverse leakage charge and the resulting efficiency degradation when one or several anodes are impaired by bioturbation.

2. The energy harvesting circuit should have small complexity to reduce its internal energy losses.

5.1 Proposed Energy Harvesting Integrated Circuit

In order to efficiently utilize the harvested energy from MFCs, an interface circuit is required between a MFC and its load (e.g., sensors, LED or other electronic devices). For energy

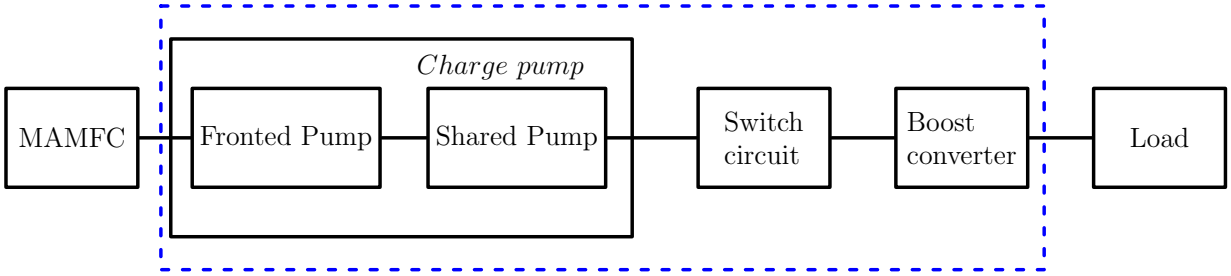

Figure 5.2: Overview of the multi-anode MFC energy harvesting system.

harvesting from a multi-anode MFC, several requirements must be met.

- First, the circuit must be compatible with the multi-anode MFC; i.e., impaired anodes in the MFC should be detected and disconnected automatically by the circuit.
- Second, due to the low output power of the MFC (typically in the range of 1μW to 2mW), the load has to be operated in a burst mode. It requires a certain charging time to accumulate the harvested energy into a temporary storage component (e.g., a super capacitor) so that the load can use the stored energy in a short time, and this process is repeated over time.
- Finally, the typical operating voltage for the load (e.g., at least $1.8V$ for many sensors) cannot be generated directly from the MFC, whose output voltage is typically in the range of $0.4 - 0.8V$. Therefore, the output voltage of the MFC should be boosted to a level that matches the load.

5.1.1 Circuit Organization

The overall design of the proposed integrated circuit for multi-anode MFC energy harvesting is shown in Fig. 5.2. At the top level, the circuit consists of a shared-stage charge pump, a switch control circuit, and a DC-DC converter. The shared-stage charge pump automatically decouples the impaired anodes caused by bioturbation from the rest of circuit. It contains two components, referred to as Frontend Pump and Shared Pump, respectively. Frontend

Pump includes multiple first-stage charge pumps connected in parallel (see Fig. 5.3), each connecting to an anode in the multi-anode MFC. Thus, the number of the first-stage charge pumps equals that of the anodes in the MFC. As explained later, Frontend Pump can automatically detect the impaired anodes due to bioturbation and disconnect the affected anodes from the system. On the other hand, Shared Pump in the subsequent stages includes normal charge pumps but are shared by all the anodes. A super capacitor (C_{cp}) is charged by the shared-stage charge pump. Energy harvested from the MFC is temporarily stored in C_{cp}. In order to provide a constant voltage to the load at the required level, a DC-DC converter is used to drive the load. To prevent inefficient use of the accumulated energy, a switch control circuit is implemented between the storage capacitor C_{cp} and the DC-DC converter. The energy transfer to the load is periodically activated by the switch control circuit. The detailed design of these components will be discussed in the following sections.

5.1.2 Shared-stage Charge Pump

Charge pumps are a key component in energy harvesting systems [38, 39, 41, 45, 69–71], e.g., as primary converters or controlling the switch of DC-DC converters because they can operate under low voltage and require low input voltage. However, existing charge pump circuits cannot be applied to multi-anode MFCs as they do not have the capability to detect impaired anodes. Employing multiple anodes for eliminating the effect of bioturbation in MFCs introduces a new requirement to the design of charge pumps. To meet this requirement, we propose a shared-stage charge pump that has two parts: Frontend Pump and Shared Pump.

5.1.2.1 Frontend Pump

Figure 5.3 shows the block diagram of Frontend Pump in the shared-stage charge pump and its circuit implementation. Frontend Pump consists of a number of first-stage charge pump

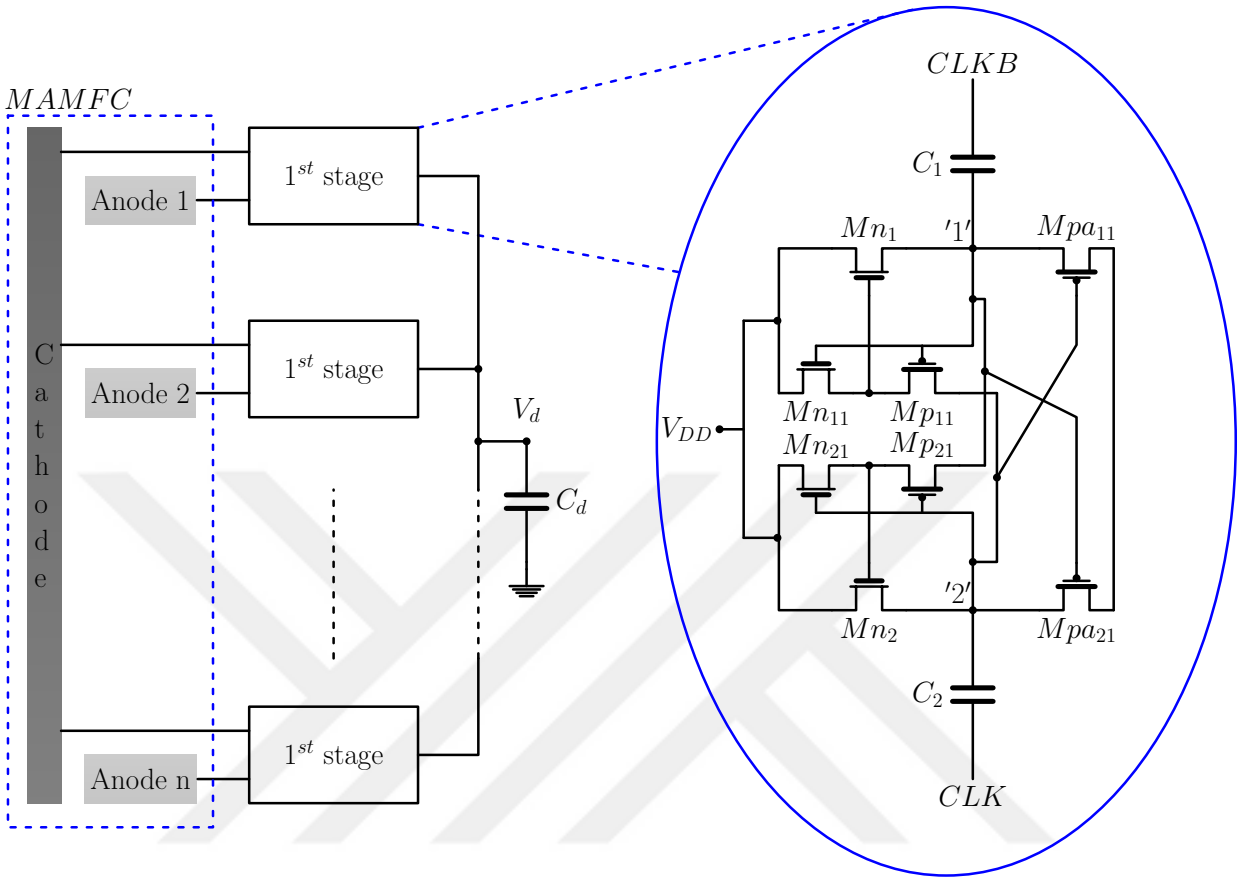

Figure 5.3: Block diagram of the fronted pump of core charge pump and its circuit implementation. V_n represents cathode(positive)/anode(negative) as an input

units connected in parallel, the number of which equals that of the anodes in the MFC. These units use the common cathode as their positive inputs, and each unit takes one anode as its negative input. The outputs of the units are connected to a capacitor C_d, which is used to provide power to the Shared Pump. Note that the connections of the common cathode and multiple anodes are not illustrated in the inset of Fig. 5.3; instead, input V_{DD} whose positive node is the shared cathode and negative node is each anode is shown.

Transistor on/off states and capacitor voltage of a first-stage charge pump unit is summarized in Table 5.1. It can be seen from Fig. 5.3 that, due to the same output (V_d) connection point of transistors $M_{pa_{11}}$ and $M_{pa_{21}}$, the output waveforms are complemental to each other. Thus, the same amount of voltage (roughly $2 \times V_{DD}$) is delivered to the output

at each $CLK/CLKB$ cycle. As a result, a low ripple output voltage is obtained.

Table 5.1: A summary of first stage operation and node voltages.

CLK &CLKB status	Transistor turns ON	Capacitor voltage
CLK=high	M_{n_1}, $M_{p_{11}}$	C_1=V_{DD}
CLKB=low	$M_{pa_{21}}$, M_{n21}	C_2=2V_{DD}
CLKB=high	M_{n_2},$M_{p_{21}}$	C_1=2V_{DD}
CLK=low	$M_{pa_{11}}$, M_{n11}	C_2=V_{DD}

Assume that one anode is impaired by bioturbation. The electric potential of the anode will drop and close to the potential of the shared cathode due to the reverse reaction. Therefore, the corresponding first-stage charge pump unit connected to that anode is short-circuited; i.e., it does not have enough input voltage to start up, and its output will stay in the high impedance stage. Since other anodes are decoupled from the impaired anode, other units are still operating. In other words, the short-circuit effect at the impaired anode will not propagate to other anodes. This is also the case if more anodes are impaired, where the corresponding units have high impedance outputs as well.

5.1.2.2 Shared Pump

Figure 5.4 shows the circuit diagram of Shared Pump. A number of charge pump units are connected in series, shared by all anodes, where the corresponding first-stage units have their outputs merged at the same point (V_d shown in Fig. 5.3). This common point is taken as the input voltage for the Shared Pump. The operation of the N^{th} stage in the Shared Pump is summarized in Table 5.2. Other stages have similar operations. The output stage of the Shared Pump includes two PMOS transistors, M_{p1} and M_{p2}, whose gates are controlled by the last stage in the Shared Pump.

The output voltage of the Shared Pump with $n-1$ stages can be approximated by

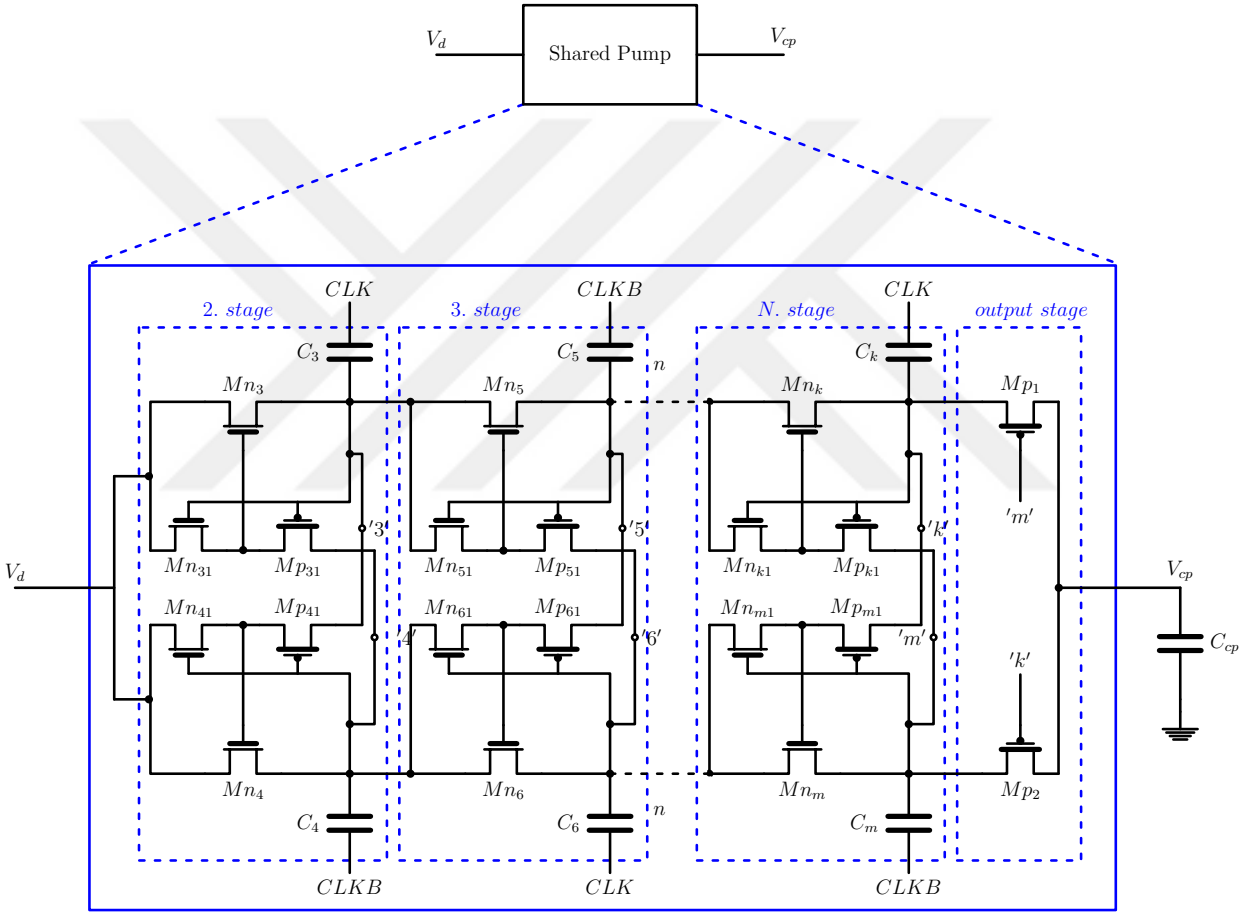

Figure 5.4: Circuit diagram of the shared pump.

$$
\begin{aligned}
V_{cp} &= V_d + (n-1) \times \Delta V \\
&= V_d + \sum_{i=1}^{n-1} (V_{in} - \frac{I_{out,i}}{C_i \times f}),
\end{aligned}
\tag{5.1}
$$

where ΔV is the voltage fluctuation at each pumping node, V_{in} is the clock supply voltage, C_i is the pumping capacitance at the i^{th} stage.

Table 5.2: The operation of N. stage at the Part B.

CLK &CLKB status	Transistor turns ON	Capacitor voltage
CLK=high	M_{n_m}, $M_{p_{m1}}$	C_m=(n-1)*V_{DD}
CLKB=low	$M_{n_{k1}}$	C_k=n*V_{DD}
CLKB=high	M_{n_k},$M_{p_{k1}}$	C_k=(n-1)*V_{DD}
CLK=low	$M_{n_{m1}}$	C_m=n*V_{DD}

5.1.2.3 Reverse currents

The shared-stage charge pump has one oscillator circuit to drive and charge capacitors and to assist transistors on/off. When an anode is impaired by bioturbation, the corresponding input voltage to the unit at Frontend Pump is close to zero, not enough to start up. However, the oscillator circuit still provides clock signals to this unit, and these clock signals always keep one of the output transistors (e.g., $M_{pa_{11}}$ in Fig. 5.3) on. Therefore, the shared-stage charge pump circuit will have reverse currents at this unit in the presence of bioturbation. For demonstration purpose, an example with two first-stage units at Frontend Pump followed by one stage at Shared Pump is shown in Fig. 5.5a. Reverse currents cause non-trivial energy losses, which result in degradation in energy harvesting performance.

In order to solve this problem, we develop a scheme by introducing two inverters before clock signals CLK and $CLKB$ as the clock buffers at each first-stage unit in Frontend

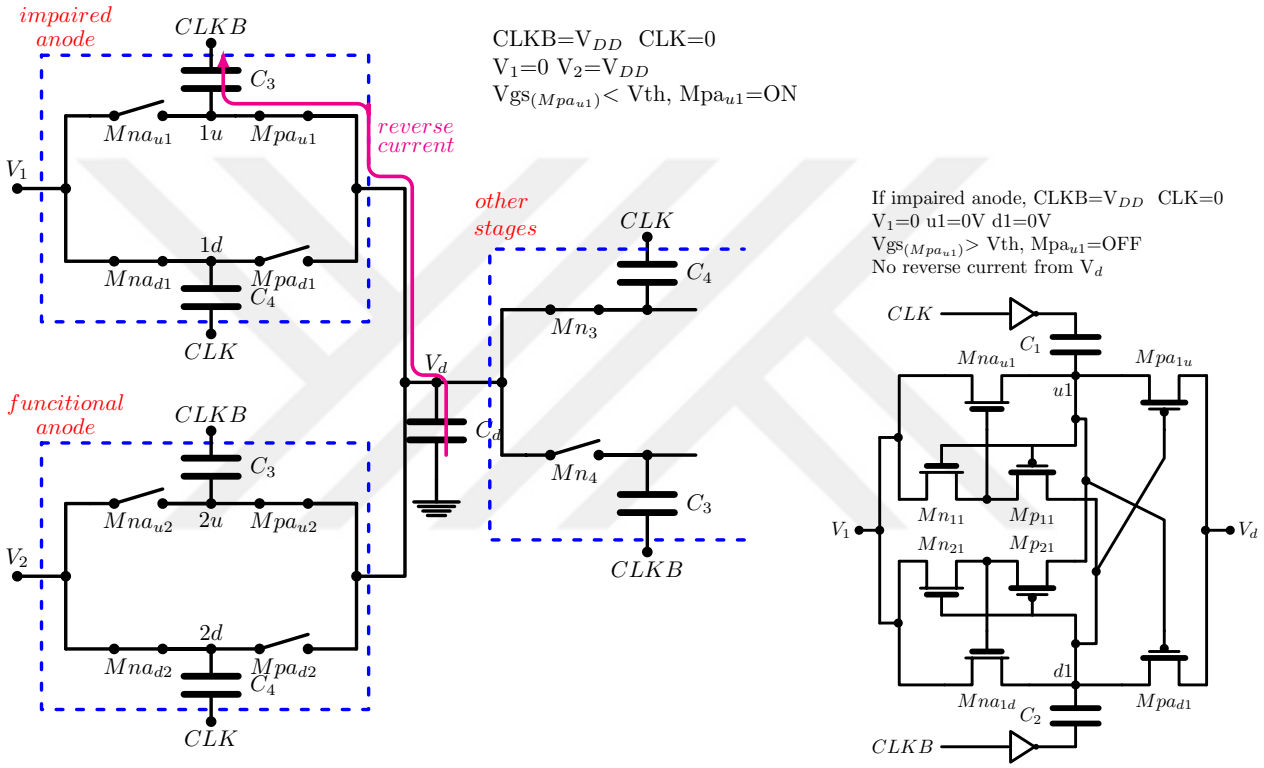

(a) An example of reverse currents flowing into the pumping unit with the impaired anode. Mna and Mpa refer to NMOS and PMOS transistors, respectively. Impaired anode case, the electrical potential difference between shared cathode and impaired anode is zero i.e. V_1=0. Note all transistors are not shown.

(b) The proposed scheme using clock buffers to circumvent reverse charging currents. Add two inverters before clock signals and inverters are powered by their corresponding input i.e. V_1.

Figure 5.5: Illustration of reverse currents and solution scheme for that.

Pump, as shown in Fig. 5.5b. These two inverters are powered by the potential difference between the common cathode and the corresponding anode of the unit. To drive these clock buffers, the potential difference should be stable enough; otherwise (e.g., in the presence of bioturbation), these clock buffers receive no power and the output transistors at Frontend Pump are always off, i.e., there will be no reverse current flowing back into this unit. In this manner, reverse currents in Frontend Pump are eliminated.

Figure 5.6 shows some results to evaluate reverse currents in the proposed shared-stage charge pump circuit. As shown, the design without inverter clock buffers obtains a large reverse current, whose value reduces with the increase in the number of impaired anodes. This is expected as more anodes are impaired by bioturbation, the number of functional anodes is reduced, which also reduces the amount of reverse currents. In comparison, the design with inverter clock buffers has almost no reverse current under all situations.

Reverse currents also affect the output voltage (as shown in Fig. 5.6b) and power efficiency (as shown in Fig. 5.6c), as they cause internal energy losses. If no anode is impaire, the output voltage and power efficiency for non-inverter shared-stage charge pump are better than the one with inverters due to design overheads introduced by the inverter clock buffers. Overall, the design with inverter clock buffers has better output voltage and power efficiency.

5.1.2.4 Optimization for the shared-stage charge pump

Achieving maximum voltage and power conversion efficiencies are essential for MFCs due to their very limited output power. In order to get the maximum voltage and power conversion efficiencies of the shared-stage charge pump, design parameters (e.g. number of stages, current consumption, capacitor values, transistor sizes, etc.) should be appropriately selected. Some previous studies [47], [48] defined a general charge pump design strategy. This design strategy cannot be applied to the shared-stage charge pump because of its unique structure. Thus, a new design strategy and optimization method are required. In (5.1), the output voltage of Shared Pump is given without considering Frontend Pump. For optimizing design

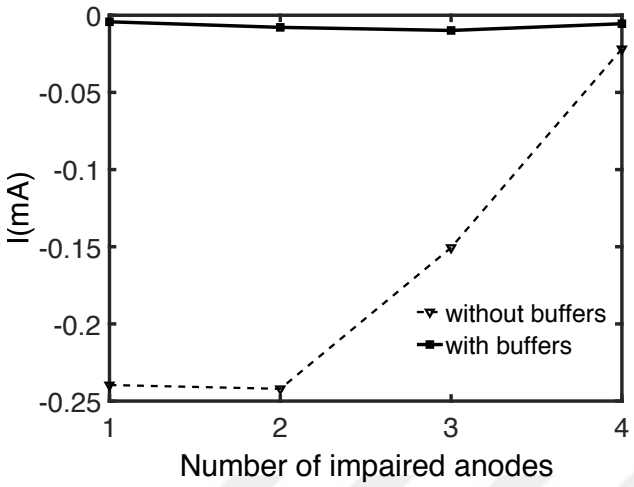

(a) Reverse Current

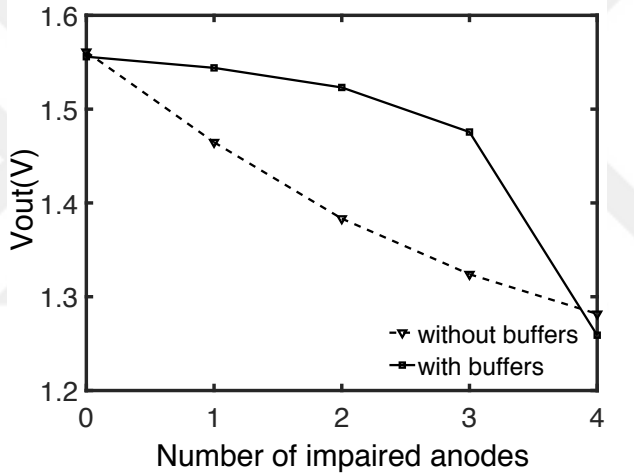

(b) Output voltage

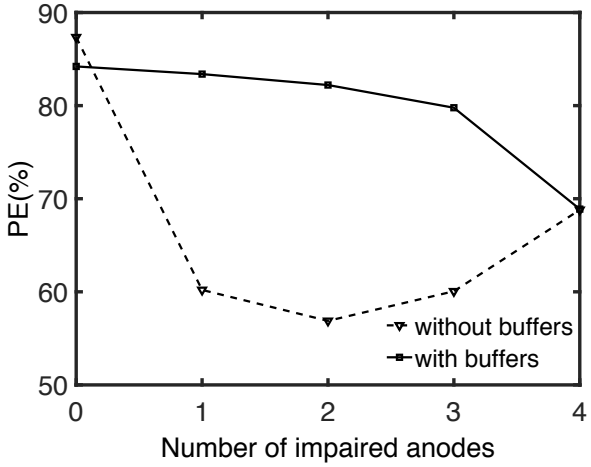

(c) Power efficiency

Figure 5.6: Performance comparison and simulation of reverse currents at the shared-stage charge pump with inverters and non-inverters.

parameters, the number of functional anodes should be taken into account.

Considering that an N-stage shared-stage charge pump has a clock frequency f and its output voltage is

$$V_{out} = (N+1) \times V_{DD} - \left[\frac{I_L \times B}{f \times C_1 \times K} + \frac{I_L}{f \times C_2} \times (N-1) \right] \tag{5.2}$$

where I_L is the output current, B is the number of functional anodes, C_1 and C_2 are the charge capacitance of Frontend Pump and Shared Pump, respectively. K is a factor which is defined current contribution constant by the number of functional anodes B in the multi anode MFC and expressed as

$$K = B - B \times \sigma_1(n, I_{cell}) \tag{5.3}$$

where B is the number of functional anodes in the MFC, and the value of parameter $0< \sigma_1(n, I_{cell})<1$ represents the non-ideal current loss in the multi-electrode configuration [1].

The first term in (5.2) is referred to the pump output voltage in the case of a pure capacitive load. The second term is referred to the voltage loss in the case of a current load. This term has two components: the first one demonstrates the effect of other stages on the pump output ($\frac{I_L}{f \times C_2} \times$(N-1)), and the second one shows a relationship between the number of first stages and the number of functional anodes, which demonstrates how a number of functional anodes affects on the pump output voltage.

The number of stages in the proposed charge pump design is determined for a capacitive load because there is a switch between the shared-stage charge pump and the boost converter. This switch isolates the charge pump from the current load. We define the number of stages as

$$N = \frac{V_{out}}{V_{DD}} - 1 \tag{5.4}$$

In order to fully transfer the stored charge from a capacitor (e.g., C_1) at Frontend Pump to a capacitor (e.g., C_2) at Shared Pump, the capacitance of the stage at Frontend Pump should be much less than the one at Shared Pump. Otherwise, the remaining charges at the first stage will diminish the pumping capability due to inefficiently transffering the charge. This sets a boundary condition as

$$C_2 \leq C_1 \times A \tag{5.5}$$

where A is the number of anodes in the MFC.

Substituting (5.5) into (5.2), the capacitance of a stage in (5.2) is derived as

$$C_1 = \frac{I_L(\frac{N-1}{A} + \frac{B}{K})}{f[(N+1) \times V_{DD} - V_{out}} \tag{5.6}$$

The efficiency of the shared-stage charge pump for the multi-anode MFC can be expressed as

$$\eta_{cp} = \frac{\sum_{i=1}^{A} P_{in_{ai}} - \sum_{i=1}^{A} P_{loss_{ai}} - P_{loss_{shared}}}{\sum_{i=1}^{A} P_{in_{ai}}} \tag{5.7}$$

where $P_{in_{ai}}$, $P_{loss_{ai}}$ and $P_{loss_{shared}}$ are the input power which is the power between the shared-cathode and corresponding anode, loss power of fronted pump stage and loss power of the shared pump, respectively.

5.1.3 Energy Accumulation and Transfer Control Circuit

Energy accumulation is achieved by multi-anode MFC through the shared-stage charge pump to charge the storage capacitor (C_{cp}). After the storage capacitor reaches at the discharge start voltage ($V_{discharge}$), accumulated energy at C_{cp} capacitor is delivered to the load. When C_{cp} capacitor voltage drops to the recharge start voltage (V_{charge}), the transfer energy is cut off. Therefore, it requires a control circuit to manage these operations. The proposed energy accumulation and transfer control circuit is shown in Fig. 5.7.

Energy accumulation initially charges the storage capacitor. The pMOS transistor $P1$ is

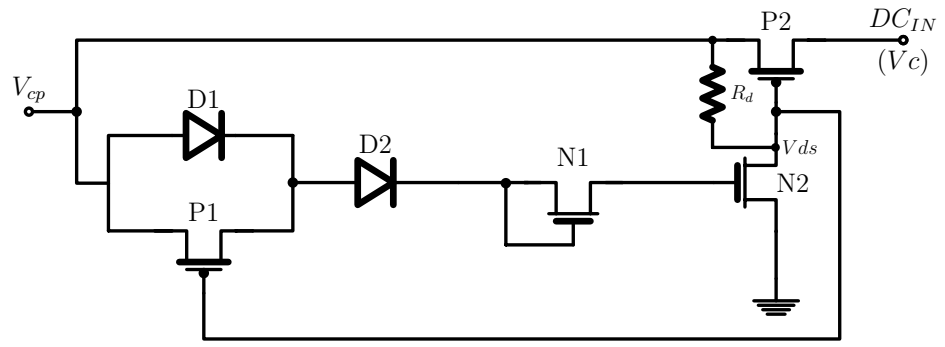

Figure 5.7: Energy accumulation & transfer control circuit diagram.

cut off since the resistor conducts as a short circuit so that the $P1$ transistor gate voltage is equal to the capacitor voltage. The gate voltage V_{g2} of the nMOS transistor $N2$ can be expressed as

$$V_{g2} = V_{cp} - 2 \times V_D - V_{tn1}, \tag{5.8}$$

where V_D is voltage drop over the diode, and V_{tn1} is the threshold voltage of the nMOS transistor $N1$.

When V_{g2} increases above its threshold voltage V_{tn2} (i.e. $V_{g2} \geq V_{tn2}$), $N2$ becomes conducting. Since its source connects to the drain and their voltages are equal to zero, the gate voltages of the pMOS transistors $P1$ and $P2$ drop to zero. As a result, $P1$ and $P2$ turn on and the boost converter is connected to the storage capacitor through $P2$. The storage capacitor starts to discharge and transfers the stored energy to the boost converter. Substituting $V_{g2} = V_{tn2}$ into (5.8), the super capacitor's discharge start voltage $V_{discharge}$ can be expressed as

$$V_{discharge} = V_{tn1} + V_{tn2} + 2 \times V_D. \tag{5.9}$$

As diode $D1$ is bypassed by $P1$, and the gate voltage V_{g2} of $N2$ initially undergoes a sudden increase with the amount equal to the voltage drop of $D1$, i.e.,

$$V_{g2} = V_{cp} - V_D - V_{tn1}. \tag{5.10}$$

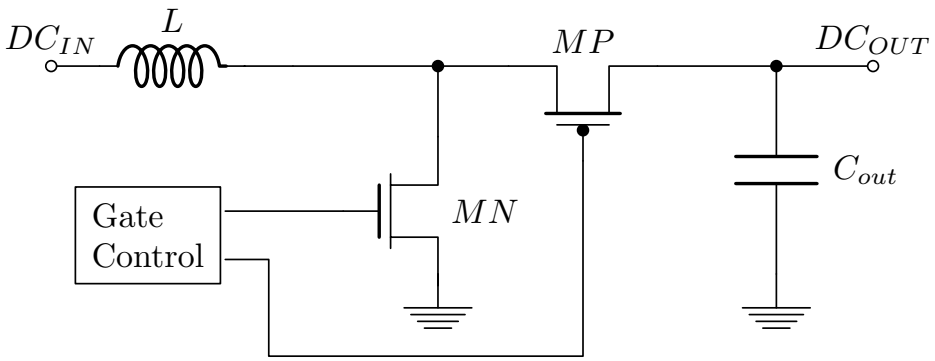

Figure 5.8: Circuit diagram of the boost converter.

This increase will keep $N2$ on till the voltage of the super capacitor V_{cp} drops to the charge start voltage V_c. From (5.10), as the voltage of the super capacitor V_{cp} drops, V_{g2} reduces as well. Once V_{g2} reaches the threshold voltage V_{tn2} of $N2$, $N2$ is cut off, which also turns off $P1$ and $P2$ and thus disconnects the boost converter from the super capacitor. The super capacitor will be charged again. Thus, substituting $V_{g2} = V_{tn2}$ into (5.10), the charge start voltage V_{charge} can be expressed as

$$V_{charge} = V_{tn1} + V_{tn2} + V_D. \tag{5.11}$$

These processes will be repeated over the time as long as the multi-anode MFC generates output power. Note that the selection of the discharge ($V_{discharge}$) start voltage level needs to be considered for the worst case scenario (i.e. four anodes failed). For this study, the voltage level of 1.35V is used for the discharge start voltage.

5.1.4 Boost converter

Most of DC-DC boost converters based on switching through an inductor [72] are able to step up a dc voltage to a higher output voltage due to the LC effect. Typically, boost converters can operate in two modes: continuous conduction mode (CCM) and discontinuous conduction mode (DCM). CCM allows inductor current to flow negatively if applying small

load. In contrast, DCM prevents the current to flow negatively and is thus more efficient [73]. A basic diagram of the boost converter is shown in Fig. 5.8. The transfer function of an ideal boost converter is

$$\frac{V_{out}}{V_{in}} = \frac{1}{1-dc} \quad or \quad \frac{T_n}{T_p} + 1 \tag{5.12}$$

where the duty cycle dc is the ratio of on time of the NMOS M_N to the period length i.e. the reciprocal of switching frequency f, T_p is on time of the M_P transistor and T_n is on time of the M_N transistor.

We developed a boost converter with discontinuous conduction mode for single-anode MFCs [3], as shown in Fig. 5.9. The converter starts operating when the switch placed between the charge pump and the converter is enabled to transfer stored energy to the load. As the switch is on (i.e., $P2$ in Fig. 5.7), the current flowing through the inductor increase since NMOS transistor M_N is turned on by the gate control circuit. When the current reaches the maximum current ($I_{L_{max}}$), M_N transistor turns off since transistor drain voltage increases over V_{ref}, which will pull down the output of the comparator. The reference voltage V_{ref} is generated by the circuit discussed in [74], which is activated once the super capacitor is connected to the boost converter.

Note that the peak inductor current $I_{L_{max}}$ can be controlled by adjusting inductor L, frequency f, and M_N and M_P transistors' on time T_N and T_P. The peak inductor current can be expressed as

$$I_{L_{max}} = \frac{V_{in}T_n}{Lf} = \frac{(V_{out} - V_{in})T_p}{Lf} \tag{5.13}$$

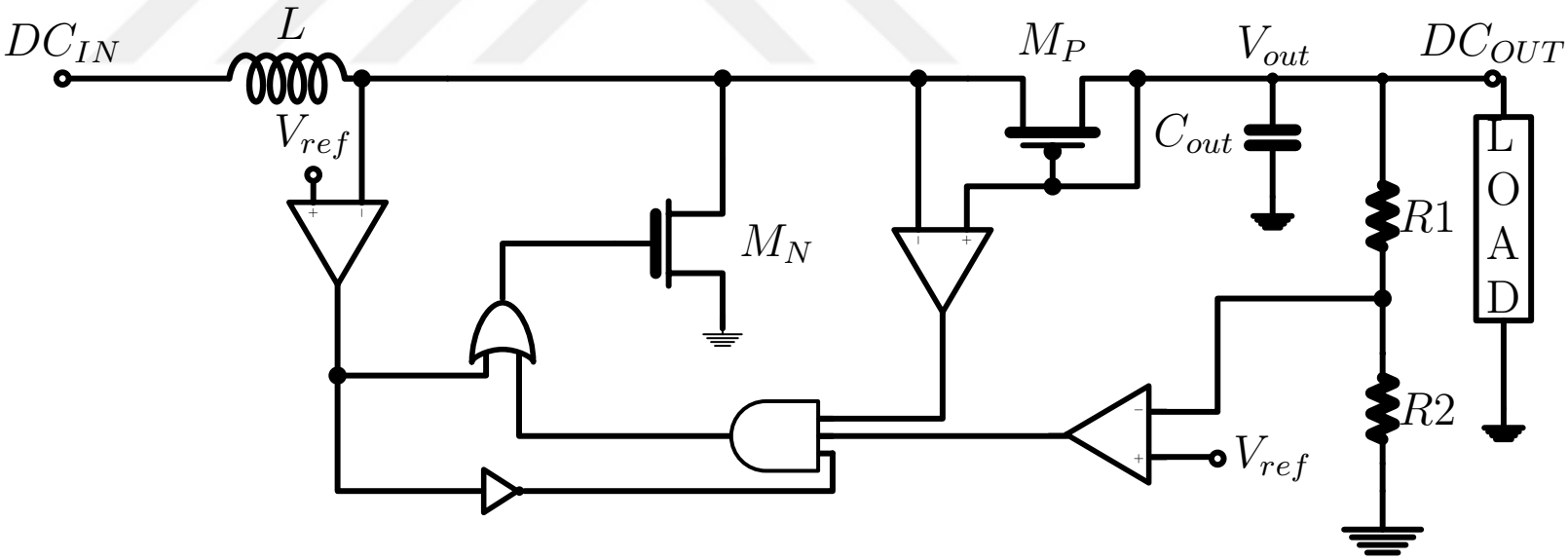

Figure 5.9: Circuit diagram of DC-DC boost converter associated with gate control circuit[3].

Every cycle the stored energy in L is delivered to C_{out}, as

$$E_{store} = \frac{1}{2} L I_{L_{max}}^2 = \frac{1}{2} C_{out} \Delta V^2 \tag{5.14}$$

PMOS transistor M_P facilitates $I_{L_{max}}$ current to flow and the energy is transferred to the output capacitance (C_{out}). Substituting (5.13) into (5.14), the voltage boost obtained at (C_{out}) at the end of each cycle is

$$\Delta V = \sqrt{\frac{L I_{L_{max}}^2}{C_{out}}} = \sqrt{\frac{V_{in}^2 T_n^2}{L f^2 C_{out}}} \tag{5.15}$$

The converter output voltage steps up to reach the demanded voltage level after a couple of M_N/M_P on and off cycles. When the output voltage reaches the demanded voltage level, the gate control circuit should regulate the transistors' on/off status to maintain this voltage level. This is achieved by using a voltage divider (as shown Fig. 5.9) at the output and feedback to the control circuit. A stable output voltage is expressed as

$$V_{out} = V_{ref} \times \frac{R1 + R2}{R2} > V_{cut} \tag{5.16}$$

where V_{cut} is the cut-off voltage of the load.

In order to maintain such an energy transfer mechanism for variable loads, inductor L and output capacitor C_{out} should be adjusted for the best efficiency. In our design, the inductor L and output capacitance C_{out} use external components to achieve this flexibility.

The boost converter can obtain the output voltage level as long as energy accumulation and transfer processes are repeated over time. The energy conversion efficiency is given by

$$\eta_{dc} \approx \frac{V_{out}^2 \Delta T / R}{\frac{1}{2} C_{cp} (V_d^2 - V_c^2)} = \frac{\frac{1}{2} C_{cp} (V_d^2 - V_c^2) - P_l \Delta T}{\frac{1}{2} C_{cp} (V_d^2 - V_c^2)} \tag{5.17}$$

where ΔT is the duration that the load can be powered, R is the effective resistance of the

load, and P_l is the internal loss of the boost converter.

5.2 Results and Discussion

Table 5.3: Values of circuit parameters

Parameters	Symbol	Value
Shared-stage charge pump		
Capacitance at Fronted pump	C1	50pF
Capacitance at Shared pump	C2	250pF
Output capacitor	C_{cp}	100mF
Switch circuit		
Resistor	R_d	1MegΩ
PMOS switch size (W/L)	P2	255u×40/100n
Boost converter		
Inductor	L	16μH
Output capacitor	C_{out}	47μF
Resistor	R1	9MegΩ
Resistor	R2	2MegΩ
NMOS switch size (W/L)	MN	100u×25/100n
PMOS switch size (W/L)	MP	255u×40/100n
Input & Load specification		
Input voltage (min)	V_{DD}	0.35V
Output voltage	V_{out}	3.3V
Each input power (max)	$P_{in_{ai}}$	25μW
Output power	P_{out}	165mW
Required power for hydrophone	P_{load}	95mW

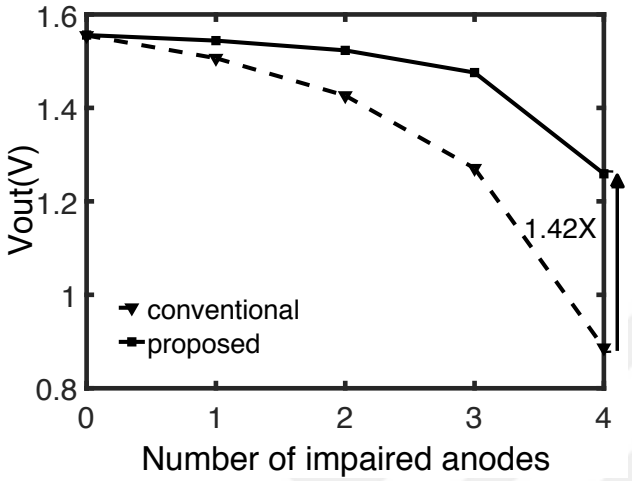

(a) Output voltage vs. number of impaired anodes

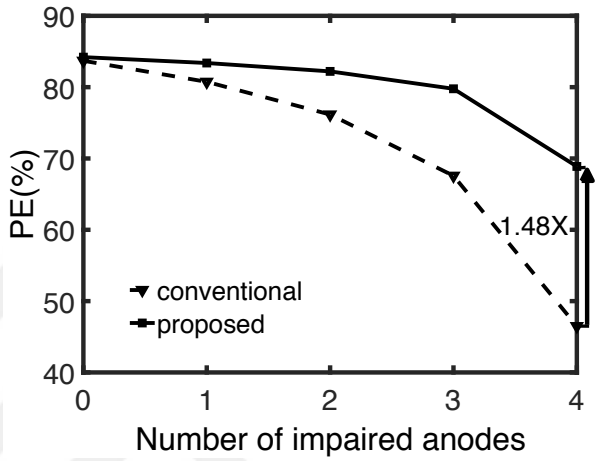

(b) Power efficiency vs. number of impaired anode

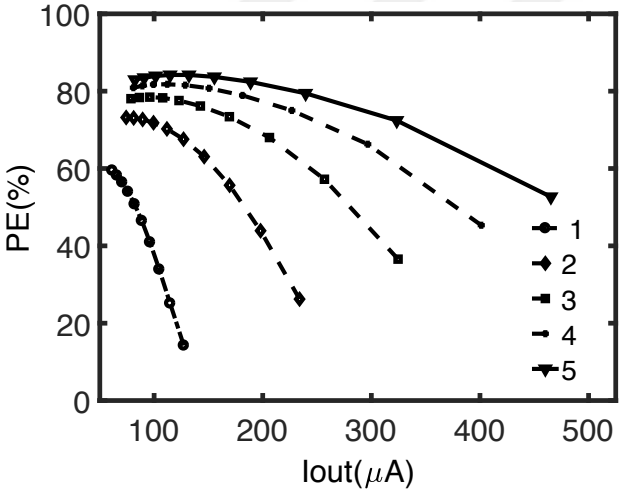

(c) Power efficiency under different loads with number of functional anode for conventional design

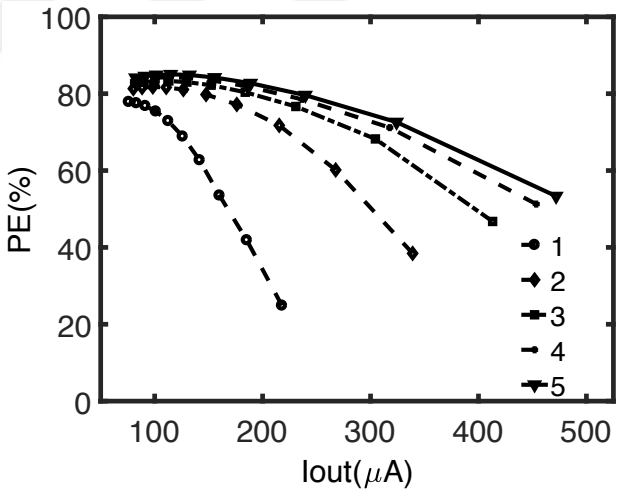

(d) Power efficiency under different loads with number of functional anode for the shared-stage charge pump

Figure 5.10: Performance comparison between conventional design and the shared-stage charge pump.

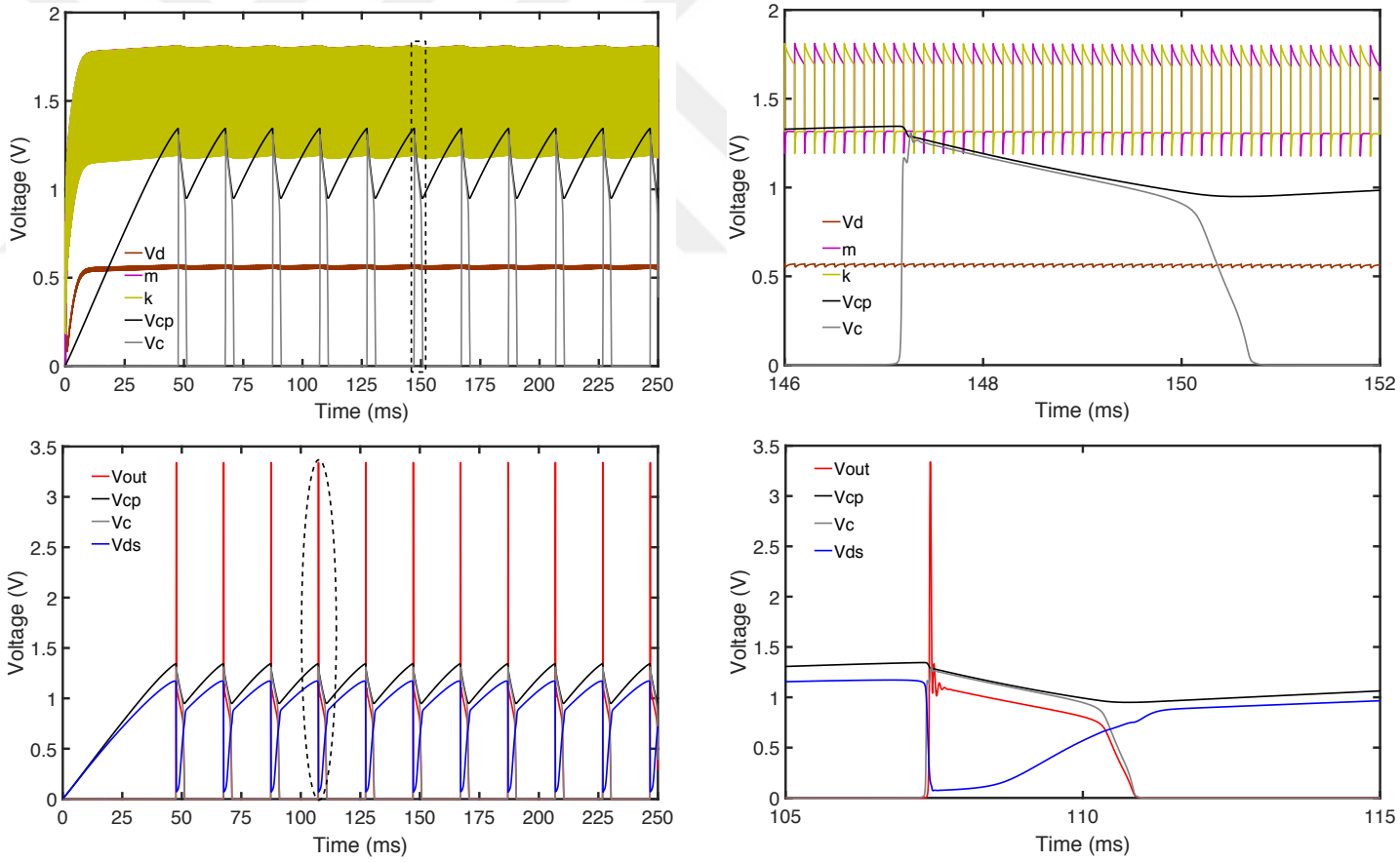

(a) Waveforms

(b) Zoomed waveforms

Figure 5.11: Voltage waveforms at different circuit nodes of the shared charge pump, the storage element, the switch circuit, the boost converter and the load.

The proposed energy harvesting circuit was evaluated in a 90nm CMOS process. An analytical multi-anode MFC model [1] was utilized to emulate the output currents and voltages for a five-anode and one shared cathode MFC configuration. The shared-stage charge pump consists of five first-stage pumping units in Frontend Pump and three common stages in Shared Pump. The output of the converter is used as the power supply for a resistive load, which is an equivalent circuit of a hydrophone. The parameters for the proposed power converter is tabulated in Table 5.3 along with the load (i.e. hydrophone) specification.

In order to evaluate the impact of anode impairments on the performance of the shared-stage charge pump, the charge pump is individually tested. A comparison is made between the shared-stage charge pump and conventional charge pumps whose inputs are connected to one anode each (see Fig. 5.1). Conventional charge pumps consist of five individual charge pumps and each charge pump has four stages. The shared pump stage in this work (see Fig. 5.4) is deployed as a pump stage for conventional one is used to frame conventional four stage charge pump. To test conventional charge pumps whose circuit connection is similar to Fig. 5.1, the pumps are designed and evaluated with proposed one. To make a fair comparison, the total pumping capacitors and frequency for both circuits are same. As shown in Figs. 5.10a and 5.10b, the shared-stage charge pump degrades at a slower rate than the conventional one. The shared-stage charge pump achieves 42% and 48% higher output voltage and power efficiency, respectively, than the conventional one when four anodes fail, which is the worst-case scenario. These achievements are related to the internal resistance of a charge pump circuit. The shared-stage charge pump achieves more power efficiency than the conventional design under varying functional anodes due to its simple structure and low internal parasitic resistance, as shown in Figs. 5.10c and 5.10d.

In order to show all circuit operations for several charging, discharging and powering cycles, proposed power converter is tested with small capacitance values of 10nF and 0.1nF for the storage capacitor C_{cp} and the output capacitor of the boost converter C_{out}, respectively. In Fig. 5.11, top figure shows the voltage waveforms at the output of the fronted pump V_d,

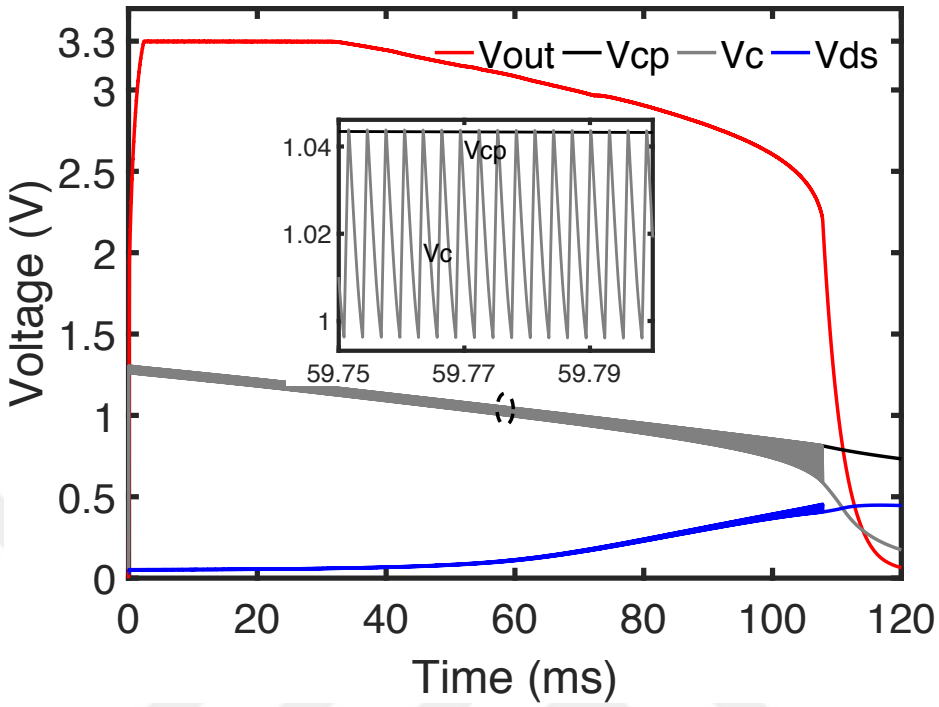

Figure 5.12: Full load condition. Waveforms for the gate voltage of the P2 PMOS transistor V_{ds}, the capacitor voltage V_{cp}, boost converter input voltage V_c and hyrophone voltage (i.e. the load) V_{out} at the super capacitor of 50mF. Zoomed voltage waveforms of V_{cp} and V_c.

the outputs at the shared pump (see Fig. 5.4) m and k, the storage node V_{cp} and the input of the boost converter V_c. Bottom figure in Fig. 5.11 shows voltages at the output of the boost converter V_{out}, the gate voltage of the P2 PMOS transistor V_{ds}, V_c and V_{cp}.

The fronted pump output capacitor C_d is charged through multi-anode MFC and its voltage V_d reaches up to 563mV. The voltage of V_d is used as a voltage supply for the shared pump. The voltages at outputs of the shared pump whose nodes are at m and k are complementary to charge the super capacitor C_{cp}. Once the capacitor reaches the discharge start voltage of $1.35V$, V_{ds} starts decreasing down to zero. Therefore, $P2$ transistor is turned on and the capacitor starts discharging. The boost converter connects to the capacitor and the input voltage of the converter is equal to the voltage of the capacitor. The boost converter shortly starts to operate and its output voltage jumps to about 3.4V. The output level is just a short spark voltage and then equal to the input voltage V_c drop over Mp PMOS transistor

(i.e. V_{out}=V_c-V_{drop}). However, this voltage level is expected to maintain during discharging time of the capacitor. This is mainly due to the fact that there is no sufficient stored energy at the capacitor (i.e. C_{cp}=10nF) and it needs large capacitance values (i.e. millifarads range capacitances).

Once the capacitor voltage reduces to the charge start voltage of $0.9V$, V_{ds} starts to increase and $P2$ switches off. This behavior indicates that stored energy at the capacitor C_{cp} is transferred to the inductor once the capacitor voltage V_{cp} changes from $1.35V$ to $0.9V$. Once $P2$ switches off, the capacitor starts to charge again through the multianode MFC. The charging and discharging processes are periodically repeated over the time.

Fig. 5.12 shows the capacitor output, the boost converter input and output voltages with the hydrophone as the load. Once the capacitor C_{cp} reaches the discharge start voltage of 1.35V, the boost converter is connected to the capacitor C_{cp} through $P2$ switch (see Fig. 5.7). It takes roughly 2.4ms for the output capacitor to get the output voltage of 3.3V. Thus, the stored energy at the capacitor C_{cp} is delivered to the hydrophone through the switched inductor, which results in step-up the converter output voltage to 3.3V. The stored energy at the capacitor C_{cp} is dissipated by the hydrophone, which draws 50mA current on average while making the capacitor voltage V_{cp} gradually discharged to the voltage of 1.2V. After that voltage level, output voltage gradually decreases to 2.5V while discharging the capacitor voltage to the charge start voltage of 0.85V. The hydrophone still dissipates the stored energy at the capacitor C_{cp} till the charge start voltage. Note that the hydrophone consumes the power of 95mW at the output voltage of 2.5V which is an enough power level for keeping operation of the hydrophone.

Once the capacitor C_{cp} reaches to the charge start voltage of 0.85V, the switch is off and the inductor L is disconnected from the capacitor C_{cp}. The hydrophone output voltage will drop to zero and the capacitor C_{cp} is charged back through the shared-stage charge pump by the multi-anode MFC. This charge back process is repeatedly over time, i.e., the load operates in a burst mode due to the low power output of the multi-anode MFC.

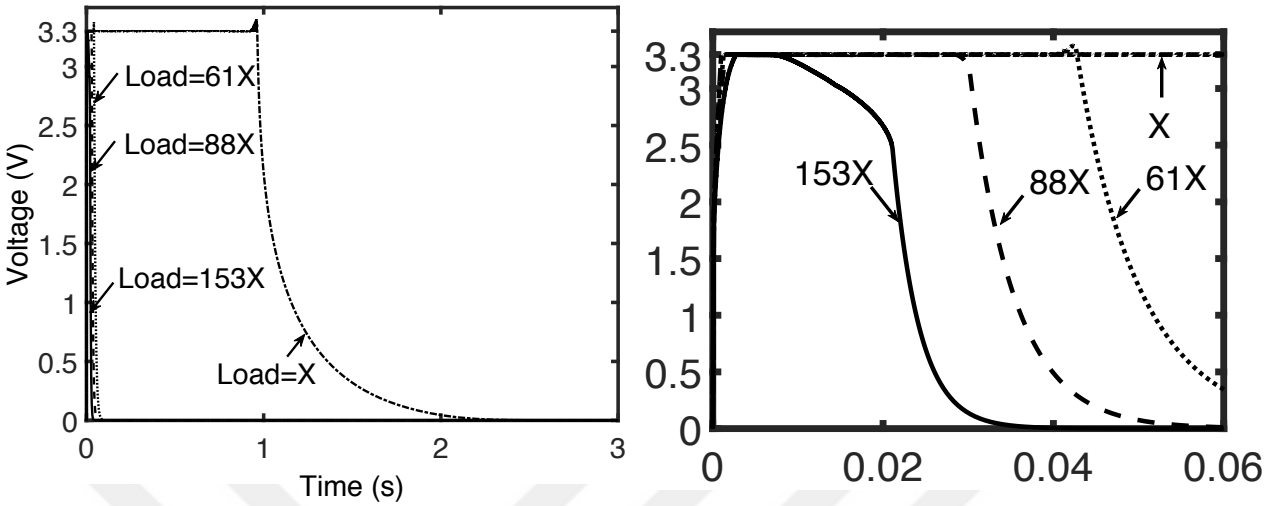

(a) (b)

Figure 5.13: (a)The load voltage waveforms for four load cases at the super capacitor of 10mF. (b) Zoomed voltage waveforms at the time range of 0-60ms.

A question arises that, during the switch P2 is kept turning on why the hydrophone voltage is started to lower from 3.3V to 2.5V at the capacitor voltage of 1.2V instead of keeping at a constant voltage of 3.3V. In order to investigate profoundly that issue, four different load cases are tested with the super capacitor of 10mF. First the hydrophone which is a heavy load at the power of 165mW (i.e. the load is denoted as Load=153X) and then two more heavy loads (i.e. Load=88X at power of 95mW and Load=61X at power of 65mW) are tested. Second case, a light load at the power of 1.08mW (i.e. denoted as Load=X) is tested. The load voltage and inductor current waveforms are shown in Fig. 5.13 and Fig. 5.14. As observed from the figure, in the light load and the last two heavy loads (i.e. 88X and 61X) there is no voltage degradation during the super capacitor voltage downs from 1.35V to 0.85V. In other words, the expected voltage level at the output of the boost converter is preserved (i.e. 3.3V). This is because in the light load, the boost converter does not always need to switch on/off the power transistors (i.e. MN and MP transistors in Fig. 5.9). Also, these loads give the boost converter a time room (see Fig. 5.14 to start next switching on/off cycles for the power transistors after the output voltages reaches at the steady state (i.e.

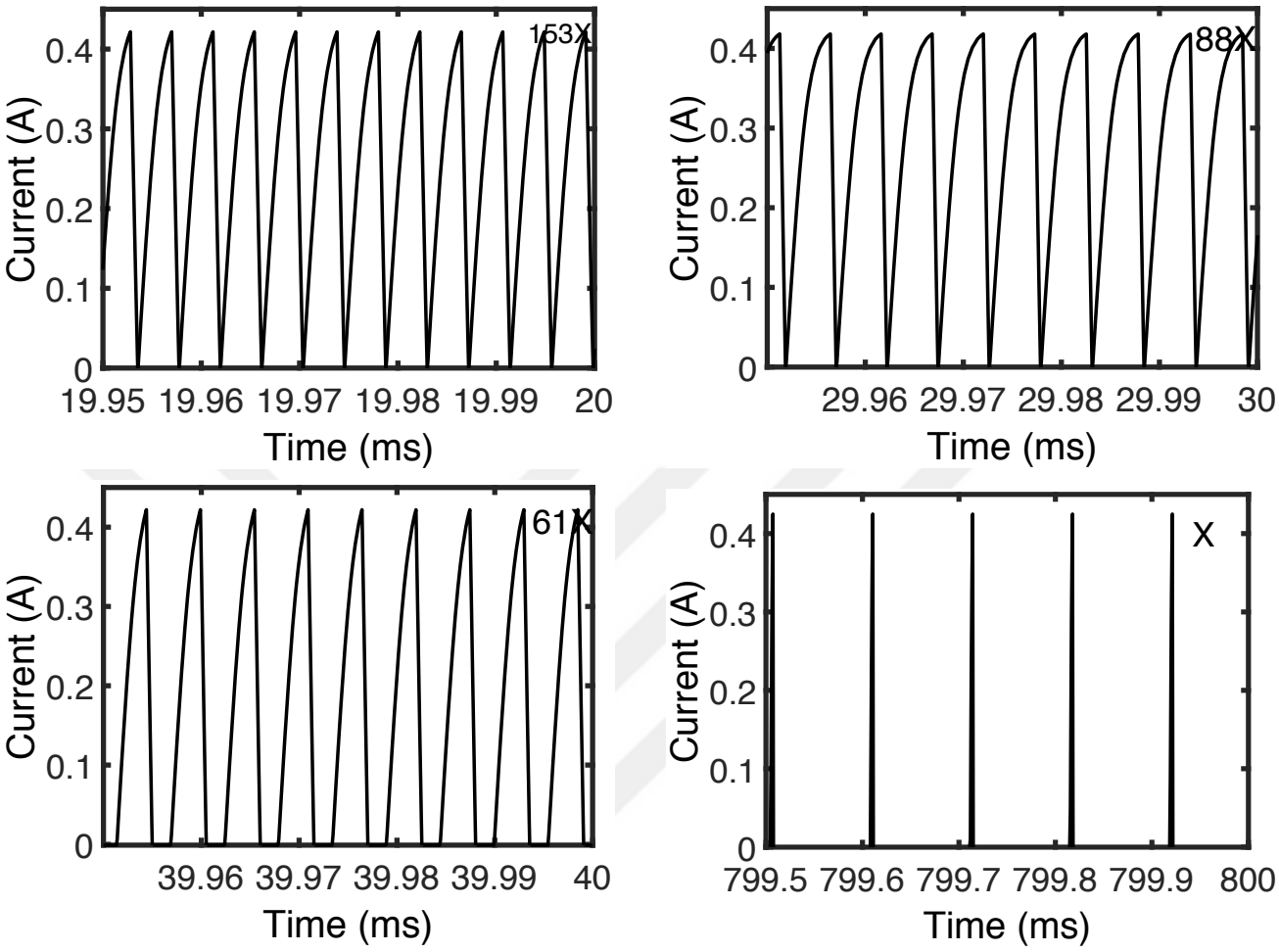

Figure 5.14: Current waveforms at the inductor I_L under varied loads.

3.3V).

However, in the most heavy load (i.e. 153X), the switching frequency of the boost converter is not kept a constant level at the super capacitor voltage downed from 1.35V to 0.85V. The switching on/off cycles takes frequently without the time room (see top left figure in Fig. 5.14 . Once the super capacitor voltage V_{cp} discharges to 1.2V, the switching frequency is changed because the operations of the components (e.g. comparators, gates etc.) at the boost converter are affected by the voltage level i.e. does not operate properly. The voltage level at downing from 1.2V to 0.85V is not enough to keep the voltage of 3.3V at the load. To operate properly for the most heavy load, the boost converter requires an input

voltage as low as $1.2V$, but for others as low as 0.85V. In this study, proposed design powers up the heavy load (i.e. hydrophone) with changing the super capacitor voltage V_{cp} levels from 1.35V to 0.85V since the required power for the hydrophone (i.e. 95mW) is provided.

The overall efficiency of the energy harvesting circuit is a product of efficiency of the shared-stage charge pump (5.7) and the boost converter (5.17), and expressed as

$$\eta_{overall} = \eta_{cp} \times \eta_{dc} \tag{5.18}$$

The efficiency of the circuit was calculated with different functional anodes, as shown in Fig. 5.15. The proposed energy harvesting system shows 42% improvement in efficiency than the conventional design under the worst condition, i.e., the presence of one functional anode case.

Table 5.4: Comparison with state-of-the-art works

Circuit	[2] (measurement)	[64] (measurement)	[75] (measurement)	[36] (simulation)	This work (simulation)
MFC Source	Single cathode	Multi cathode (4)	Single cathode	Multi cathode (4)	Single cathode
Topology	Multi anode (3)	Multi anode (4)	Single anode	Multi anode (4)	Multi anode (5)
Output Voltage	3.3V	1.6V	2.5V	1.55V	3.3V
Maximum Output Power	NA	33.5mW	250μW	NA	165mW
Efficiency	35.02%	32.8%	58%	NA	61.46%
Technology	Discrete	Discrete	0.5μm	0.13μm	90nm
Bioturbation/Robustness	Yes	Yes	No	No	Yes

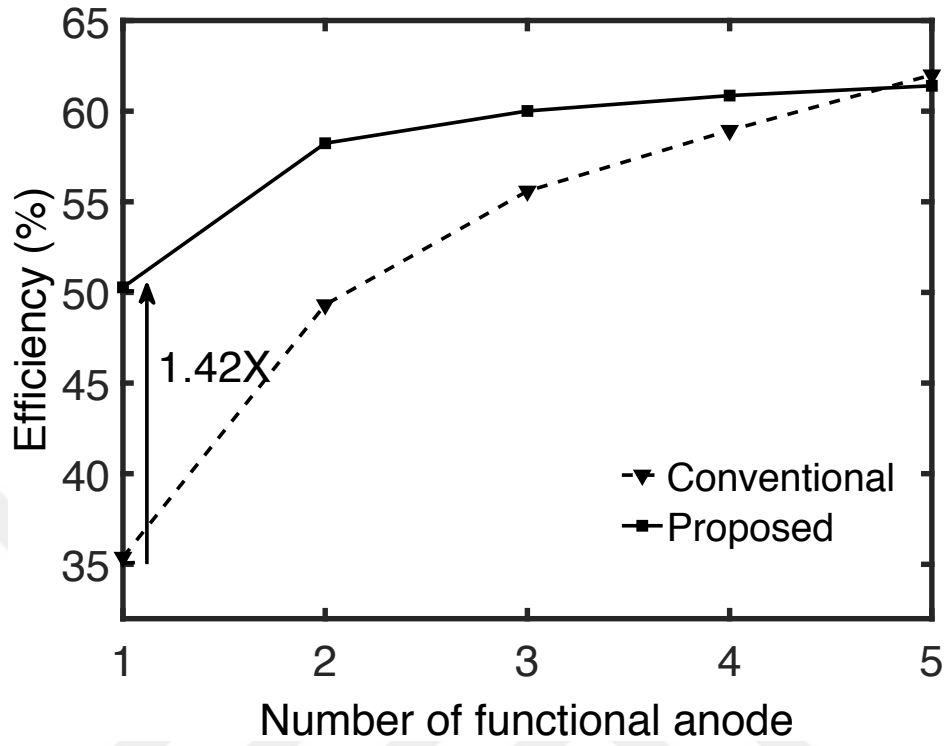

Figure 5.15: Overall efficiency with varying number of functional anodes.

Table 5.4 shows a comparison of the performance of proposed power converter with previously published MFCs energy harvesting circuits. As observed from the table, proposed converter achieves the highest efficiency among discrete state-of-the-art works [2], [64] due to the implementation of the integrated circuit. This study is based on a predict model and its results are carried out by simulation. It is clear that there will be some degradation in overall efficiency of proposed converter, but some techniques with maximum power extraction can makes some enhancement on the efficiency.

Compared with [75], a high efficiency is achieved with MPPT implementation under light load condition (i.e. the maximum power of 250μW). In addition, it depends on single converter (i.e. boost converter) without considering bioturbation issue. However, proposed converter operates under heavy load condition (i.e. 165mW) without MPPT implementation. Also, proposed converter is based upon two converters (i.e. shared charge pump and boost converter) to process the energy twice with different efficiency rates before powering the

load, thereby constraining the overall efficiency. The efficency of the boost converter in this study is 73%. Moreover, proposed converter is affectively able to address bioturbation by the number of five-anodes.

5.3 Conclusion

Bioturbation resilience for MFC in harsh ocean environment is achieved by employing multiple anodes with shared cathode. Energy harvesting circuit have been designed in this paper that allows automatically detect the impaired anodes due to bioturbation and to regulate output voltage as a demand voltage for load application. The shared-stage charge pump has distinct advantages, and provides 42% and 48% improvement in output voltage and power efficiency over the conventional multi charge pump. Design optimization of the harvesting circuit is considered for both the power efficiency and the impact of possible bioturbation problems. The detailed design of the harvesting circuit was discussed. The simulation results are in good agreement with the design specifications and to prove the effectiveness of the harvesting circuit.

Chapter 6

Summary and Conclusions

In order to accomplish batteryless operation of underwater devices, it is essential to harvest energy from aquatic environment to allow autunomous operation. The best candidate for energy harvesting from the surroundings i.e. aquatic environment is to implement microbial fuel cells as an energy source. An interface (i.e. power management system) needs between harvesters and loads due to inherently the low voltage and power at MFC outputs. Thus, this thesis has focused on four power management systems, making them more efficient in terms of power obtained (chapter 2), in terms of combining all sources (chapter 3) and compatible with MFCs that solved bioturbation (chapter 4 and chapter 5). In what follows, the specific contributions achieved are listed below.

Chapter 2: Maximum power point circuit

This chapter presents an inductorless power converter (i.e. charge pump) with the maximum power point for energy harvesting systems. As compared to conventinal capacitive based power converter, the proposed power converter is divided into two parts; first-stage and shared-stage. First-stage is the maximum power extraction stage by connecting a number of first-stage in parallel. First-stage achieves maximizing power extraction without increasing power dissipation and circuit complexity except increasing area. Shared-stage operates as conventional charge pump to step-up the merged output voltage of a number of first-

stage to a usable level by the application. Maximum power extraction is analyzed. Design methodology and optimization are discussed and incorporated into circuit implementation. The key contributions of this design are:

- For not only low-power energy source but also high-power energy source, the maximum power extraction is targeted by the proposed converter.
- The extracted power from energy sources enhances by range from 117% to 161% over the conventional design.
- The peak end-to-end efficiency is enhanced by 98% as compared to the conventional converter.

Chapter 3: Energy combiner circuit

This chapter presents an energy combiner circuit for multiple and homogeneous microbial fuel cells to enhance the drivability of the load for prolonged operation time. The combiner is based on output time-multiplexing scheme that connects outputs of converters in-order and equal time. Digital control circuit that configures the connection orders and the routing ways (i.e. either the load or the battery.) is presented. The stored energy at the converter outputs is fully transferred without loss of energy by routing the outputs to the load or an energy storage (e.g., a rechargeable battery or a super capacitor). The key contributions of this design are:

- This architecture allows all energy sources to simultaneously operate and include all sources to increase overall system reliability.
- It is self-powered i.e. does not need of a precharge voltage or external supply.

Chapter 4: Discrete anode decoupling circuit

In this chapter, a discrete power management system (PMS) for multi-anode BMFCs was developed to achieve bioturbation resilince in multi anode MFCs. The PMS includes a multi anode decoupling circuit, a switching circuit and a boost converter. The PMS starts an input voltage as low as 0.35V and regulates the output to 3.3V to power up underwater devices. The key contributions of this design are:

- The proposed PMS automatically disconnects the impaired anodes from the rest of the system for bioturbation resilience and better efficiency.
- The proposed PMS is self-starting, i.e., no need of extra power sources other than the BMFC.
- This work achieves higher efficiency with consideration of bioturbation as compared to previously published works.

Chapter 5: Integrated anode decoupling circuit

Chapter 5 focuses on a fully integrated power management circuit for multi anode MFCs. The integrated PMS consists of a shared-stage charge pump, an energy accumulation and transfer control circuit and a boost converter. The impaired anode decoupling is achieved in the Frontier stage of the shared-stage charge pump. The PMS starts an input voltage as low as 0.35V and regulates the output to 3.3V. The key contributions of this design are:

- The PMS automatically detects the impaired anodes and disconnects them from the rest of the system for better energy efficiency and robustness.
- The shared-stage charge pump has distinct advantages, and provides 42% and 48% improvement in output voltage and power efficiency over the conventional multi charge pump.
- Proposed PMS achieves a maximum efficiency of 62%.

- As compared to conventional design, Integrated power converter provides 42% improvement in overall efficiency.

As compared to chapter 4, the key contributions achieve with integrated PMS in chapter 5 are:

- The energy harvesting circuit minimizes the reverse leakage charge and the resulting efficiency degradation when one or several anodes are impaired by bioturbation, and
- The energy harvesting circuit has small complexity to reduce its internal energy losses.
- The energy harvesting circuit obtains higher efficiency.

Bibliography

[1] Udayarka Karra, Guoxian Huang, Ridvan Umaz, Christopher Tenaglier, Lei Wang, and Baikun Li. Stability characterization and modeling of robust distributed benthic microbial fuel cell (dbmfc) system. *Bioresource Technology*, 144:477 – 484, 2013.

[2] R. Umaz, C. Garrett, F. Qian, B. Li, and L. Wang. A power management system for multianode benthic microbial fuel cells. *IEEE Transactions on Power Electronics*, 32(5):3562–3570, May 2017.

[3] G. Huang, R. Umaz, U. Karra, B. Li, and L. Wang. In *International Symposium on Low Power Electronics and Design (ISLPED)*.

[4] M. Dini, A. Romani, M. Filippi, and M. Tartagni. A nanocurrent power management ic for low-voltage energy harvesting sources. *IEEE Transactions on Power Electronics*, 31(6):4292–4304, June 2016.

[5] K. W. R. Chew, Z. Sun, H. Tang, and L. Siek. A 400nw single-inductor dual-input-tri-output dc-dc buck-boost converter with maximum power point tracking for indoor photovoltaic energy harvesting. In *2013 IEEE International Solid-State Circuits Conference Digest of Technical Papers*, pages 68–69, Feb 2013.

[6] A. Mansano, S. Bagga, and W. Serdijn. A high efficiency orthogonally switching passive charge pump rectifier for energy harvesters. *IEEE Transactions on Circuits and Systems I: Regular Papers*, 60(7):1959–1966, July 2013.

[7] A. Das, Y. Gao, and T. T. H. Kim. A 220-mv power-on-reset based self-starter with 2-nw quiescent power for thermoelectric energy harvesting systems. *IEEE Transactions on Circuits and Systems I: Regular Papers*, 64(1):217–226, Jan 2017.

[8] Y. Qiu, C. Van Liempd, B. O. het Veld, P. G. Blanken, and C. Van Hoof. 5μw-to-10mw input power range inductive boost converter for indoor photovoltaic energy harvesting with integrated maximum power point tracking algorithm. In *2011 IEEE International Solid-State Circuits Conference*, pages 118–120, Feb 2011.

[9] G. Huang, R. Umaz, U. Karra, B. Li, and L. Wang. A power management integrated system for biomass-based marine sediment energy harvesting. *International Journal of High Speed Electronics and Systems*, 23:1450012 (1–20), 2014.

[10] Udayarka Karra, Eri Muto, Ridvan Umaz, Mike Kolln, Carlo Santoro, Lei Wang, and Baikun Li. Performance evaluation of activated carbon-based electrodes with novel power management system for long-term benthic microbial fuel cells. *International Journal of Hydrogen Energy*, 39(36):21847 – 21856, 2014.

[11] J. D. Park and Z. Ren. Hysteresis-controller-based energy harvesting scheme for microbial fuel cells with parallel operation capability. *IEEE Transactions on Energy Conversion*, 27(3):715–724, Sept 2012.

[12] B. Li J. Dai, X. Li and L. Wang. Design and modeling of an underwater energy harvesting system. In *International Symposium on Circuits and Systems (ISCAS)*.

[13] Fei Zhang, Lei Tian, and Zhen He. Powering a wireless temperature sensor using sediment microbial fuel cells with vertical arrangement of electrodes. *Journal of Power Sources*, 196(22):9568 – 9573, 2011.

[14] Timothy Ewing, Phuc Thi Ha, Jerome T. Babauta, Nghia Trong Tang, Deukhyoun Heo, and Haluk Beyenal. Scale-up of sediment microbial fuel cells. *Journal of Power Sources*, 272:311 – 319, 2014.

[15] Conrad Donovan, Alim Dewan, Huan Peng, Deukhyoun Heo, and Haluk Beyenal. Power management system for a 2.5w remote sensor powered by a sediment microbial fuel cell. *Journal of Power Sources*, 196(3):1171 – 1177, 2011.

[16] A. Meehan, H. Gao, and Z. Lewandowski. Energy harvesting with microbial fuel cell and power management system. *IEEE Transactions on Power Electronics*, 26(1):176–181, Jan 2011.

[17] S. Carreon-Bautista, C. Erbay, A. Han, and E. Sanchez-Sinencio. An inductorless dc-dc converter for an energy aware power management unit aimed at microbial fuel cell arrays. *IEEE Journal of Emerging and Selected Topics in Power Electronics*, 3(4):1109–1121, Dec 2015.

[18] I. Lee, G. Kim, S. Bang, A. Wolfe, R. Bell, S. Jeong, Y. Kim, J. Kagan, M. Arias-Thode, B. Chadwick, D. Sylvester, D. Blaauw, and Y. Lee. System-on-mud: Ultra-low power oceanic sensing platform powered by small-scale benthic microbial fuel cells. *IEEE Transactions on Circuits and Systems I: Regular Papers*, 62(4):1126–1135, April 2015.

[19] J. Heidemann, Wei Ye, J. Wills, A. Syed, and Yuan Li. Research challenges and applications for underwater sensor networking. In *IEEE Wireless Communications and Networking Conference, 2006. WCNC 2006.*, volume 1, pages 228–235, April 2006.

[20] J. G. Proakis, E. M. Sozer, J. A. Rice, and M. Stojanovic. Shallow water acoustic networks. *IEEE Communications Magazine*, 39(11):114–119, Nov 2001.

[21] M. C. Potter. Electrical effects accompanying the decomposition of organic compounds. *Proceedings of the Royal Society of London B: Biological Sciences*, 84(571):260–276, 1911.

[22] B. Cohen. The bacterial culture as an electrical half-cell. *J. Bacteriol.*, 21(1):18–19, 1931.

[23] M. G. DelDuca, J. M. Friscoe, and R. W. Zurilla. Developments in industrial microbiology. *American Institute of Biological Sciences*, 1963.

[24] S Suzuki, I Karube, T Matsunaga, S Kuriyama, N Suzuki, T Shirogami, and T Takamura. Biochemical energy conversion using immobilized whole cells of clostridium butyricum. *Biochimie*, 62(5-6):353358, 1980.

[25] Bruce Logan. *Microbial Fuel Cells*. John Wiley & Sons, Inc.

[26] N. Degrenne, F. Buret, F. Morel, S. E. Adami, D. Labrousse, B. Allard, and A. Zaoui. Self-starting dc:dc boost converter for low-power and low-voltage microbial electric generators. In *2011 IEEE Energy Conversion Congress and Exposition*, pages 889–896, Sept 2011.

[27] Bruce E. Logan, Bert Hamelers, Ren Rozendal, Uwe Schrder, Jrg Keller, Stefano Freguia, Peter Aelterman, Willy Verstraete, and Korneel Rabaey. Microbial fuel cells: methodology and technology. *Environmental Science & Technology*, 40(17):5181–5192, 2006.

[28] Conrad Donovan, Alim Dewan, Deukhyoun Heo, and Haluk Beyenal. Batteryless, wireless sensor powered by a sediment microbial fuel cell. *Environmental Science & Technology*, 42(22):8591–8596, 2008.

[29] T Chailloux, A Capitaine, B Erable, and Gaël Pillonnet. Autonomous Sensor Node Powered by CM-Scale Benthic Microbial Fuel Cell and Low-Cost and Off-the-Shelf Components. *Energy Harvesting and Systems*, May 2016.

[30] Fan Yang, Daxing Zhang, Tsutomu Shimotori, Kuang-Ching Wang, and Yong Huang. Study of transformer-based power management system and its performance optimization for microbial fuel cells. *Journal of Power Sources*, 205:86 – 92, 2012.

[31] Daxing Zhang, Fan Yang, Tsutomu Shimotori, Kuang-Ching Wang, and Yong Huang. Performance evaluation of power management systems in microbial fuel cell-based energy harvesting applications for driving small electronic devices. *Journal of Power Sources*, 217:65 – 71, 2012.

[32] Ridvan Umaz. Design of the power management system for marine sediment microbial fuel cell. Master's thesis, University of Connecticut, 7 2013.

[33] Jae-Do Park and Zhiyong Ren. High efficiency energy harvesting from microbial fuel cells using a synchronous boost converter. *Journal of Power Sources*, 208:322 – 327, 2012.

[34] Peter K. Wu, Justin C. Biffinger, Lisa A. Fitzgerald, and Bradley R. Ringeisen. A low power dc/dc booster circuit designed for microbial fuel cells. *Process Biochemistry*, 47(11):1620 – 1626, 2012.

[35] F. Khaled, O. Ondel, and B. Allard. Optimal energy harvesting from serially connected microbial fuel cells. *IEEE Transactions on Industrial Electronics*, 62(6):3508–3515, June 2015.

[36] Ridvan Umaz and Lei Wang. An energy combiner design for multiple microbial energy harvesting sources. In *Proceedings of the on Great Lakes Symposium on VLSI*, pages 443–446, May 2017.

[37] Ridvan Umaz and Lei Wang. An integrated power converter design for low-voltage microbial energy harvesting. In *2017 15th IEEE International New Circuits and Systems Conference (NEWCAS)*, 2017.

[38] I. Doms, P. Merken, C. Van Hoof, and R. P. Mertens. Capacitive power management circuit for micropower thermoelectric generators with a 1.4μ a controller. *IEEE Journal of Solid-State Circuits*, 44(10):2824–2833, Oct 2009.

[39] Y. C. Shih and B. P. Otis. An inductorless dc-dc converter for energy harvesting with a 1.2- μw bandgap-referenced output controller. *IEEE Transactions on Circuits and Systems II: Express Briefs*, 58(12):832–836, Dec 2011.

[40] F. Qian, R. Umaz, Y. Gong, and L. Wang. Design of a shared-stage charge pump circuit for multi-anode microbial fuel cells. In *2016 IEEE International Symposium on Circuits and Systems (ISCAS)*, pages 213–216, May 2016.

[41] Jingjing Che, Chun Zhang, Zhongqi Liu, Ziqiang Wang, and Zhihua Wang. Ultra-low-voltage low-power charge pump for solar energy harvesting systems. In *2009 International Conference on Communications, Circuits and Systems*, pages 674–677, July 2009.

[42] J. F. Dickson. On-chip high-voltage generation in mnos integrated circuits using an improved voltage multiplier technique. *IEEE Journal of Solid-State Circuits*, 11(3):374–378, Jun 1976.

[43] H. Shao, C. Y. Tsui, and W. H. Ki. The design of a micro power management system for applications using photovoltaic cells with the maximum output power control. *IEEE Transactions on Very Large Scale Integration (VLSI) Systems*, 17(8):1138–1142, Aug 2009.

[44] C. Lu, S. P. Park, V. Raghunathan, and K. Roy. Low-overhead maximum power point tracking for micro-scale solar energy harvesting systems. In *2012 25th International Conference on VLSI Design*, pages 215–220, Jan 2012.

[45] P. H. Chen, K. Ishida, Xin Zhang, Y. Okuma, Y. Ryu, M. Takamiya, and T. Sakurai. A 120-mv input, fully integrated dual-mode charge pump in 65-nm cmos for thermoelectric energy harvester. In *17th Asia and South Pacific Design Automation Conference*, pages 469–470, Jan 2012.

[46] J. Kim, P. K. T. Mok, and C. Kim. A 0.15 v input energy harvesting charge pump with dynamic body biasing and adaptive dead-time for efficiency improvement. *IEEE Journal of Solid-State Circuits*, 50(2):414–425, Feb 2015.

[47] T. Tanzawa and T. Tanaka. A dynamic analysis of the dickson charge pump circuit. *IEEE Journal of Solid-State Circuits*, 32(8):1231–1240, Aug 1997.

[48] G. Palumbo, D. Pappalardo, and M. Gaibotti. Charge-pump circuits: power-consumption optimization. *IEEE Transactions on Circuits and Systems I: Fundamental Theory and Applications*, 49(11):1535–1542, Nov 2002.

[49] Timothy Ewing, Phuc Thi Ha, Jerome T. Babauta, Nghia Trong Tang, Deukhyoun Heo, and Haluk Beyenal. Scale-up of sediment microbial fuel cells. *Journal of Power Sources*, 272:311–319, 2014.

[50] Firas Khaled, Olivier Ondel, and Bruno Allard. Microbial fuel cells as power supply of a low-power temperature sensor. *Journal of Power Sources*, 306:354 – 360, 2016.

[51] M. Patoka. Fundamentals of power system oring. *Power Management Design Lines EE Times*, March 2007.

[52] C. Vankecke, L. Assoure, A. Wang, P. Durand-Estbe, F. Caignet, J. M. Dilhac, and M. Bafleur. Multisource and battery-free energy harvesting architecture for aeronautics applications. *IEEE Transactions on Power Electronics*, 30(6):3215–3227, June 2015.

[53] D. Carli, D. Brunelli, L. Benini, and M. Ruggeri. An effective multi-source energy harvester for low power applications. In *2011 Design, Automation Test in Europe*, pages 1–6, March 2011.

[54] Y. K. Tan and S. K. Panda. Energy harvesting from hybrid indoor ambient light and thermal energy sources for enhanced performance of wireless sensor nodes. *IEEE Transactions on Industrial Electronics*, 58(9):4424–4435, Sept 2011.

[55] J. Colomer-Farrarons, P. Miribel-Catala, A. Saiz-Vela, and J. Samitier. A multiharvested self-powered system in a low-voltage low-power technology. *IEEE Transactions on Industrial Electronics*, 58(9):4250–4263, Sept 2011.

[56] S. Bandyopadhyay and A. P. Chandrakasan. Platform architecture for solar, thermal, and vibration energy combining with mppt and single inductor. *IEEE Journal of Solid-State Circuits*, 47(9):2199–2215, Sept 2012.

[57] C. Shi, B. Miller, K. Mayaram, and T. Fiez. A multiple-input boost converter for low-power energy harvesting. *IEEE Transactions on Circuits and Systems II: Express Briefs*, 58(12):827–831, Dec 2011.

[58] T. Kang, S. Kim, C. Hyoung, S. Kang, and K. Park. An energy combiner for a multi-input energy-harvesting system. *IEEE Transactions on Circuits and Systems II: Express Briefs*, 62(9):911–915, Sept 2015.

[59] A. Romani, M. Filippi, and M. Tartagni. Micropower design of a fully autonomous energy harvesting circuit for arrays of piezoelectric transducers. *IEEE Transactions on Power Electronics*, 29(2):729–739, Feb 2014.

[60] M. Dini, A. Romani, M. Filippi, V. Bottarel, G. Ricotti, and M. Tartagni. A nanocurrent power management ic for multiple heterogeneous energy harvesting sources. *IEEE Transactions on Power Electronics*, 30(10):5665–5680, Oct 2015.

[61] G. Yu, K. W. R. Chew, Z. C. Sun, H. Tang, and L. Siek. A 400 nw single-inductor dual-input-tri-output dc-dc buck-boost converter with maximum power point tracking for indoor photovoltaic energy harvesting. *IEEE Journal of Solid-State Circuits*, 50(11):2758–2772, Nov 2015.

[62] Y. S. Yuk, S. Jung, H. D. Gwon, S. Choi, S. D. Sung, T. H. Kong, S. W. Hong, J. H. Choi, M. Y. Jeong, J. P. Im, S. T. Ryu, and G. H. Cho. 23.5 an energy pile-up resonance circuit extracting maximum 422% energy from piezoelectric material in a dual-source energy-harvesting interface. In *2014 IEEE International Solid-State Circuits Conference Digest of Technical Papers (ISSCC)*, pages 402–403, Feb 2014.

[63] H. Lhermet, C. Condemine, M. Plissonnier, R. Salot, P. Audebert, and M. Rosset. Efficient power management circuit: From thermal energy harvesting to above-ic microbattery energy storage. *IEEE Journal of Solid-State Circuits*, 43(1):246–255, Jan 2008.

[64] N. Tang, W. Hong, T. Ewing, H. Beyenal, J. H. Kim, and D. Heo. A self-sustainable power management system for reliable power scaling up of sediment microbial fuel cells. *IEEE Transactions on Power Electronics*, 30(9):4626–4632, Sept 2015.

[65] Seiko Instruments Inc. *Ultra low voltage operation charge pump IC for step UP DC-DC converter startup.* S882Z Datasheet, 2010.

[66] Korneel Rabaey and Willy Verstraete. Microbial fuel cells: novel biotechnology for energy generation. *Trends in Biotechnology*, 23(6):291 – 298, 2005.

[67] Farzaneh Rezaei, Tom L. Richard, Rachel A. Brennan, and Bruce E. Logan. Substrate-enhanced microbial fuel cells for improved remote power generation from sediment-based systems. *Environmental Science & Technology*, 41(11):4053–4058, 2007.

[68] STMicroelectronics. *Synchronous rectifier step up converter.* L6920DB Datasheet, Oct., 2006.

[69] Po-Hung Chen, K. Ishida, Xin Zhang, Y. Okuma, Y. Ryu, M. Takamiya, and T. Sakurai. 0.18-v input charge pump with forward body biasing in startup circuit using 65nm cmos. In *IEEE Custom Integrated Circuits Conference 2010*, pages 1–4, Sept 2010.

[70] K. Kadirvel, Y. Ramadass, U. Lyles, J. Carpenter, V. Ivanov, V. McNeil, A. Chandrakasan, and B. Lum-Shue-Chan. A 330na energy-harvesting charger with battery management for solar and thermoelectric energy harvesting. In *2012 IEEE International Solid-State Circuits Conference*, pages 106–108, Feb 2012.

[71] P. S. Weng, H. Y. Tang, P. C. Ku, and L. H. Lu. 50 mv-input batteryless boost converter for thermal energy harvesting. *IEEE Journal of Solid-State Circuits*, 48(4):1031–1041, April 2013.

[72] J. M. Damaschke. Design of a low-input-voltage converter for thermoelectric generator. *IEEE Transactions on Industry Applications*, 33(5):1203–1207, Sep 1997.

[73] E. J. Carlson, K. Strunz, and B. P. Otis. A 20 mv input boost converter with efficient digital control for thermoelectric energy harvesting. *IEEE Journal of Solid-State Circuits*, 45(4):741–750, April 2010.

[74] G. De Vita and G. Iannaccone. A sub-1-v, 10 ppm/ ^{circ}c, nanopower voltage reference generator. *IEEE Journal of Solid-State Circuits*, 42(7):1536–1542, July 2007.

[75] S. Carreon-Bautista, C. Erbay, A. Han, and E. Snchez-Sinencio. Power management system with integrated maximum power extraction algorithm for microbial fuel cells. *IEEE Transactions on Energy Conversion*, 30(1):262–272, March 2015.